Phase and Morphological Control of Copper(I) Chalcogenide Nanocrystals

By

Evan Hojer Robinson

Dissertation
Submitted to the Faculty of the
Graduate School of Vanderbilt University
in partial fulfillment of the requirements
for the degree of

DOCTOR OF PHILOSOPHY
in
Chemistry
May 8, 2020
Nashville, Tennessee

Approved:

Janet. E. Macdonald, Ph.D.
Timothy P. Hanusa, Ph.D.
Sandra J. Rosenthal, Ph.D.
Bridget R. Rogers, Ph.D.

DEDICATION

To my family, thank you all for the support you have given me over the last five years. Ashley, Margot, and mom, you are the most important people in my life and I love you dearly.

To Janet, words cannot describe how appreciative I am for all you have done for me. I cannot tell you how many times I left your office thinking, "that's why Janet is the boss, and I am the grasshopper." The lab is founded on all of your hard work and your vision. I hope your horizons continue to expand over the years and I look forward to following the lab's work. Mike, thank you for paving the way for my first project and teaching me the fundamentals of nanocrystal synthesis through email and text message. Your wizard-like psychic vibrations still reverberate through the halls of the chemistry department. Andrew, you were always there with thoughtful (and much appreciated) advice, I'm happy you found a job at Lander and hope the work is fulfilling. Thanks for inviting Ashley and me over for D&D. Emil, you are a natural leader, and your presence in the lab lifted everyone's spirits. Your attitude, knowledge of chemistry, and vision for both short- and long-term goals were indispensable during my time in the Macdonald lab. I feel confident that you can run a research group. I wish you all the best going forward. Jordan, if you look up cool in the dictionary, I know you'll see your photo there. You have impressed me both as a chemist and of course as an artist. The future is very bright for you and I look forward to seeing where your career takes you. Shane, you proved that being a parent in graduate school and maintaining your sanity was possible, so I felt a lot more confident when Ashley

and I had Margot. Elijah is lucky to have such a great dad. Alice, you set the high-water mark for the group and gave us all something to shoot for (?) or simply raise our beers at. Your knowledge and competence are matched only by your high trajectory. Steph, I'm very happy you found a position that fits what you want to do professionally. Science outreach seems tailored to you, and I wish you the best with your interdisciplinary doctorate and PhutureDoctors. Thanks for listening to me complain about life so much. Summer, thank you for helping me get squared away when I first joined the lab, your easygoing attitude was reassuring when I was jumping into the mysterious world of graduate research. I'm glad your job has turned into a rewarding experience. Suresh, thank you for all of the advice, and congratulations on starting such a wonderful family. I'm happy for you. Chris, Maddy and Nathan, the third-year tri-force. The Macdonald lab is lucky to have you guys, I feel like you will quickly surpass what I have accomplished. Chris, thank you for taking over the XRD, keep your eye out for RS1, RS2, the chiller, the instrument and the software. Any issues you have with those can be resolved with a voodoo ritual, be sure to use plenty of cheetah blood. Nathan, [insert witticism about Purdue/IRS/90s alternative], am I right? Maddy, you have the skills and perseverance to accomplish anything since you steered the Co project back on course. I hope that project will be/has been fruitful. Lexie, welcome to the group! Nikki and Paul, you guys were lightyears beyond what I was capable of in undergrad, I was very impressed with your knowledge of chemistry and how you guys conducted yourselves. I hope your continued academic pursuits lead to fulfilling careers.

May your base baths be the good kind of silent…

ACKNOWLEDGEMENTS

This work was supported financially by the Vanderbilt University Department of Chemistry. I gratefully acknowledge the funding of the work presented herein through National Science Foundation (NSF) CAREER Award Sus-ChEM-1253105, NSF EPS-1004083, NSF CHE-1905265 and the Vanderbilt Institute of Nanoscale Science and Engineering (VINSE). I would like to thank and acknowledge support from the Mitchum E. Warren Fellowship.

I would like to thank the following people for their help over the last five and a half years. My committee: Professors Janet Macdonald, Sandra Rosenthal, Timothy Hanusa and Bridget Rogers for the spirited discussions and advice. Prof. Bridget Rogers for help with XPS data acquisition and interpretation. Emil and Andrew for bringing me onto the $Cu_{2-x}Se$ project. I'm very grateful to you guys. Prof. Ahmed Nuriye for graciously providing the ditelluride precursor. James R. McBride for being a huge resource on the TEM and all things related to nanocrystal chemistry. Prof. Nathan Schley for help with single-crystal diffractometry and the processing of data. Anthony Hmelo and Dmitry Koktysh for help with instrument training. Ross Koby and Jordan Rhodes for help with DFT calculations. Chris Sharp for help with the XRD. The Cliffel lab members for help with electrochemistry, namely Margaret Calhoun and Aaron Daniel. I would like to thank Prof. Sandra Rosenthal and the members of the Rosenthal lab for help in a countless number of instances. Huge thanks to Ian Tomlinson, Talitha VanWie, Louie Thal, Danielle Bailey, Kemar Reid, Nathaniel Freymeyer, Oleg Kovtun, Sophie Click, Cara Bradsher, Devin

Taylor, Noah Orfield, Toshia Wrenn, Joe Keene and Scott Niezgoda. I and many members of the Macdonald lab owe Keri Tallman a huge debt of thanks for all of the help she has provided us. Thanks for being so patient with my long list of questions over the years.

I would like to thank the Chemistry Department staff and Plant Ops for everything they have done for me, particularly Jackie, Robert and Paulette for all things related to ordering materials, Magda for help with orchestrating the XRD's billing, and Laura Johnson for bringing my family food when my wife was recovering.

The department has been very supportive during my time here, and I'm grateful. Thank you so much.

TABLE OF CONTENTS

Page

LIST OF TABLES

Table Page

LIST OF FIGURES

Figure Page

Chapter 1

INTRODUCTION

1.1 Balancing the Progress of Civilization and Caring for the Planet

Mankind's quest to create a larger and more complex civilization has taken a toll on the planet, changing the composition of air above and the water and soil below. Electricity generation, transportation and industrial production have placed a massive burden on the earth's resources to meet the needs of an ever-growing population. Additionally, the planet's natural means of regulating the amount of carbon dioxide in the atmosphere (plants) has been shown to become less effective upon drastic increases in CO_2 concentration.[1] The U.S. Government's Energy Information Administration (EIA) estimates that the country will continue to rely upon natural gas, oil and coal as the primary sources of energy to 2050, with renewables estimated to surpass coal in the late 2040s (Figure 1.1).[2] If greener means of energy production are not embraced on larger scales,

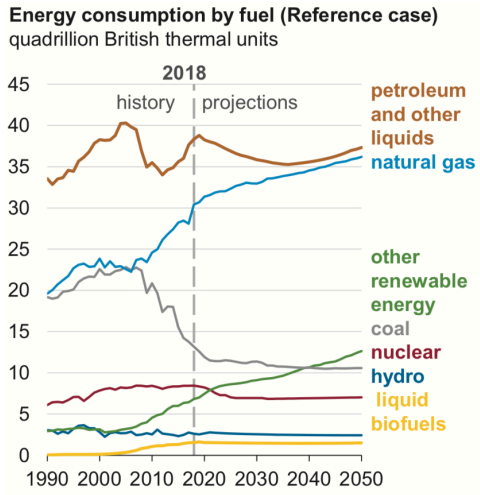

Figure 1.1. The U.S. EIA energy outlook to 2050, highlighting projected consumption of fossil fuels. Source: U.S. Energy Information Administration (Jan. 2019).

combustion of liquid hydrocarbon fuels, natural gas, and coal will continue to increase the amount of carbon in the atmosphere for the foreseeable future.

The associated rise in global temperature (and its disastrous effects) due to the generation of greenhouse gases is a primary concern when debating the continued use of fossil fuels. An alarming report by the U.N.'s Intergovernmental Panel on Climate Change (IPCC) in October of 2018 laid out a warning regarding mankind's effect on global temperature increases since the Industrial Revolution.[3] The panel concluded that the earth is on track for a 1.5 ˚C rise over "pre-industrial" temperatures, and if no action is taken the global temperature could rise by as much as 2.0 ˚C. The effects would include "severe and widespread impacts" to marine life, the arctic, and coastlines. The IPCC warns that for the global temperature to not exceed a 1.5 ˚C increase, carbon dioxide emission must be cut 45% by 2030.

With this in mind, there exist emergent technologies that may mitigate man's negative effects on the environment. Green energy production, which includes solar, wind and hydrothermal energy capture (among others), is the promising alternative to fossil fuel combustion, and will be at the fore in the fight to reverse climate change.[4] Currently, solar and wind electricity production are among the least expensive alternatives to fossil fuels.[5] Solar cell arrays have the advantages of no (or few) moving parts, being practical in urban environments, and making use of the sun's abundant energy. In addition, small-scale processing is also possible with newer-generation solar cell components, like semiconductor nanocrystals (or crystals composed of semiconductor materials with dimensions on the nanometer scale). Research groups have driven nanocrystal-based solar cell efficiencies from 3% in 2010[6] to efficiencies in the mid-teens,[7,8] with the current record

[Spring 2019] standing at 16.6% (Lianzhou Wang, University of Queensland). Utilizing components like semiconductor nanocrystals bypasses the industrial infrastructure needed to produce traditional silicon-based solar cells[9] (Figure 1.2) and wind turbines, and will make applications viable in developing communities.

Figure 1.2. (left) A commercial boule growing system from PVATePla (right, image used with permission) a boule of Si to be cut into wafers (from waferpro.com, image used with permission).

In addition to solar cells, semiconductor nanocrystals have been used in other energy-related applications like photocatalytic water splitting and as light emitters.[10] The hydrogen fuel cell could be another potential route to breaking free of fossil fuel dependency if hydrogen production can be achieved without steam reformation or electrolysis that uses fossil-fuel-produced electricity. Steps have been taken towards photocatalytic production of hydrogen from water,[11,12] but issues like material stability will need to be overcome.

The need for new technologies and improvements upon existing green energy alternatives is driving researchers to harness control of materials at the nanoscale. If control of nanomaterials can match the imagination of scientists and the increasing need for new

energy sources, mankind may be able to reverse the rising tide of manmade climate change through advances in fuel and electricity production.

1.2 Introduction to Nanocrystal Chemistry

Nanocrystals (NCs) are particles of crystalline material in which one dimension is at or below around 100 nanometers.[13] NCs fall under the umbrella term "nanoparticles" which additionally includes amorphous phase[14] and polymer-based particles.[15] An interesting early example of mankind's (likely accidental) use of NCs is the Lycurgus Cup, an ancient Roman chalice composed of pea-colored cut glass (in ambient light) which appears bright translucent red when light is transmitted through the vessel. Modern electron microscopic analysis of the cup revealed that 50-100 nm Ag/Au alloyed NCs were responsible for the "dichroic" coloration.[16] We now know that the interesting properties of the Lycurgus Cup are due to the metal nanocrystals' localized surface plasmon resonance (LSPR),[17] or a phenomenon in which light is scattered due to the oscillatory resonance of the NC's conduction electrons.[18] More recently, the seminal studies of colloidal nanoparticle science began with work by Michael Faraday in the 1850s.[19] Faraday's prescient observations included the correlation between particle size and the system's color. The modern understanding of these dynamic size-dependent properties began with Brus's proposal of the quantum confinement effect. While at Bell Laboratories, Brus's work formed the foundational understanding of what would become known as quantum dots (QDs). QDs are a special type of fluorescent nanocrystals in which unique properties are seen due to confinement of generated excitons (electron/hole pairs) to domains smaller than the material's exciton Bohr radius.[20,21]

The versatility of the colloidal nanocrystal has made it the focus of a great deal of fundamental and applied research. What follows is an introductory discussion on nanocrystal synthesis, properties and characterization techniques.

1.2.1 Introduction to Nanocrystal Synthesis and Brief Historical Context

A broad range of crystalline metal and semiconductor materials are used in NC chemistry, and tailoring NC systems for end-of-line applications results in a multitude of crystal phases, morphologies, and unique surface chemistries. In this section, the fundamental concepts underlying nanocrystal synthesis will be introduced, including nucleation theory and crystal growth. Additional background on the development of modern solvothermal nanocrystal synthesis will be discussed, highlighting the early synthetic work in the field.

Nucleation theory is the study of colloid formation from concentrated precursor solutions and the thermodynamic balancing act between the formation of solids and their surfaces. The Gibbs crystal free energy equation (eq. 1) models the disparity between the thermodynamically favorable bulk free energy of the nanocrystal and the unfavorable surface free energy.

$$\Delta G = \frac{4}{3}\pi r^3 \Delta G_v + 4\pi r^2 \gamma \quad (1)$$

As depicted in Figure 1.3, the surface energy term $4\pi r^2\gamma$, where γ is the surface energy of a particle with radius r, is always positive. Thus, NC systems with more surface area, i.e. many small NCs, are less thermodynamically favorable than a single large crystal in which the $\frac{4}{3}\pi r^3\Delta G_v$ term dominates.[22] ΔG_v is the free energy of the crystal, or the energy

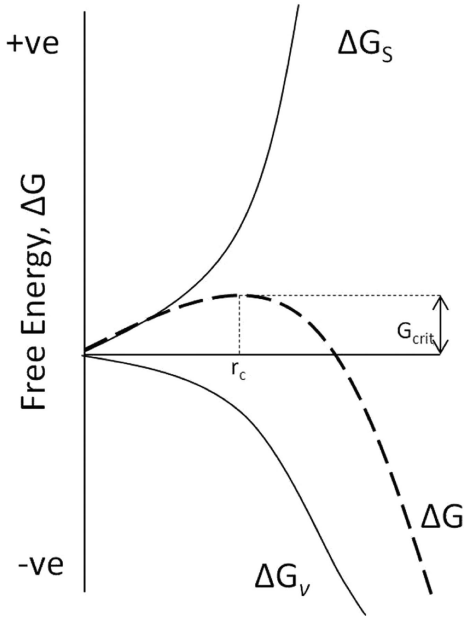

Figure 1.3. Plot of free energy (ΔG) v. particle radius (r). Reprinted with permission from Thanh, N. T. K., et al. *Chem. Rev.* **2014**, *114* (15), 7610. Copyright 2014 American Chemical Society.

difference between a monomer unit (of the crystalline material) in a crystal or in solution.[23] Thus, in a synthesis environment, nanocrystal systems tend to lessen the thermodynamic impact of the higher energy surfaces by growing larger at the expense of smaller particles, in a phenomenon known as Ostwald ripening.[24] In Figure 1.3, an important size is noted (r_c) which must be met for a nanocrystal to achieve permanence, otherwise it will dissolve. This critical radius is the point at which the stability offered by the nascent crystal begins to counteract the energy required for the sub-r_c higher-surface-area nanocrystals. Particles that meet this radial requirement can now grow larger.[23] Above the critical radius, the NC growth rate is initially high, but begins to taper off at larger and larger NC radii, leading to

a "focusing" of the size distribution. This idea was proposed by Sugimoto[25] and later proven experimentally by Peng, et al.[26]

Victor LaMer's works on nucleation dating to the mid-20th century laid the groundwork for our modern understanding of nanocrystal synthesis. LaMer observed that a sulfur-producing reaction would nucleate when the precursor reached a certain concentration (region II in Figure 1.4), and following this "outburst of nuclei," monomers would continue to coalesce on the particle surfaces resulting in growth.[27,28] This coalescence of monomers on the nanocrystal surface is favored in larger particles that exceed the critical radius mentioned above.

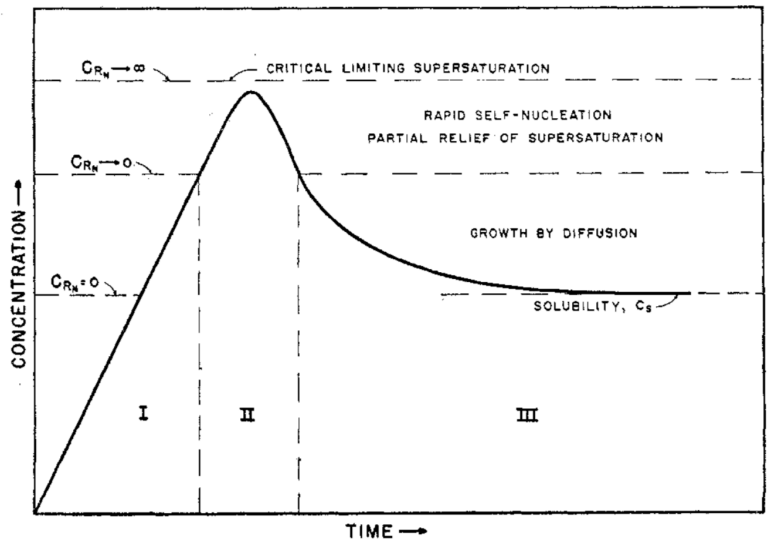

Figure 1.4. LaMer's plot of burst nucleation. Region I, monomer formation reaches a critically high concentration. Region II, nucleation of material occurs which lowers monomer concentration, nucleation immediately ceases. A single, brief nucleation event is ideal when forming monodisperse NCs. Region III, the monomer concentration is no longer high enough for homogenous nucleation, so monomers coalesce on the particle surface, resulting in NC growth. Reprinted with permission from La Mer, V. K. *Ind. Eng. Chem.* **1952**, *44* (6), 1270. Copyright 1952 American Chemical Society.

In a typical solvothermal nanocrystal synthesis, one needs a solvent that can withstand elevated temperatures, a ligand species that will coordinate to and stabilize the surface of the nanocrystal, and the precursors for the semiconductor (or metal) nanocrystalline material.[29] Solvothermal nanocrystal syntheses occur in organic solvents as opposed to hydrothermal syntheses that occur in water,[30] therefore ligands (and coordinating solvents) typically have a polar headgroup to attach to the NC surface sites and a hydrocarbon chain to keep the nanocrystals colloidally suspended. Examples of molecules commonly found in nanocrystal syntheses can be seen in Figure 1.5.

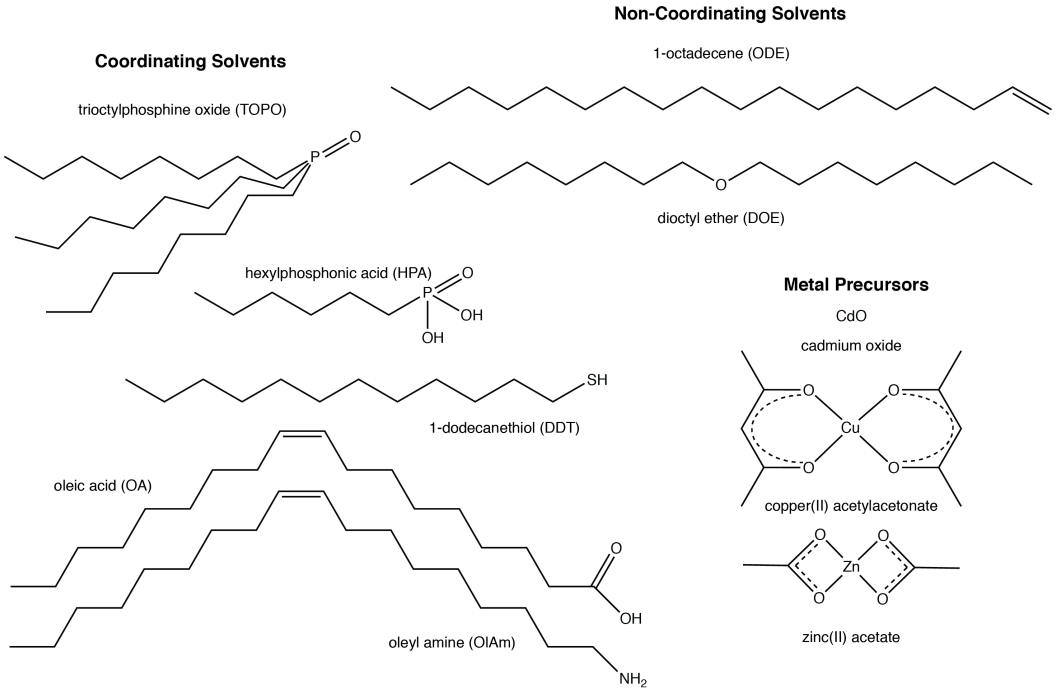

Figure 1.5. Common components of solvothermal nanocrystal syntheses, including coordinating solvents (ligands), non-coordinating solvents, and metal precursors.

The early 1980s saw the genesis of the modern era of purposeful nanocrystal synthesis. Early syntheses involved creating sols of semiconductor materials such as TiO_2[31–33] and CdS[33–36] and ZnS[37] in aqueous media. These systems were susceptible to aggregation and ripening, and Brus wrote contemporaneously that characterization was

carried out in the reaction media to avoid these deleterious issues.[38] The Henglein (Germany) and Brus (Bell Labs) groups controlled nanocrystal solubility—and therefore Ostwald ripening—by performing syntheses in organic solvents like 2-propanol[39] and acetonitrile,[40] respectively, resulting in particle sizes smaller than those possible in aqueous media where NC dissolution would occur. Henglein's group also explored the use of a complexing species, hexametaphosphate, which stabilized small CdS NCs in water by reducing the material's solubility, and allowed for re-dispersion of dry CdS NC powders.[39] The implications of this NC surface chemistry manipulation were vast, as the concept would become an essential part of many areas of investigation, including morphology and phase control.

Nanocrystal syntheses based on surfactants and microemulsions remained a popular option into the late 1980s,[41] then chemists at Bell Labs synthesized single-source molecular precursors from Me_2Cd and a selenol[42] or bis(trimethylsilyl)selenium,[43] which could be heated to 400 ˚C resulting in CdSe NCs. Several months later, Moungi Bawendi (also at Bell Labs) published a synthetic method that converted zinc blende (ZB) CdSe[44] to the wurtzite (WZ) crystal structure through annealing (at ~220 ˚C) in tributylphosphine and tributylphosphine oxide coordinating solvents,[45] highlighting the importance of stabilizing coordinating solvents and an early example of NC phase control.

Christopher Murray's 1993 publication (in Bawendi's group at MIT) on cadmium chalcogenide nanocrystal synthesis was a seminal work that aimed to ensure LaMer's burst nucleation event would take place in a controlled manner by injecting precursors into a hot reaction environment.[46] Subsequent evaluations of this work have marked this publication as the genesis of the "hot-injection" technique,[29] and have acknowledged the procedure's

results as highly uniform[47] and the advantageous scalability of the synthetic process.[48] The "hot-injection" technique is still commonly used in the synthesis of group II-VI semiconductors, though dimethyl cadmium has been replaced with a less-dangerous precursors like cadmium oleate (from CdO reacted in oleic acid, see Xiaogang Peng).[49]

Another common nanocrystal synthesis procedure is known as the "heat-up" method.[50] This involves mixing NC precursors at low temperature and then heating the system. The nucleation event is caused by the controlled thermal decomposition of the precursors, or complexes that form during the ramp up to reaction temperature.[51,52] This type of NC synthesis will be primarily discussed in this thesis as it relates to the formation of Cu_2S, $Cu_{2-x}Se$ and $Cu_{2-x}Te$ nanocrystals.

In a procedure representative of the heat-up method, stoichiometric chalcocite Cu_2S nanocrystals can be synthesized with a copper precursor such as copper(II) acetylacetonate and the solvent 1-dodecanethiol (DDT). The earliest precedent of using DDT with a copper precursor in a heat-up synthesis appears to be a 2004 publication by Kuzuya, et al.[53] and variations on the general procedure have been used in many other texts in the years since.[54,55] In the Cu_2S synthesis described above, the thiol is serving three distinct purposes as the solvent, the sulfur source, and the NC ligand. This synthesis is foundational in much of the work performed by the laboratory of Janet Macdonald, and this is due to the special nanocrystal surface chemistry that this type of synthesis produces (vide infra).

1.2.2 Nanocrystal Properties and Characterization

It has been noted that using a primary thiol in NC synthesis results in NCs that are resistant to ligand exchange,[56] and this rugged ligand attachment lends itself well to high

temperature applications. While in Uri Banin's lab, Macdonald, et al. published a paper in which these aforementioned Cu_2S nanocrystals served as a template for the growth of a ruthenium deposition along the high-energy edge sites between facets.[57] As seen in Fig. 1.6, the resulting cages are only possible due to the special surface chemistry of the thiols on the Cu_2S NCs that block the facets from Ru deposition even at the high temperature of 210 ˚C. At Vanderbilt University, Turo and Macdonald were able to show that these

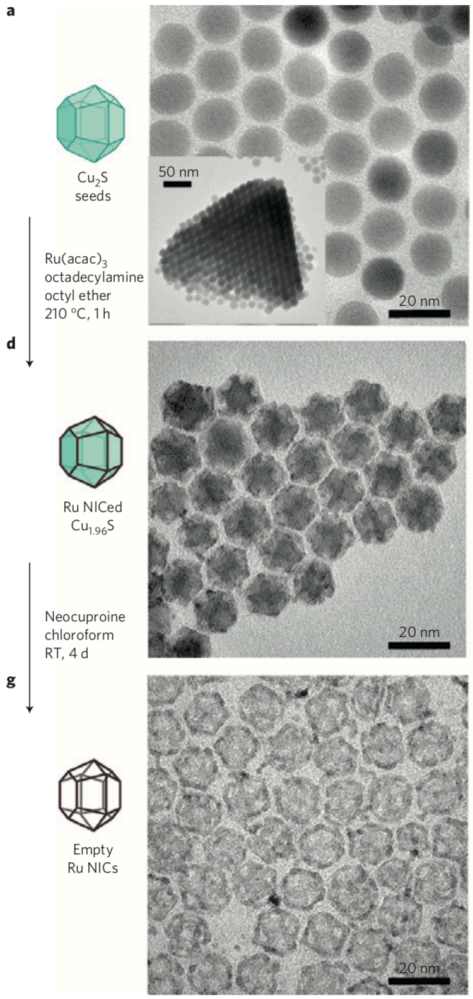

Figure 1.6. Cu_2S nanocrystals are synthesized, and Ru is deposited via Ru(III) reduction with oleylamine. This results in a Ru(0) cage that can be isolated through dissolution of the semiconductor core with neocuproine. Reprinted with permission from Springer Nature: Nature Materials. Citation: Macdonald, J. E., et al. *Nat. Mater.* **2010**, *9* (10), 810. Copyright 2010.

thiolate ligands occupy high-coordination number sites, i.e. the ligands' sulfur atoms are actually integrated into the nanocrystal lattice itself. Turo called these thiolates "crystal-bound" ligands, distinguishing this ligand binding mode from existing systems.

The covalently attached ligands used commonly in NC syntheses, known as "surface-bound" ligands, will attach to the NC surface in one of several ligand binding modes.[58–60] Shown in Fig. 1.7, L-type ligands, like dodecanethiol, oleylamine (OlAm) or

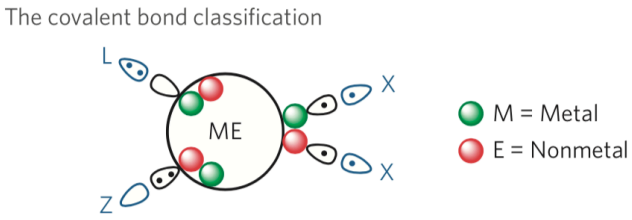

Figure 1.7. L, X and Z-type ligand binding with orbitals and electrons elucidating bond dynamics. Reprinted with permission from Springer Nature: Nature Materials. Citation: De Roo, J. et al. *Nat. Mater.* **2016**, *15* (5), 517. Copyright 2016.

trioctylphosphine oxide (TOPO), donate a pair of electrons to the metallic component of the semiconductor nanocrystals. This is as opposed to X-type ligands, which donate a single electron and are exemplified by dodecanethiolate, oleic acid and phosphonic acids. The Z-type binding mode is a special case in which a metal cation is bound between two X-type ligands, which allow the metal to act as a Lewis acid and accept two electrons from the NC's surface. For example, when a Cd-oleate complex is bound to the surface of a cadmium chalcogenide NC.[61] Turo proposed that X-type alkanethiolate sulfur atoms were integrated into the NC surface (Fig. 1.8) which was evidenced by NMR, TGA-MS and

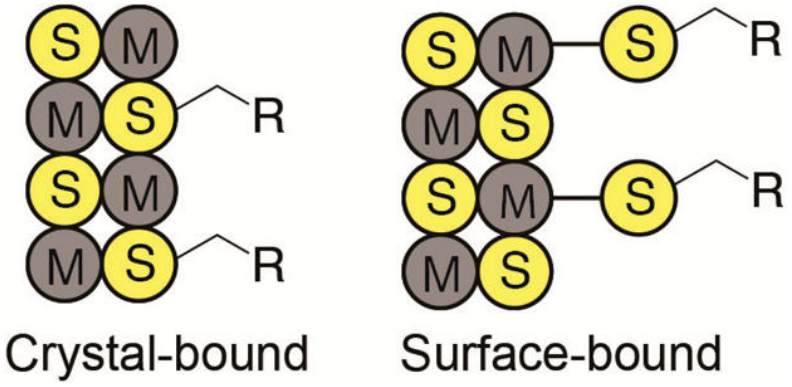

Figure 1.8. Crystal-bound and surface-bound ligands. Reprinted with permission from Turo, M. J., et al. *ACS Nano* **2014**, 8 (10), 10205.Copyright 2014 American Chemical Society.

XPS data.[62] This Cu_2S nanocrystal system with crystal-bound dodecanethiol ligands will be exploited to synthesize nanorods of that material in Chapter 2.

In addition to their surface chemistry, semiconductor nanocrystals (like NCs of Cu_2S) offer researchers fertile ground for investigation in many other areas including their electronic properties. NCs that comprise of semiconductor materials maintain the familiar band structures of their bulk counterparts with a noteworthy difference first proposed by Louis Brus. In addition to early works on nanocrystal synthesis, Brus's discovery of the phenomenon known as quantum confinement is likely his most crucial contribution to the field.[21] Quantum confinement correlates semiconductor bandgap energy to crystallite size (of radius r) through equation 2. A nanocrystal's bandgap (E_{BG}^{*}) is related to the bulk material's bandgap and the additive effect of the exciton pair's particle-in-a-box-like kinetic energy, followed by the deleterious Coulombic attraction between the electron and hole. The final term is based on the polarization of the NC due to the presence of a point charge, though this term can be neglected and the equation will nonetheless afford information on the lowest excitonic state.[63] Quantum confinement effects are seen in nanomaterials when one of the physical dimensions begins to approach the Bohr exciton radius,[64] a spatial distance which is an intrinsic characteristic of a given material. The Bohr

exciton radius is representative of the typical volume that the exciton pair will occupy once generated.[65]

$$E_{BG}^{*} = E_{BG_{bulk}} + \frac{h^2\pi^2}{2r^2}\left[\frac{1}{m_e^* m_0} + \frac{1}{m_h^* m_0}\right] - \frac{1.8e^2}{\varepsilon\varepsilon_0 r} + \frac{e^2}{r}\sum_{n=1}^{\infty}\alpha_n\left[\frac{s}{r}\right]^{2n} \quad (2)$$

Brus's quantum confinement concept can be visualized in depictions like the one in Fig. 1.9. A bulk semiconductor is comprised of a vast quantity of atoms (Si: ~10^{22} atoms/cm^3), and these atoms represent a virtually infinite density of available states in that semiconductor's valence and conduction bands (which are conceptually similar to ground and excited states, respectively). However, in nanoscale crystallites, a finite quantity of atoms is present on the order of hundreds or thousands per NC. By confining the size of these crystals to smaller and smaller volumes, one is effectively removing atoms from the crystal lattice. Therefore, energy states are also removed at smaller NC sizes, ultimately

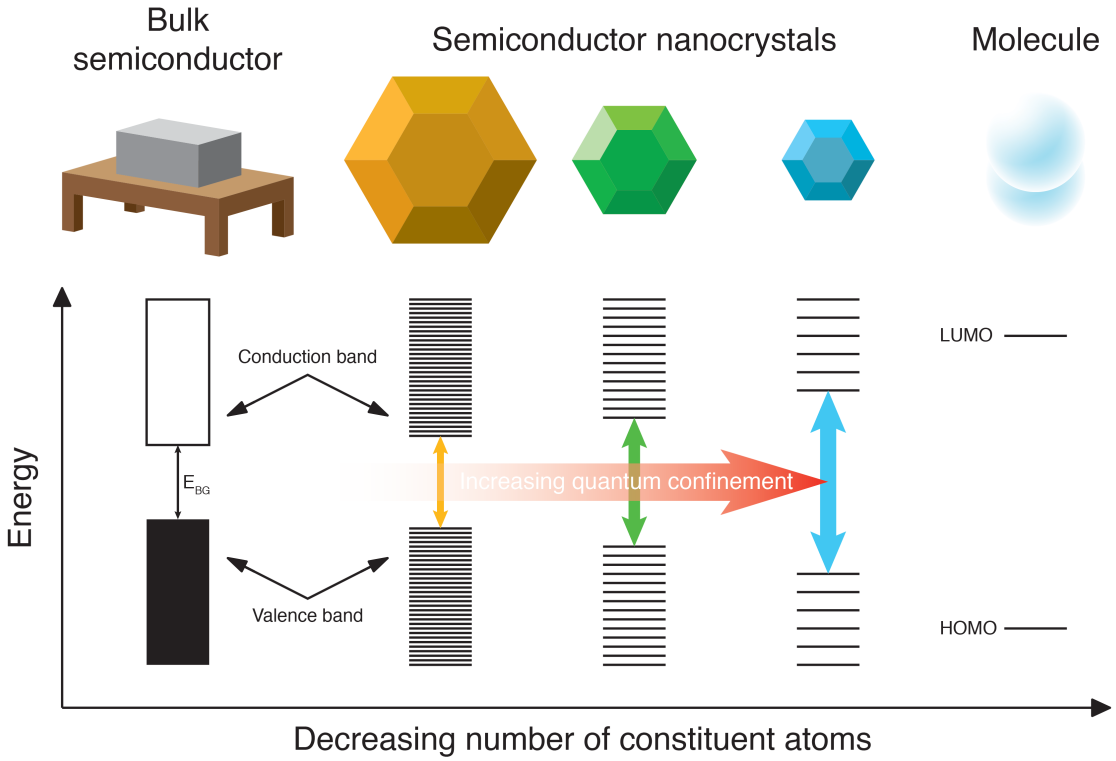

Figure 1.9 Visual representation of semiconductor crystallite size and correlating bandgap widening at the nanoscale.

thinning out the energy bands and widening the bandgap. In the end, smaller nanocrystals fluoresce higher energy blue light in comparison to their larger red-light-fluorescing counterparts. This is explained by Brus's quantum confinement concept.

The unique optical and electronic properties of semiconductor nanocrystals make them ideal for display applications, photovoltaics, photocatalysis and biomedicine.[66] Like their bulk counterparts, semiconductor nanocrystals generate an electron/hole pair when they are supplied with sufficient energy. An electron is excited to the conduction band, leaving a hole in the valence band, where they can move spatially (conduction) or recombine. Exciton recombination releases energy mirroring the nanocrystal's bandgap. Applications scientists and engineers can take advantage of both radiative and non-radiative charge recombination, or they can extract the charge before recombination can take place.

Quantum dots emit light in a narrow wavelength range, and they are used commercially in displays (televisions) and as biomarkers in research applications.[67–69] The ability to track a specific protein in a cell is a powerful investigative technique, and this can be accomplished with monovalent attachment of QDs to proteins or other targets through linker molecules.[70–75] Special microscopes allow researchers to track the movement of these quantum dots in situ, revealing information on the cell environment dynamics. The brightest quantum dots (QDs with the highest quantum yields) are typically shelled with additional layers of material, which form a defect-passivating heterojunction with the fluorescent center nanocrystal.[76–78] One-dimensional nanorods can also be grown around a QD, and these nanorods can absorb photons like an antenna,[79] funneling excitons

into the fluorescent core increasing the quantum yield. This synthetic technique (rod growth) requires control over nanocrystal morphology (vide infra).

Non-radiative charge recombination pathways can be leveraged to produce heat, which can be used to destroy cancer cells photothermally.[80] In addition, semiconductor nanocrystals can be used as components in solar cells and in photocatalytic applications. As mentioned previously, these NCs do not require the technically elaborate production infrastructure that silicon boule crystallization does; semiconductor NCs can be synthesized at the bench-scale and tailored to the specific device application with modifications to material composition and crystallite size.[81] Semiconductor NCs are used as a photon-absorbing layer within quantum dot solar cell (QDSC) devices, and the electron/hole pairs generated therein quickly transfer to their respective energetically favorable charge pathways within the device producing a current.[82]

Photocatalytic applications also take advantage of electron and/or hole generation and use charge carriers to run redox reactions like water splitting.[83] Ever-improving control over nanoscale synthesis has led to heterostructures that direct electron and hole movement within the nanostructures themselves. Selective deposition of catalytic precious metals, like platinum, on the crystallographically anisotropic tips of wurtzite CdS nanorods is a well-known example of a photocatalytic nano-heterostructure.[84] In this system, the electron is funneled into the Pt tip due to the heterostructure's band alignment, while the hole is trapped in a CdSe core embedded within the CdS nanorod. This spatial (and energetic) separation of charge prevents recombination and allows the electron to be used in the production of hydrogen gas, a valuable commodity in the emerging energy economy.

1.2.3 Morphology and Phase Control

The ability to dictate the phase and morphology of nanomaterials is an essential skill for the materials chemist. Many advantageous material properties are unlocked when a certain nanocrystal morphology or phase is obtained. For example, plasmonic nanocrystals can exhibit additional resonances caused by shape-dependent modes,[17,85] and phase-dependent NC optical properties are also exploitable.[86] As discussed below, controlling morphology is itself largely dependent upon control of phase.

It is known that nanomaterials comprise crystal structures and facets that mirror those of their bulk counterparts.[87] That is, crystal structures that were historically characterized by geologists and mineralogists on the macroscopic scale[88,89] are relevant to the modern nanomaterials chemist. In a simple example, PbSe nanocrystals possess the cubic "rock salt" crystal structure of their bulk counterpart.[90] The crystalline arrangement of atoms is enclosed by planar facets (and edges with some degree of curvature) that are characteristic of that material type, and the facets are designated by their Miller indices.[91] As depicted in Fig. 1.10, a PbSe nanocrystal's morphology resembles the cubic crystal

structure from which it is derived. However, the synthetic reaction conditions and controlled surface chemistry ultimately play a large role in the resulting morphology.

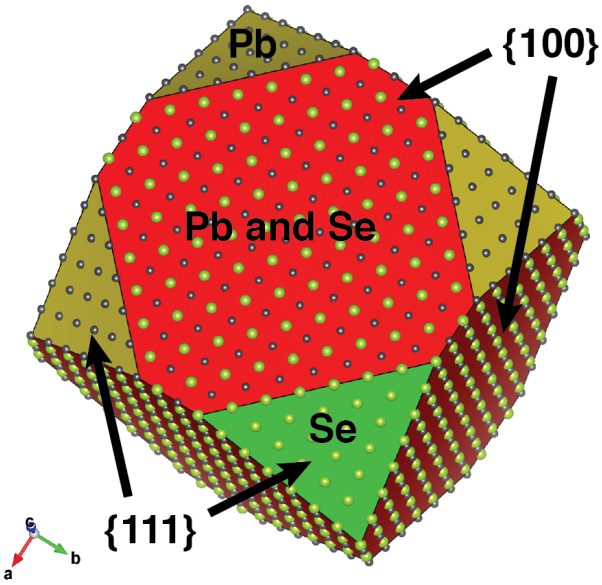

Figure 1.10 A ~5 nm PbSe nanocrystal with two facet groups highlighted. The {100}-type facets (red) comprise Pb and Se atoms. The {111} planes (four each of yellow, Pb only and green, Se only) intersect the cubic lattice in such a way that either Pb or Se terminate the crystal, not both. The special arrangement of this surface chemistry maintains charge balance.

Before the turn of the 21st century, Paul Alivisatos, having previously worked with Brus at Bell Labs, had established his lab at Berkeley as a powerhouse of nanocrystal research. While being a leader in the investigation of the physical chemistry of nanocrystals,[87,92] Alivisatos's group began experimenting with nanocrystals comprising multiple crystal phases in the mid-1990s.[93] Mews, et al. noted that "half" of their product was a unique polytypic CdS/HgS NC that contained a zinc blende tetrahedral core and epitaxially grown wurtzite domains on the core's four facets. This system laid the groundwork for further investigations by the Alivisatos group on morphology and phase

control, with several seminal papers appearing at the turn of the 21st century (see publications by Peng, et al. and Manna, et al.).[94,95]

Control of morphology and phase go hand in hand in much of this research, as exploiting the anisotropic crystal structure of wurtzite (hexagonal) cadmium chalcogenides (and other materials with similar crystallographic characteristics) is crucial for one-dimensional growth. It is now known that phosphonic acid impurities in technical grade (90%) trioctylphosphine oxide (TOPO) are key in stabilizing the lateral facets of cadmium chalcogenide nanorods.[96] Additionally, the structural similarity between the zinc blende {111} and wurtzite {001} facets (see Fig. 1.11) was exploited by the Alivisatos group to grow polytypic tetrapods of the cadmium chalcogenides with ZB cores and WZ arms.[97] In the case of tetrapods, ZB cores are synthesized separately and injected into a reaction mixture that favors WZ Cd-chalcogenide growth, as developed by Talapin, et al.[98] Interestingly, using a WZ seed (instead of ZB) yields a single WZ nanorod-shelled core. This nanorod core/shell synthesis is the basis for many nano-heterostructure applications

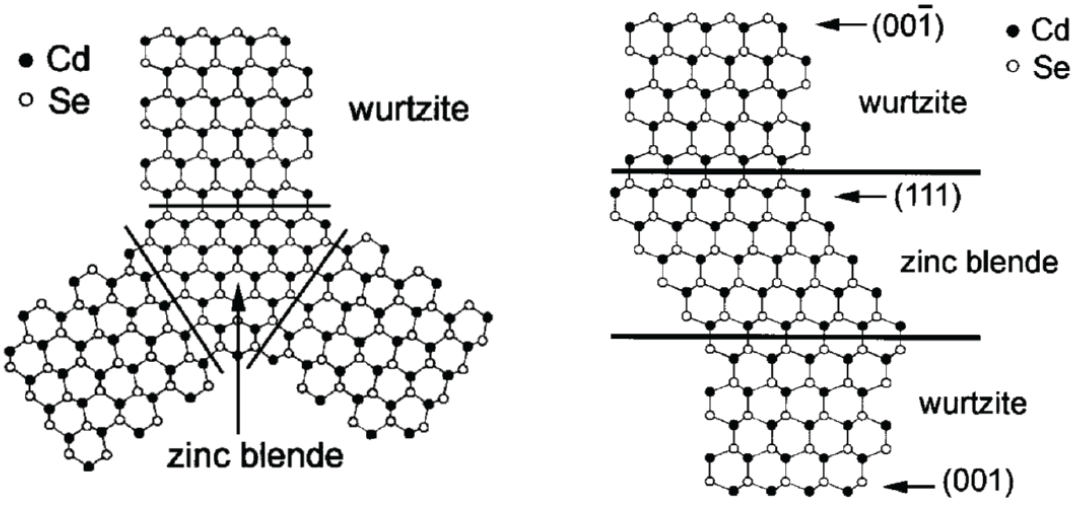

Figure 1.11 Two-dimensional representation of the polytypic nanocrystals synthesized by the Alivisatos group. This figure highlights the fortuitous similarity between the zinc blende {111} and wurtzite {001} facets, which allow for the growth of the tetrapod arms from the core NC. Reprinted with permission from Manna, L., et al. *J. Am. Chem. Soc.* **2000**, *122*, 51 12700-12706. Copyright 2000 American Chemical Society.

that benefit from the spatial separation of charge (mentioned previously) or the larger absorption cross-section the nanorod shell affords (aiding in photon absorption for photoluminescence applications).[84,99] Additional discussion on the history of morphological control as it relates to the copper(I) sulfide NC system is contained in Chapter 2.

At a lower (granular) level of fundamental research, there is still debate over what actually dictates nanocrystal phase in a synthetic environment. There are two prominent schools of thought here. The first subscribes to a transition from a metastable phase to the thermodynamic phase based on Ostwald's "Rule of Stages" during nanocrystal synthesis. Geoffrey Strouse's group found evidence that stacking faults due to fast growth after nucleation would facilitate the transition of kinetically-trapped ZB to thermodynamically-favored WZ in CdSe.[100] They were able to control the growth of both cubic ZB and hexagonal WZ CdSe NCs from 2 to 14 nm, finding that limiting the growth rate (and therefore defects) through precursor concentration was essential for maintaining the kinetically-trapped ZB phase. The second school of thought points to the minute energy differences between phases (like ZB and WZ),[101] and have provided evidence that ligand binding mode[102] and ligand alkyl chain length (which varies the efficiency of adsorption to the NC surface)[103] contribute to the favorability of and allow the power to synthesize one phase over the other. The work presented in Chapters 3 and 4 covers the direct synthesis of a new copper(I) selenide phase, copper(I) telluride NCs of various morphologies, and investigates the synthesis dynamics of those systems.

1.3 Discussion of Powder X-ray Diffractometry (XRD)

Powder X-ray diffractometry is an important instrument in the nanomaterials chemist's toolbox because XRD is crucial in identifying a material's phase. A modern XRD instrument comprises an X-ray source and a detector designed to sense X-rays that reflect from a crystalline sample. As shown in Fig. 1.12, when a simple powder XRD experiment is performed, the source and detector move radially around the sample (at angle θ), and the sample is bombarded with collimated (or divergent, depending on setup) X-rays of a monochromatic wavelength (λ). The crystalline material will constructively reflect the incident X-rays into the detector at specific source/detector positions. A given crystalline material may constructively reflect the incident X-rays at a number of different 2θ angles ($\theta_{source} + \theta_{detector} = 2\theta$, the "diffraction angle"), and these reflections are intrinsic characteristics of that material.

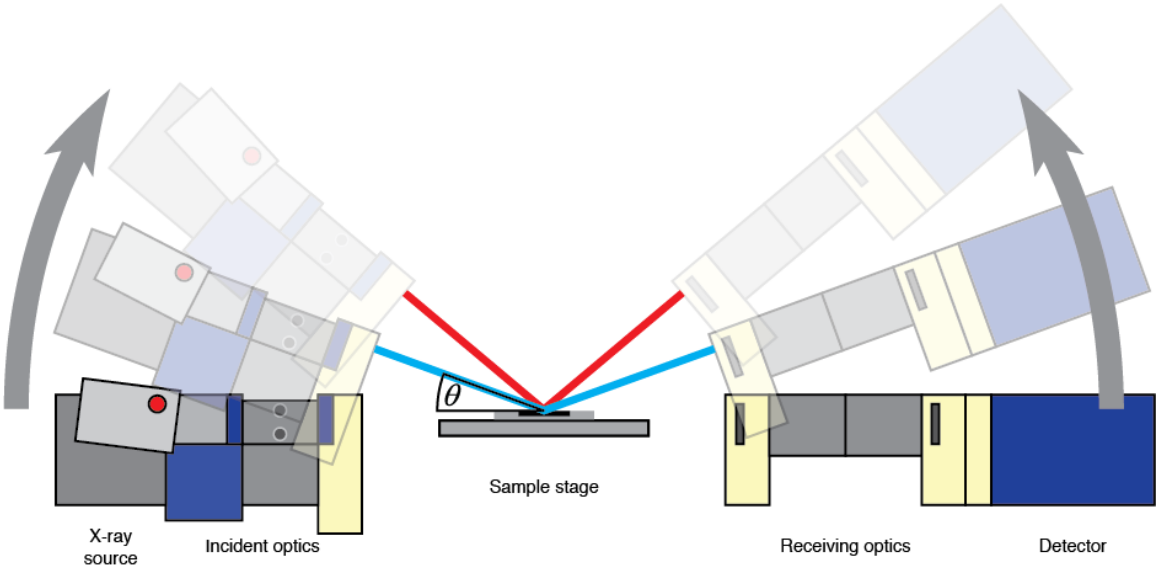

Figure 1.12 Depiction of X-ray diffractometer hardware including the X-ray source, sample stage and detector. As a typical powder XRD experiment progresses, the X-ray source and detector increase in angle θ relative to the planar sample. The detector counts the number of X-rays that reflect from the sample surface (in addition to a non-zero quantity of scattered X-rays from other sources) as a function of θ.

The lattice planes of the crystalline powder are the key to the constructive interference of the reflected X-rays (see Fig. 1.13). Similar to the crystal facets discussed

in section 1.2.3, crystalline materials comprise repeating layers of atoms designated by their Miller indices. The distance between these layers is known as a *d*-spacing. The Bragg equation (eq. 2)[104] mathematically links the *d*-spacing of a material's lattice plane to the θ angle at which the reflected X-rays constructively interfere:

$$n\lambda = 2dsin\theta \tag{2}$$

Therefore, when an X-ray source of known wavelength λ is used to characterize a material, the lattice spacings can be deduced from the reflections' diffraction angles. Additionally, the resulting XRD pattern is comparable with patterns obtained on different instruments, though different X-ray sources have different λ, and this affects the angle of reflectance. Note that the variable *n* is an integer known as the order of reflection, and is typically 1. Higher order values deal with equivalent lattice planes (i.e., (001) and (002)) that constructively reflect X-rays at different (but nonetheless predictable through the Bragg equation) θ values.

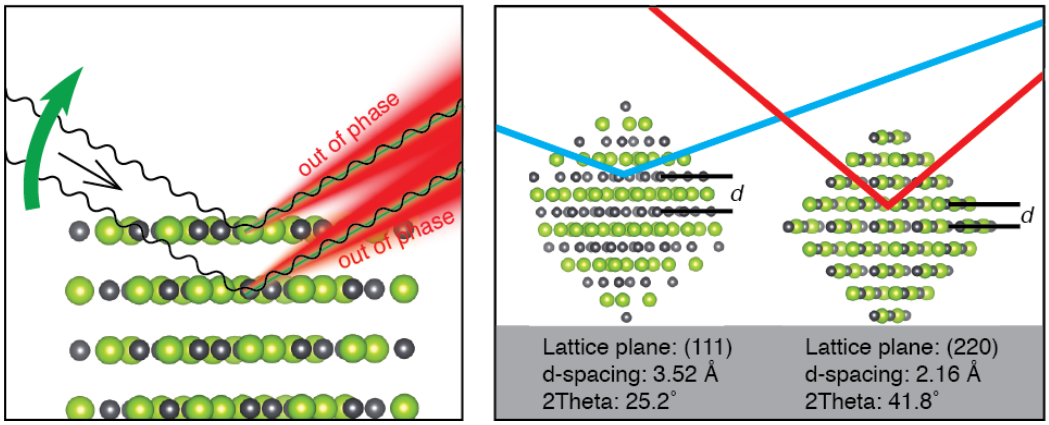

Figure 1.13 Illustrations of powder XRD concepts using cubic PbSe nanocrystals. On the left, as the X-ray source and detector sweep through θ, the X-ray detector will only pick up a signal under the correct circumstances. The reflected X-rays must constructively interfere with one another, satisfying the Bragg equation for the relevant d-spacing. Outside of the specific 2θ angle, the reflected X-rays are out of phase and destructively interfere with one another, preventing the detector from observing a signal. On the right, two PbSe NCs are oriented with [111] and [221] normal to the XRD's sample stage. These lattice planes generate a diffraction signal at markedly different 2θ angles, and this is due to the difference in d-spacing for these planes.

The result of an XRD experiment, known as a pattern, depicts the X-ray intensity at the detector as a function of 2θ. From this data, the material can be identified using a reference pattern database, the relative proportions of mixed phases can be quantified, the crystallite domain size can be calculated using the Scherrer equation,[105] or it can be determined if the material is crystallographically preferentially oriented.

1.4 Scope of Dissertation

The focus of this thesis is the phase and morphological control of copper(I) chalcogenide nanocrystals. Chapter 2 covers a new route to copper(I) sulfide nanorods through the oriented attachment mechanism. This process made use of the anisotropic crystal structure of the chalcocite phase, and was dependent upon the unique ligand-like properties of 1,2-hexadecanediol, which is typically used as a reducing agent. This synthesis had advantages over previous Cu_2S nanorod syntheses in that it did not rely on cation exchange (no Cd^{2+} is present), and fully stoichiometric chalcocite was the product phase.

Chapter 3 covers the direct synthesis of a new copper(I) selenide phase through the use of a diselenide precursor. The wurtzite phase of $Cu_{2-x}Se$ had been observed once previously through a cation exchange with CdSe.[106] The chapter discusses the reaction products when a selenol was used in place of the diselenide, which resulted in the thermodynamic cubic phase. Using variable temperature XRD, the phase dynamics of the kinetically trapped wurtzite phase were probed at higher temperatures. Additionally, the selenol precursor was used in the synthesis of other semiconductor nanocrystals in an effort to explore phase control in other systems.

Chapter 4 discusses the application of a ditelluride precursor to synthesize $Cu_{2-x}Te$ nanocrystals of different phases, and also explores morphological control of that system. Depending on the reaction conditions, the pseudo-cubic metastable $Cu_{1.5}Te$ was primarily obtained with a cube-like morphology. In a non-coordinating solvent and at moderate temperature, nanosheets of what appeared to be CuTe (Vulcanite) were also seen.

Chapter 5 covers the syntheses of additional metal selenides using selenol and diselenide precursors, and the attempted synthesis of monovalent copper sulfide nanoclusters. The chapter also briefly discusses a charge transfer investigation of various $Co^{2+/3+}$ complexes with vastly different self-exchange rates. It was hypothesized that differences in reorganization energy (and therefore self-exchange rate) would affect charge transfer between these Co complexes and fluorescent quantum dots.

Chapter 6 concludes the thesis and contains a summary of the work contained herein, discusses possible future directions, and an outlook on the broader field of nanomaterials chemistry.

Chapter 2

CONTROLLED SURFACE CHEMISTRY FOR THE DIRECTED ATTACHMENT OF COPPER(I) SULFIDE NANOCRYSTALS

2.1 Abstract

This chapter discusses a new route to stoichiometric low chalcocite copper(I) sulfide nanorods without the need for cation exchange. Nanorods are formed through the oriented attachment of seed nanocrystals with crystal-bound thiols facilitated by 1,2-hexadecanediol (HDD). Evidence suggests that rather than acting as a reducing agent, the HDD serves as a nanocrystal stabilizer. Nanorod syntheses attempted without HDD result in ripened and aggregated particles, while reactions performed with an excess of HDD result in solitary unaltered nanocrystals. When the optimal concentration is used, HDD coordinates to the reactive c-axis facets limiting seed ripening and disordered aggregation, without hindering oriented attachment. XPS analysis reveals similar surface chemistry and XRD verifies the same crystal structure between the seed nanocrystals and the final nanorod product.

2.2 Introduction

Ever-growing demand on our traditional energy resources makes harnessing underutilized alternative energy sources all the more necessary and desirable to the scientific community.[107] Colloidal copper(I) sulfide nanocrystals (NCs) are an attractive photovoltaic device component due to their solar absorption characteristics;[108] Cu_2S is a p-type semiconductor with a bandgap reported from 1.1 to 1.4 eV, and an absorption

coefficient of 10^4 cm^{-1}.[109] Cu_2S is also a parent material to ternary and quaternary copper sulfides such as $CuInS_2$ which has emissive defects that can be used for LED lighting, biomedical applications and solar concentrating.[110]

The light-absorbing characteristics of copper(I) sulfide can be further enhanced by morphologies that increase the absorption cross-section of the nanocrystals. Manipulating reaction mixture additives can generate highly faceted Cu_2S nanocrystals,[111] and careful stabilizer control has been used previously to make Cu_2S nanoribbons from nanocrystal assemblies in aqueous media.[112] Sadtler *et al*. were first to synthesize Cu_2S nanorods through cation exchange with CdS nanorods, a process that lacks atom economy and generates a cadmium byproduct.[113] Additionally, the cation exchange process likely leaves the Cu_2S doped with Cd ions. Kruszynska *et al*. discovered that substoichiometric $Cu_{2-x}S$ nanorods could be grown from nucleations when using *tert*-DDT as a ligand and sulfur source,[114] but the fully stoichiometric Cu_2S was not achieved. Further developments to prepare rods structures without cadmium and of controlled stoichiometry are needed.

The oriented attachment of Cu_2S seed particles into larger single crystalline structures offers a means to obtain nanostructures with morphologies, sizes and compositions that may not be possible with traditional monomer-based growth. Oriented attachment of PbSe performed by Cho[115] and later by Koh[116] produced nanowires, nanorings, and nanorods from single-particle building blocks. Oriented attachment has also been used to create single-crystalline chains of TiO_2 crystals,[117] CdTe nanowires,[118] and nanorods of ZnO,[119] CdS and Ag_2S.[120] The process occurs due to dipole interactions between particles. Hexagonal-like crystal structures (as seen in ZnO, CdS and Ag_2S) inherently have a dipole due to crystal structure anisotropy, yet control over the surface

chemistry was essential to orchestrate the directed attachment in many of these cases. The room temperature crystal structure of stoichiometric Cu_2S (low chalcocite) and substoichiometric crystal structure djurleite ($Cu_{1.96}S$) consist of copper atoms arranged around a distorted hexagonally-close-packed sulfur sub-lattice[121] (approximated here for simplicity by the hexagonal high chalcocite structure). Provided the surface chemistry can be effectively controlled, this structural anisotropy leaves the door open for the oriented attachment of Cu_2S.

Our group's research has shown that Cu_2S nanocrystals synthesized with alkanethiols acting as both the ligands and sulfur sources result in the ligand alkanethiolate sulfur atoms becoming integrated into the crystal lattice. These "crystal-bound" thiolate ligands have sulfur atoms that sit in high-coordination-number sites, and are resistant to ligand exchange and photooxidative disulfide formation.[56,62] Robust ligand binding in Cu_2S nanocrystals has enabled the selective cleavage of ligands at higher temperatures and deposition of metal on exposed edge sites, resulting in nanoscale inorganic cages.[57,122] Higher synthesis temperatures result in cleavage of the surface ligands through a breaking of the C-S bond.[62,123] The Kolny-Olesiak group observed that rods could be grown in the direction of crystallographic anisotropy (corresponding to the c-axis of chalcocite) using *t*-DDT as the sulfur source, suggesting that the c-facet can be selectively activated. This highly defined surface chemistry where ligands are not labile and are cleaved at specific temperatures is an opportunity to develop oriented attachment-based syntheses for Cu_2S.

Here we present a new synthetic route to Cu_2S nanorods in which copper sulfide NCs with crystal-bound ligands are joined through the mechanism of oriented attachment in the presence of 1,2-hexadecanediol (HDD) (Figure 2.1). Often seen in nanocrystal literature as a reducing agent,[124] evidence discussed herein suggests that HDD functions as a nanocrystal stabilizer necessary to the oriented attachment process. It was found that control of the concentration of HDD was critical to successful directed attachment of

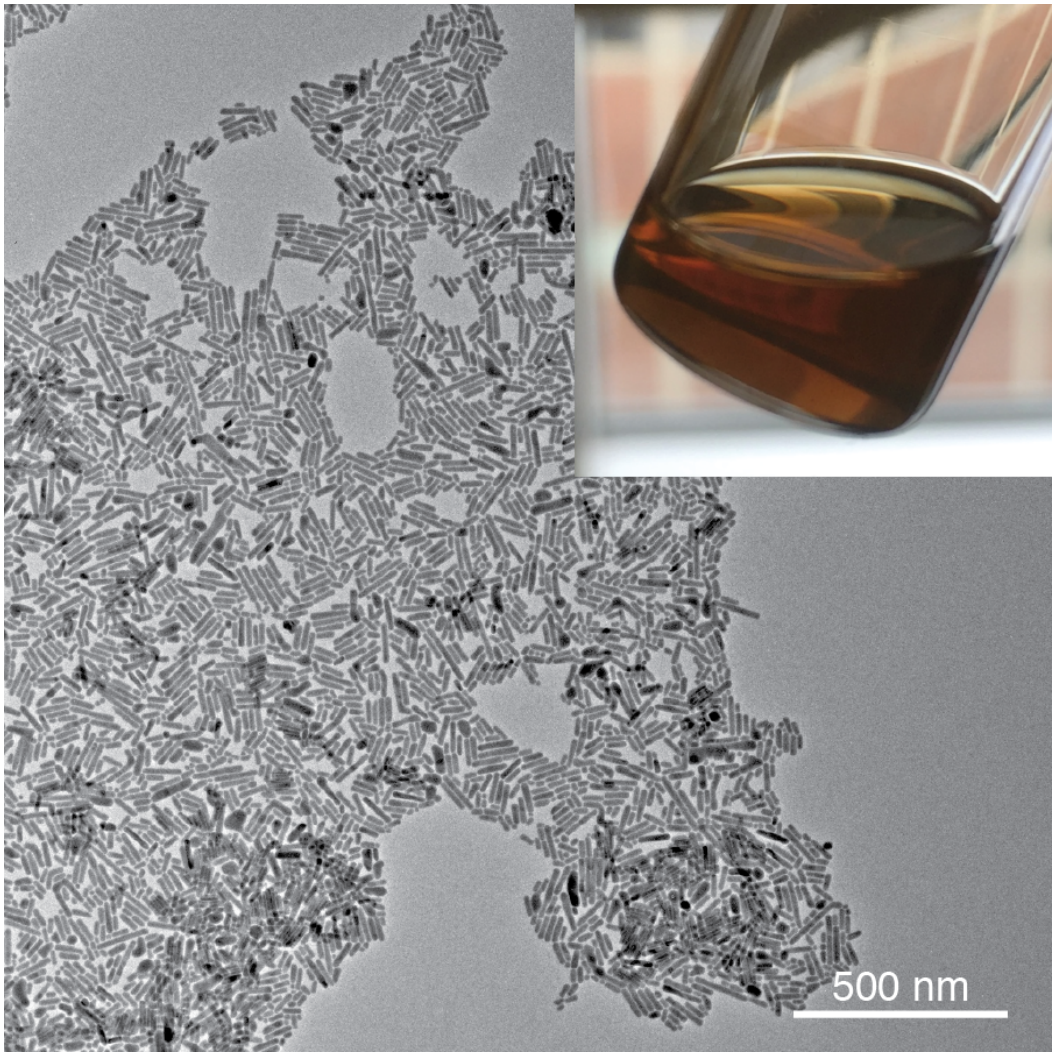

Figure 2.1: TEM image of Cu_2S nanorods synthesized through oriented attachment, inset: photograph of Cu_2S nanorod solution in $CHCl_3$. This particular batch of rods was synthesized with 12.0 ± 1.0 nm seed particles (N = 158), and the final rod dimensions were: width 13.0 ± 1.2 nm and length 44 ± 22 nm (N = 101). Reprinted with permission from Robinson, E. H., et al. *Chem. Mater.* **2017**, *29* (9), 3854. Copyright 2017 American Chemical Society.

nanocrystals in nanorod syntheses, and that the nanorod product had surface chemistry and a crystal structure similar to the constituent NCs.

2.3 Results and Discussion

Prior to the nanorod synthesis, monodisperse quasi-spherical seed nanocrystals with crystal-bound thiol ligands were prepared using a modified literature synthesis.[53] Briefly, $Cu(acac)_2$, 1-dodecanethiol (DDT) and dioctyl ether (DOE) were heated under inert atmosphere to 215 ˚C for one hour. The 12-14 nm seeds were then transferred into a glovebox and purified. For the nanorod synthesis, ~3.7×10^{15} NCs were then heated in 3 mL DOE with HDD (50 mg, 193 μmol) for one hour and subsequently washed with polar solvents to remove unreacted precursors. The seed NCs had a native crystal-bound DDT surface density of 3.7 molecules/nm^2 as determined by thermogravimetric analysis; 50 mg of HDD equates to more than 50 molecules/nm^2 (experimental methods section contains experimental details and ligand density calculations).

Figures 2.2A & B show TEM images of the seed nanocrystals and nanorods which have a diameter of 12.0 ± 1.0 nm and 13.0 ± 1.3, respectively. The rod length distribution at 20 minutes of reaction time (Figure 2.2C) has peaks at regular size intervals, which is a

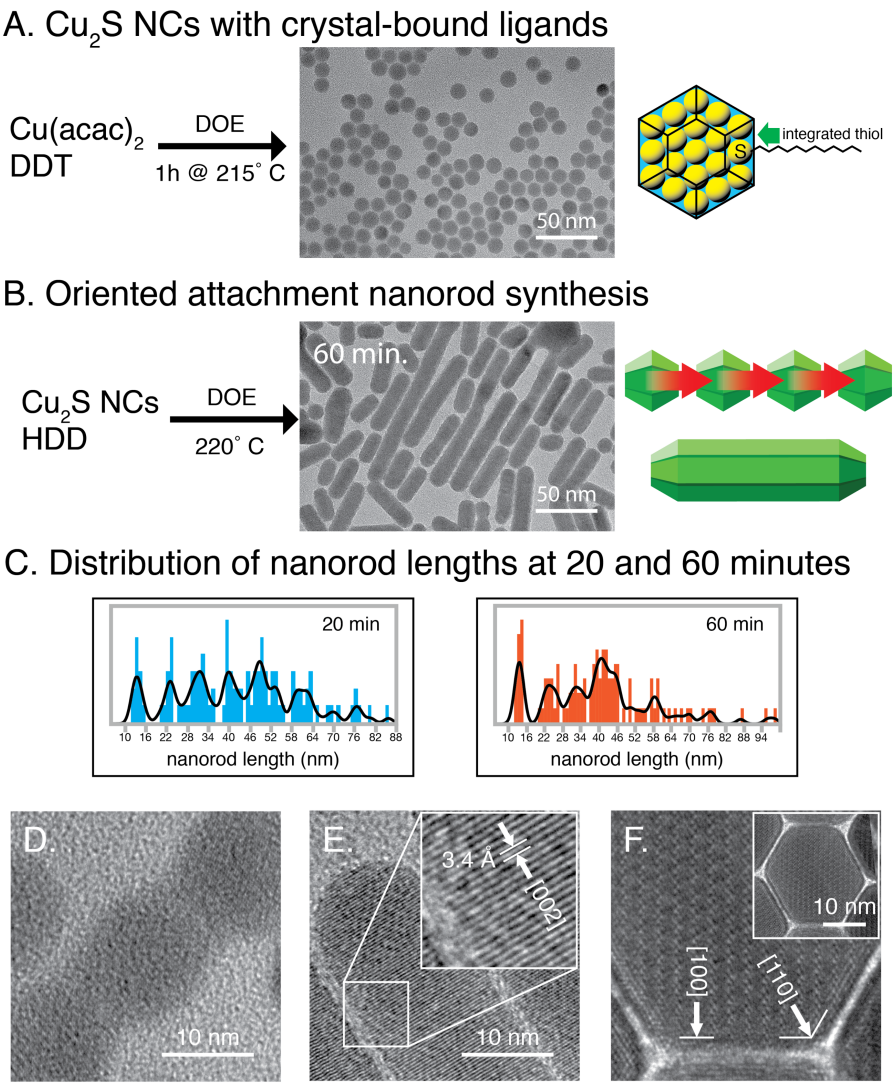

Figure 2.2. (A) Synthesis of Cu_2S seed nanocrystals with crystal-bound ligands; (B) oriented attachment of seed nanocrystals forming nanorods. Distributions in (C) display measured nanorod lengths at 20 minutes (average length: 42 ± 18 nm, N = 109) and 60 minutes (average length: 42 ± 23 nm, N = 115) of reaction time. (D) "Peapod" formation seen in nanorod synthesis, (E) lattice fringing showing growth along chalcocite c-axis, (F) faceting of close-packed nanorods viewed down the c-axis. Reprinted with permission from Robinson, E. H., et al. *Chem. Mater.* **2017**, *29* (9), 3854. Copyright 2017 American Chemical Society.

hallmark of the oriented attachment mechanism. After 60 minutes of reaction time, the average rod length does not increase, however the distribution loses its regularity due to slight variations in length likely due to ripening. Similarly, the rod diameter increased from

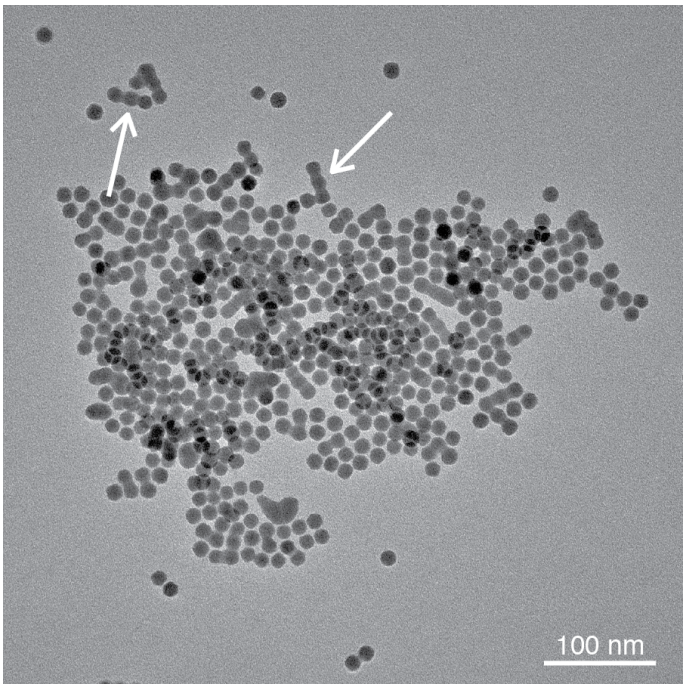

Figure 2.3: TEM image of nanoparticles before ripening obscures the higher surface area "peapod" morphology indicative of oriented attachment. Reprinted with permission from Robinson, E. H., et al. *Chem. Mater.* **2017**, *29* (9), 3854. Copyright 2017 American Chemical Society.

13.2 ± 1.1 to 14.6 ± 1.1 nm from 20 to 60 minutes. Additionally, the number of rods increases with respect to the number of solitary particles (vide infra). TEM images of underdeveloped rod samples show characteristic "peapod" shapes indicative of oriented attachment (Figures 2.2D & 2.3).

Preferential alignment along the chalcocite c-axis is evidenced by FFT of HRTEM of nanocrystals in the process of oriented attachment (Figure 2.4). The nanorods in Figure 2.2E (detail in Figure A2.1) show d spacings of 3.4 Å which correlate to the (002) plane of the high chalcocite crystal structure. Similar to the results of Kruszynska *et al.*,[114] precipitates of nanorod self-assemblies were recovered at the end of the reaction (Figure 2.5). TEM of the nanorods often show self-assembled three-dimensional structures containing on the order of 10s of nanorods. Since the disparity in rod diameter is already quite small (<10%), in future work, increased monodispersity in the lengths could result in more extended self-assemblies (Figure 2.6). FFT of the vertically aligned rods seen in

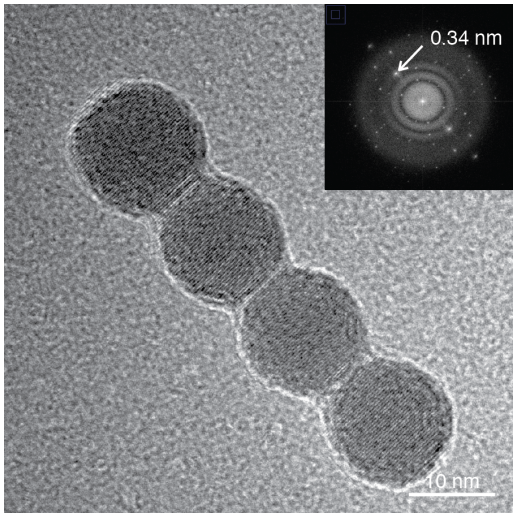

Figure 2.4. High-resolution TEM image of Cu_2S nanocrystals that are undergoing the oriented attachment process. FFT of the entire "peapod" nanostructure indicates that the attachment direction correlates to the c-axis [002] direction of high chalcocite (JCPDS 26-1116). Reprinted with permission from Robinson, E. H., et al. *Chem. Mater.* **2017**, *29* (9), 3854. Copyright 2017 American Chemical Society.

Figure 2.2F reveals the lateral facets are in the {100} family of planes (with additional FFT in Fig. 2.5). The use of air-free techniques after the synthesis results in stoichiometric Cu_2S; UV-Vis absorption analysis of a nanorod solution shows that the rods are not plasmonic

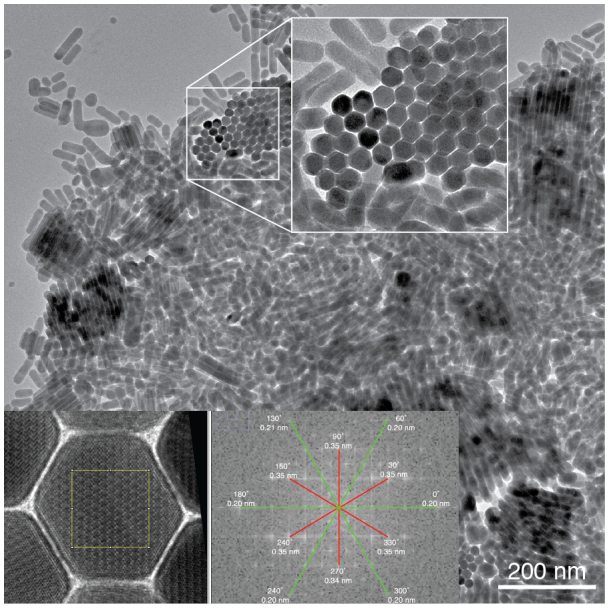

Figure 2.5. TEM image of self-assembled Cu_2S nanorods, top inset shows the faceted lateral sides. Bottom inset shows FFT of vertical nanorods and the identification of lattice planes (JCPDS card # 46-1195). Reprinted with permission from Robinson, E. H., et al. *Chem. Mater.* **2017**, *29* (9), 3854. Copyright 2017 American Chemical Society.

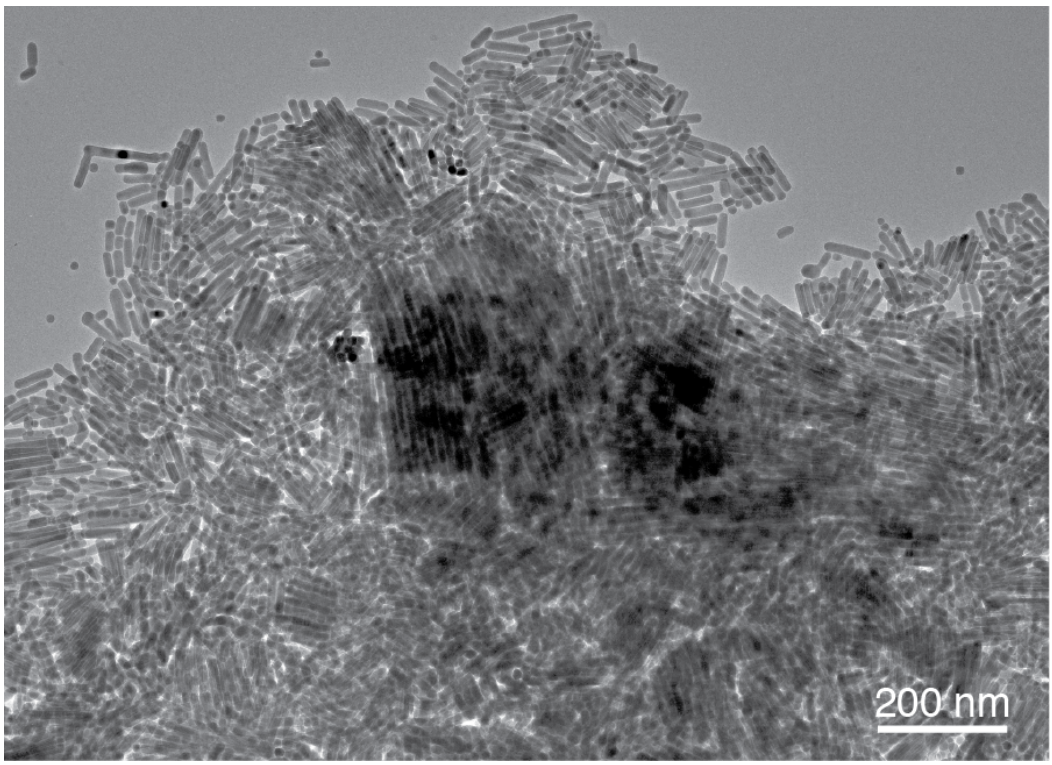

Figure 2.6. TEM image depicting the self-assemblies of nanorods (center top half of image). Rather than forming self-assemblies the height of one nanorod, the structures shown here are stacked in both the short and long directions of the nanorods. Length polydispersity hinders self-assembly and can account for the fact that many nanorod structures are smaller. Reprinted with permission from Robinson, E. H., et al. *Chem. Mater.* **2017**, *29* (9), 3854. Copyright 2017 American Chemical Society.

(Figure 2.7). Furthermore, X-ray diffraction (XRD) of seeds and nanorods confirms that the Cu_2S retains the stoichiometric low chalcocite phase after the synthesis (Figure 2.8A).

A sufficient seed concentration and a synthesis temperature of 220 ˚C were necessary for successful oriented attachment along the chalcocite c-axis. While tuning the length of the nanorods was not a focus in this study, it was observed that lowering the seed concentration by a factor of five resulted in dimers and solitary nanocrystals (Figure A2.2). In the future, this observation suggests that seed concentration could be used to control nanorod length. TGA of the seed particles has shown that organics can detach from the nanocrystal surface at 220 ˚C (Figure A2.3). Correspondingly, at reaction temperatures of 180 ˚C or 200 ˚C, no attachment was observed since the ligands remain stable. At 230 ˚C,

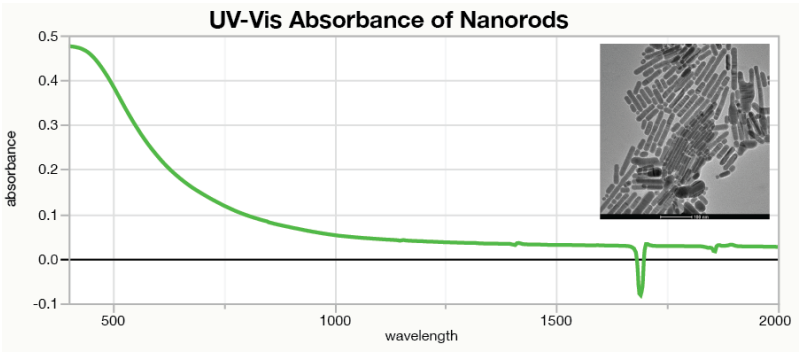

Figure 2.7. UV-Vis absorbance of Cu_2S nanorods in $CHCl_3$. Note the lack of a plasmon in the infrared which would have been indicative of a substoichiometric phase of Cu_2S. Inset: TEM of nanorod sample Reprinted with permission from Robinson, E. H., et al. *Chem. Mater.* **2017**, *29* (9), 3854. Copyright 2017 American Chemical Society.

some oriented attachment was observed at 15 minutes, but after 1h the ripening process and uncontrolled agglomeration had surpassed the organized attachment mechanism resulting in polydisperse nanoparticles. It is likely that 220 ˚C is needed to selectively

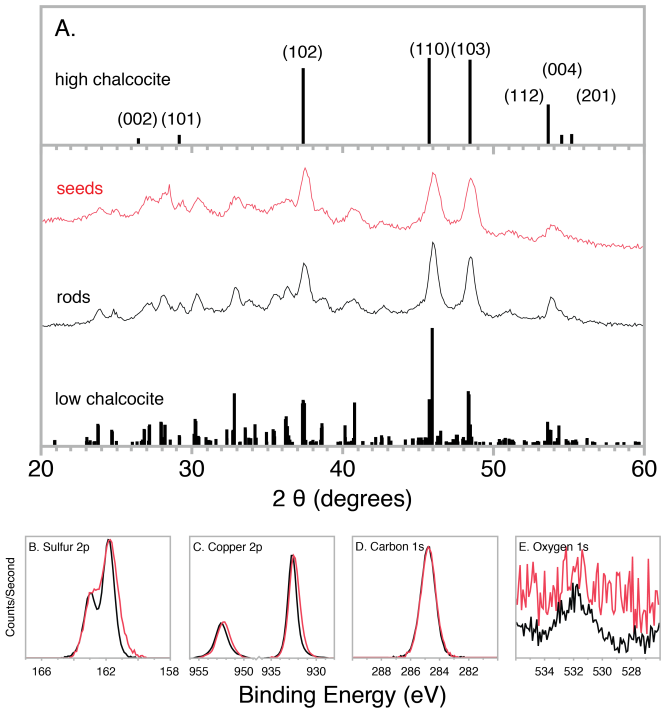

Figure 2.8. XRD and XPS spectra of seed NCs (red) and nanorods (black). (A) XRD of seeds and rods, (bottom) low chalcocite RRUF ID: R120113.9, (top) high chalcocite for reference (JCPDS 26-1116). The large and complex unit cell of low chalcocite causes peak broadening due to closely spaced reflections. This prevents meaningful Scherrer analysis, especially in the important [002]. (B-E) Sulfur 2p doublet, copper 2p doublet, carbon 1s, and oxygen 1s XPS spectra. XPS spectra (except oxygen) have had background signal subtracted and are normalized. Reprinted with permission from Robinson, E. H., et al. *Chem. Mater.* **2017**, *29* (9), 3854. Copyright 2017 American Chemical Society.

cleave the crystal-bound ligands on the metal-rich high energy c-facets, over the lateral {100} facets.

The presence of HDD was also necessary to foster oriented attachment, but only at a very specific concentration. Reactions in which seed nanocrystals were heated in 3 mL DOE without HDD (Figure 2.9) resulted in polydisperse, nebulous particles due to ripening and disordered sintering. When a ratio of 50 molecules/nm^2 (of spherical Cu_2S surface area) was used, nanorods were formed as seen in Figure 2.9B. Increasing the concentration of HDD by a factor of five resulted in solitary particles that did not change in size (Figure 2.9C, original seed diameter: 13.0 ± 0.4 nm, post reaction: 12.8 ± 0.9 nm). The requirement of an excess of HDD, but not too much, suggests that HDD is involved in an equilibrium process with the surface.

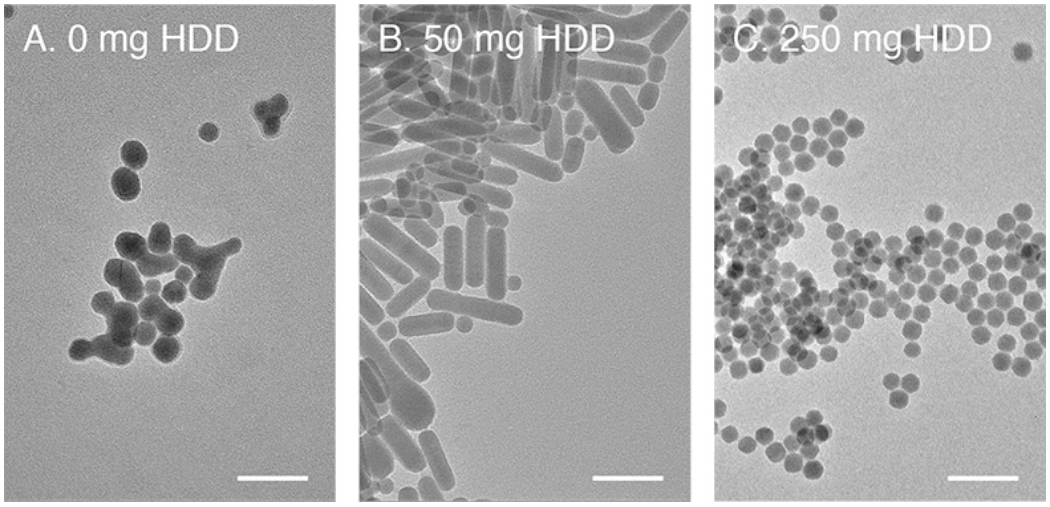

Figure 2.9. TEM images of nanorod reaction products. (A) 0 mg HDD (B) 50 mg HDD (C) 250 mg HDD. Scale bar 50 nm. Reprinted with permission from Robinson, E. H., et al. *Chem. Mater.* **2017**, *29* (9), 3854. Copyright 2017 American Chemical Society.

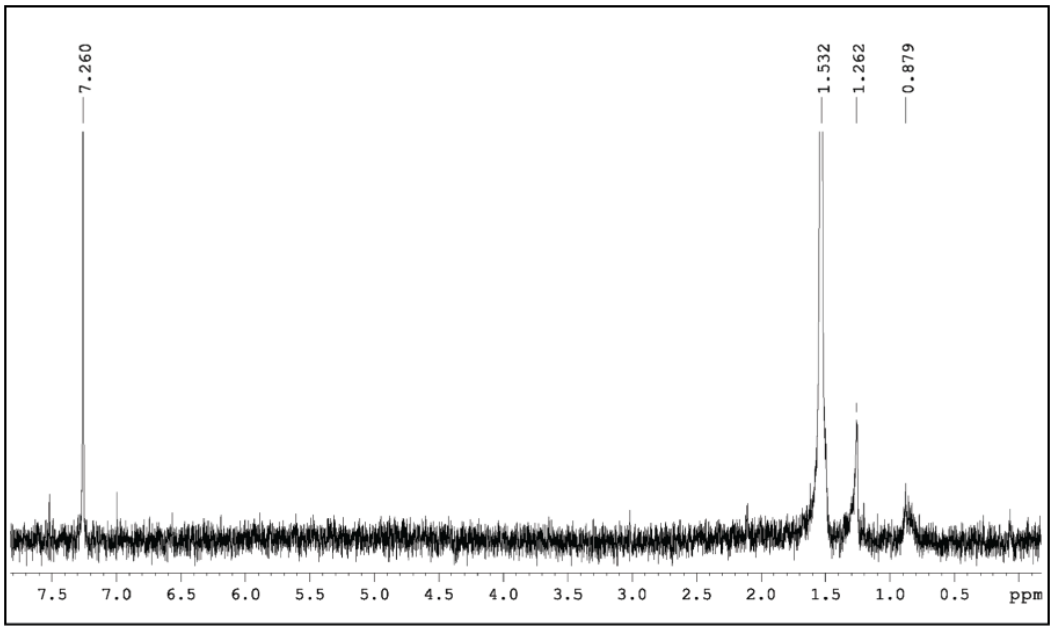

Figure 2.10. ^{1}H NMR of nanorod sample in $CDCl_3$ showing $CHCl_3$ signal at 7.26 ppm, water 1.532 ppm, $-CH_2-$ 1.262 ppm, $-CH_3$ 0.879 ppm. Sample was dried under vacuum on a Schlenk line prior to the addition of $CDCl_3$, and the nanorod concentration was approximately equivalent to 187.5 μmol Cu. The broad signal could be due to characteristic broadening of organics bound to nanoparticles. Additionally, if the nanorods are forming any self-assemblies in solution, the ligand signal may be diminished. Reprinted with permission from Robinson, E. H., et al. *Chem. Mater.* **2017**, *29* (9), 3854. Copyright 2017 American Chemical Society.

The hypothesis that the specific role of HDD is to act as a surface ligand is notable, as it is most commonly employed as a reducing agent in nanocrystal syntheses. We found no evidence of the products of HDD oxidation in a gas chromatography analysis of the post-reaction mixture (see Experimental Section) and there was no reduction in the concentration of HDD. ^{1}H NMR of a nanorod solution shows broad aliphatic CH_2 and CH_3 signatures indicative of long chain aliphatic ligands bound to a surface[125] (Figure 2.10). The peak broadening results from the slow tumbling rate of the nanorods and only signals from the outermost protons are observed. Since the concentration of free HDD does not change, we concluded that the nanocrystals continue to be capped with crystal-bound dodecanethiol, rather than having undergone extensive ligand exchange to HDD.

XPS analysis was used to further interrogate the changes in the surfaces of the seeds and rods. Figures 2.8B through E compare XPS spectra of seed nanocrystals with crystal-bound thiol ligands (red trace) and nanorods (black trace) which both have the characteristic narrow crystal-bound spectra; Cu_2S NCs with crystal-bound ligands have notably narrow S 2p signals as there are only Cu_2S "type" sulfurs. There are no low coordination (or surface-bound) thiolates, which have a higher binding energy.[62] After the reaction, the S 2p and Cu 2p peaks narrow by losing low binding energy components. We attribute this change in surface chemistry to a change in faceting from a large portion of {101}- and {001}-like facets exposed in the seeds, to predominantly {100} facets in the rods. A small oxygen 1s peak appears in the nanorod sample and could be due to HDD or a DOE remnant after the nanocrystals were cleaned. The small oxygen XPS peak in comparison to the large carbon signal is further evidence that HDD is not a major component of the nanorod ligand corona.

The quantitative elemental XPS percentages in Figure 2.11 reveal a relative loss of carbon upon rod formation. This may be due to variations in the adventitious carbon, but are also consistent with the decreased surface to volume ratio of the nanorods and consequent decreased number of ligands present. The surfaces of the Cu_2S are sulfur-rich according to the surface-sensitive XPS which show a Cu:S ratio of 1.63:1 and 1.75:1 in the seeds and rods, respectively. The increase in the surface copper to sulfur ratio detected with XPS is possibly due to the change in faceting. Based on the high chalcocite crystal structure, the seed nanocrystals have a large proportion of {101} and {001} facets, whereas the rods present a large portion of {100}. The differences in surface chemistry can be visualized in Figure 2.12, using the structure parameters of Will, et al.[126,127] In the (100)

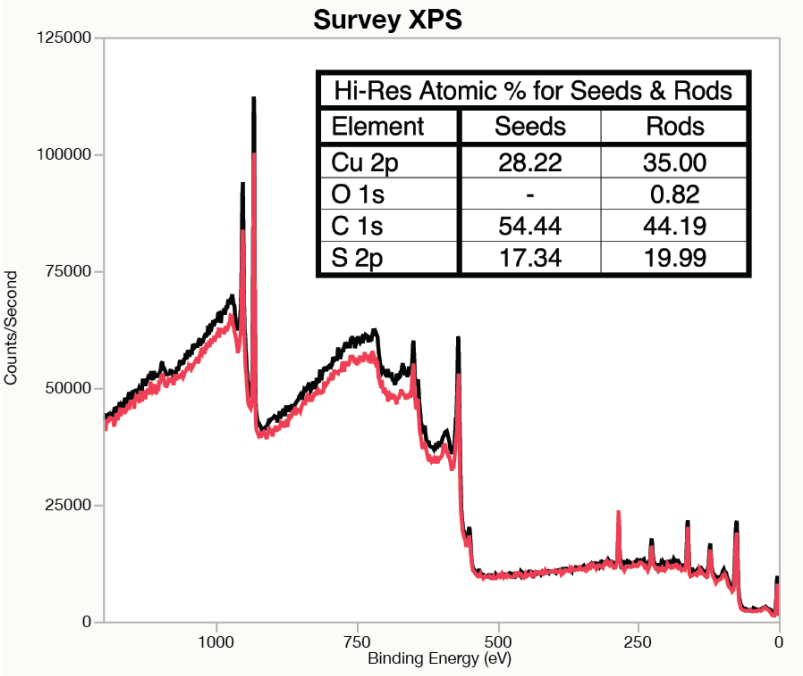

Figure 2.11. XPS survey spectrum of seed nanoparticles (red) and nanorods (black). Inset: atomic percentages of copper, oxygen, carbon and sulfur based on the high-resolution spectra in Figure 2.4. Reprinted with permission from Robinson, E. H., et al. *Chem. Mater.* **2017**, *29* (9), 3854. Copyright 2017 American Chemical Society.

case (left, representing lateral nanorod facets), the ratio of Cu:S is 0.695:1, while in the (101) case (right, representing seed particle facets), the Cu:S is 0.518:1, relative to the Cu occupancy. Below the first layer of these planes, the presence of stoichiometric Cu_2S increases the Cu contribution relative to S in the XPS. However, XPS is surface sensitive,

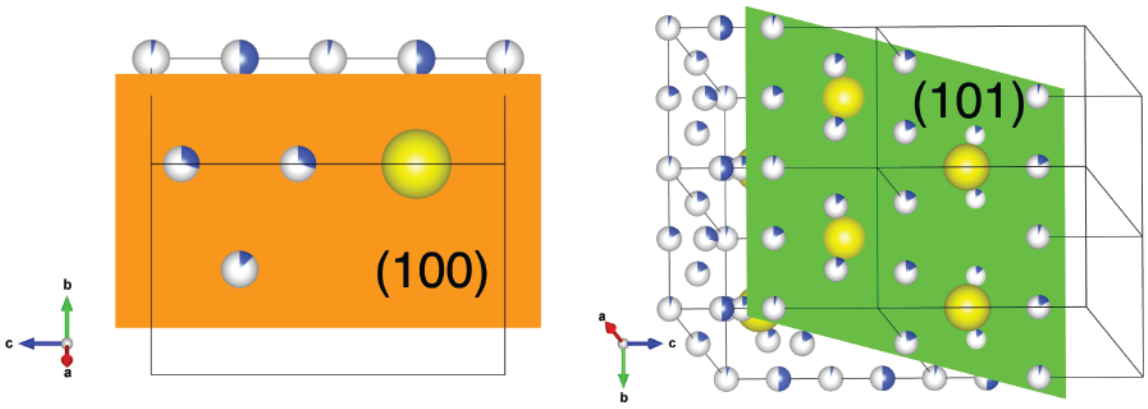

Figure 2.12. Two depictions of the high chalcocite crystal structure based on the structure parameters from Will, et al. rendered in VESTA. In these unit cells, planes in the [100] and [101] with the highest concentration of sulfur atoms are shown. Reprinted with permission from Robinson, E. H., et al. *Chem. Mater.* **2017**, *29* (9), 3854. Copyright 2017 American Chemical Society.

and on these topmost layers this subtle difference in stoichiometry could explain the Cu:S ratio described in Figure 2.11.

The sum of these observations lead to the conclusion that at 220°C, the crystal-bound ligands on the c-facets of the seeds are selectively cleaved through irreversible C-S bond cleavage.[123] Without the presence of another stabilizing ligand, the newly exposed high energy surface catalyzes morphological changes and uncontrolled sintering of the particles. In the presence of HDD, a weak diol ligand, the surface is stabilized, preventing these changes. The binding of HDD is in equilibrium with free HDD in solution, so that when an excess of HDD is used, the equilibrium is shifted to "on" and no oriented attachment can occur due to a strong passivation. When a middle ground is found, dipole interactions between particles enable nearby nanocrystals to push through the less-dense HDD barrier and attach along the high chalcocite c-axis. A temporal study of the nanorod synthesis shown in Figure 2.13 reveals that rods continuously form over the course of the

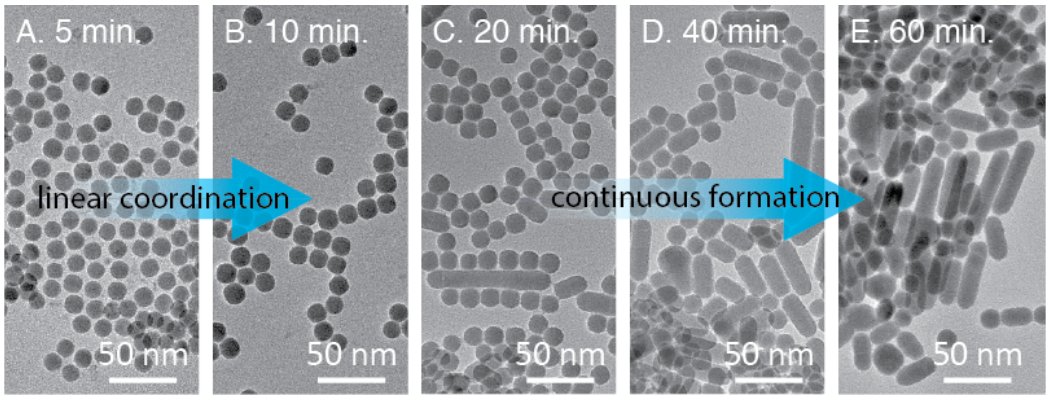

Figure 2.13. A temporal study of an oriented attachment nanorod synthesis with aliquots taken at 5, 10, 20, 40 and 60 minutes after the reaction reached 220 ˚C. From 5 to 10 minutes, the Cu_2S seed nanocrystals begin to linearly coordinate with one another. At 10 minutes, there may be a slight morphological change in which the c-axis facet area is enhanced in the seeds, increasing the dipolar attraction between nanocrystals. From 20 to 60 minutes, the number of rods begins to increase and the number of solitary seeds begins to decrease as more seeds attach with one another. In this synthesis, the seeds were 13.1 ± 0.7 nm and the rod dimensions (length, width) were: 20 min.: 37 ± 15 nm, 13.5 ± 1.0 nm, N = 147; 40 min.: 41 ± 19 nm, 14.3 ± 1.3 nm, N = 143; 60 min.: 37 ± 12 nm, 14.0 ± 1.0 nm, N = 189. It is apparent that the attachment process is continuously occurring over the course of the reaction as solitary nanocrystals meet in solution. However, once a rod is formed, it is removed from the pool of available material likely in the self-assemblies seen in Figures 2.5 and 2.6. Thus, the average rod length does not change while the prevalence of rods is higher in later aliquots.. Reprinted with permission from Robinson, E. H., et al. *Chem. Mater.* **2017**, *29* (9), 3854. Copyright 2017 American

reaction rather than in one event. The study also suggests that the rods are removed from the pool of available material (in self-assemblies) after oriented attachment, as evidenced by the consistent average nanorod lengths seen at 20, 40 and 60 minutes of reaction time.

For comparison, oleylamine (OlAm) was substituted for HDD under the same nanorod synthesis conditions. The results of this experiment, seen in Figure 2.14, show that the binding of OlAm to the surface of the Cu_2S nanocrystals in a markedly different manner from HDD and thus alters their shape through lateral ripening rather than oriented attachment. OlAm has a preference for the c-axis facets of Cu_2S and binds strongly, a fact that can be exploited to make platelet-shaped nanocrystals.[128] In this experiment, spherical particles doubled in width perpendicular to the c-axis (12.0 ± 1.0 nm to 24.1 ± 2.4 nm),

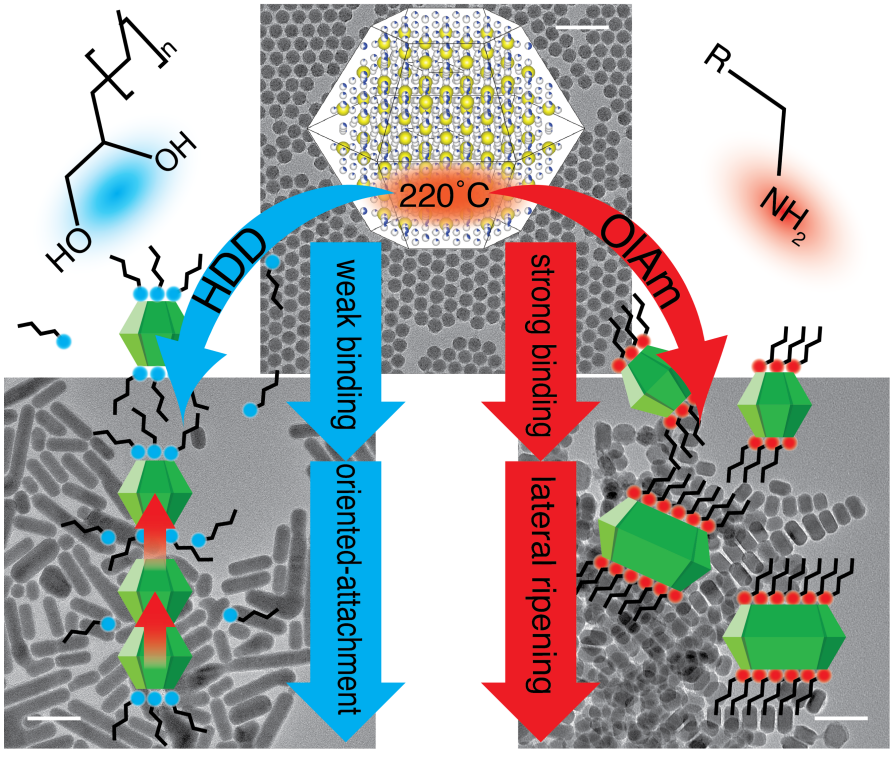

Figure 2.14. Effects of HDD (left) and OlAm (right) on Cu_2S NCs with crystal-bound ligands. Scale bar 50 nm. Reprinted with permission from Robinson, E. H., et al. *Chem. Mater.* **2017**, *29* (9), 3854. Copyright 2017 American Chemical Society.

while growth along the c-axis was negligible (final length: 13.1 ± 0.7 nm). Columnar assemblies seen in the TEM images of this sample highlight copper(I) sulfide's preference for c-axis coordination.[129]

2.4 Conclusion

This chapter has discussed the use of HDD as a weakly binding stabilizer and facilitator of Cu_2S nanocrystal-oriented attachment. Quasi-spherical Cu_2S nanocrystals with crystal-bound ligands were used to synthesize nanorods of similar but slightly ripened diameters. Evidence for oriented attachment was seen in TEM images of peapod-like nanorods and periodic spikes in the distribution of rod lengths. Varying the concentration of HDD had the effect of preventing disordered attachment, and enabled dipole-driven interaction to connect nanocrystals when the quantity of HDD was optimal. Reactions without HDD resulted in ripening and disorganized attachment, while reactions with a high concentration resulted in solitary nanocrystals. XPS of seed nanocrystals and nanorods revealed similar surface chemistry with the nanorods. The FWHM of S 2p and Cu 2p decreased in the rod samples suggesting a homogenization of the nanorod surface states. XRD analysis of the nanorods showed that the low chalcocite crystal structure of the seeds is preserved. To the best of our knowledge, this is the first time colloidal stoichiometric Cu_2S nanorods have been synthesized without cation exchange. Moving forward, it is hoped that while oriented attachment can result in polydisperse nanorod lengths, quantum confinement can be achieved with smaller seeds due to rod/seed diameter correlation.

2.5 Experimental Methods

Materials. Dioctyl ether (DOE, 99%), 1,2-hexadecanediol (HDD, 90%), 1-dodecanethiol (DDT, 98%), were obtained from Sigma-Aldrich. Copper(II) acetylacetonate ($Cu(acac)_2$, >98%) was obtained from Strem Chemicals. Octadecane analytical standard was obtained from Polyscience Corporation. All materials were used as received without additional purification. Air-free Schlenk line (argon) and glovebox (nitrogen) techniques were used throughout the experimental procedure.

Copper(I) Sulfide Nanoparticles. Seed nanoparticles were prepared using a modified literature synthesis from Kuzuya.[53] $Cu(acac)_2$ (5 mmol), DDT (20 mL), and DOE (5 mL) were degassed for one hour then heated to 215˚C under argon for one hour. After cooling the reaction mixture to room temperature, the particles were transferred to a glovebox where the nanoparticle solution was precipitated four times in isopropanol, followed by precipitation in chloroform four times. Formation of superlattices enables precipitation in non-polar solvents.

Determination of Cu_2S seed concentration. The seed nanoparticle/chloroform solution was stored in a sealed vial in a glovebox to prevent oxidation. To determine the concentration,[57] a known volume of the solution was dissolved with the copper-complexing agent neocuproine, and the UV-Vis absorbance was compared with a calibration curve. From the copper concentration in the sample vial the number of nanoparticles in that vial could be extrapolated using TEM images to determine nanoparticle diameter.

Copper(I) Sulfide Nanorods. The oriented attachment synthesis began with degassing 3 mL of DOE, and 50 mg HDD in a three-necked flask for one hour at 50 ˚C. In a glovebox, Cu_2S seed nanoparticles ($3.7*10^{15}$ NCs) dispersed in chloroform were injected into the flask. $CHCl_3$ was subsequently evaporated at room temperature with a Schlenk line, and nanorod synthesis was carried out at 220 ˚C for one hour. This sample was cooled to room temperature and transferred back into the glovebox where it was repeatedly precipitated in isopropanol.

Quantitative Gas Chromatography (GC). Two GC experiments designed to quantify the amount of HDD present in the first nanorod precipitation (cleaning) step using an internal standard (octadecane). HDD is soluble in 2-propanol, so through quantitative weighing of precursors (HDD and DOE) and solvent (2-propanol), any difference between the control sample and the supernatant solution could be observed. In the first experiment, a standard nanorod synthesis was performed and the rods were cleaned with 2-propanol. In the second, HDD, DOE and 2-propanol were mixed at room temperature. The retention times are DOE (8.307 min.), octadecane (9.820 min.) and HDD (12.739 min.). Both samples (the nanorod reaction supernatant and the control) began with the same concentration of HDD. After retrieving the integrations from the GC, the values were inserted into an internal standard calibration curve for HDD and octadecane. The results show that no difference in HDD concentration is seen after the nanorod reaction in comparison with the mixture of precursors; during nanorod cleaning, the HDD is dissolved and transferred into the 2-propanol while the nanorods precipitate.

Characterization. Transmission Electron Microscopy (TEM) was performed on a FEI Technai Osiris™ digital 200 kV S/TEM system. Absorption spectra were obtained on a Jasco V-670 UV-Vis spectrophotometer. Gas chromatography (GC) was performed on a Hewlett Packard HP 6890 Series GC System with a 7683 Series Injector (5 µL injection), a HP 3396 Series III Integrator, and a Supelco SPB-5 24048 GC column (30 m). The injection port was heated to 200 ˚C, and the detector was set to 300 ˚C (FID). Helium was used as the carrier gas at a flow rate of 1.5 mL/min. The GC oven was programmed to dwell at 150 ˚C for 5 minutes then ramp to 250 ˚C at 10 ˚C/min. Thermogravimetric Analysis (TGA) was performed on an Instrument Specialists TGA 1000 with a nitrogen flow rate of 100 cc/min and temperature ramp rate of 2 ˚C/min. X-ray diffraction (XRD) measurements were done using a Scintag XGEN-4000 X-ray diffractometer with a CuKα (λ = 0.154 nm) radiation source. XPS was performed using an Ulvac-PHI Versaprobe 5000.

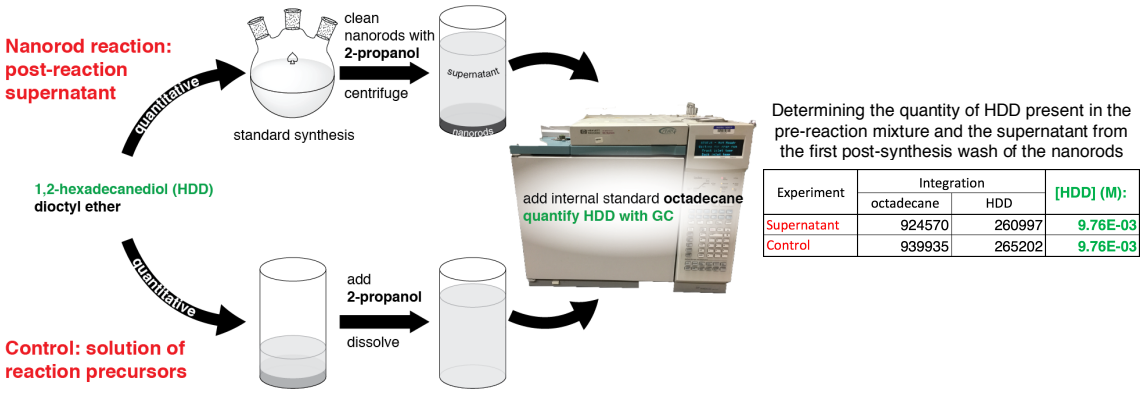

Figure 2.15. Scheme for the quantitative GC experiment. Reprinted with permission from Robinson, E. H., et al. *Chem. Mater.* **2017**, *29* (9), 3854. Copyright 2017 American Chemical Society.

Monochromatic Al Kα x-rays (1486 eV), a 100 µm diameter x-ray spot, and a takeoff angle of 60 degrees from sample normal were used. Pass energies of 187.7 eV and 23.5 eV were used for the survey and high-resolution acquisitions, respectively. 1.1 eV electrons and 10 eV Ar^+ ions were used for charge neutralization. The spectra were calibrated to the C 1s peak at 284.8 eV for sp^3 carbon. A Shirley background was subtracted from the high-

resolution images in Figure 2.8, but in the survey in Figure 2.11 no normalization or background subtraction has been performed. ^{1}H NMR spectra were obtained using a 400 MHz Bruker spectrometer, spectra were calibrated to the residual $CHCl_3$ peak at 7.26 ppm.

Calculating [HDD]/nm². Ratio of 1,2-hexadecanediol per square nanometer of nanocrystal surface area (SA) assuming the nanocrystals have a spherical shape. NC diameter = 13.01 nm, mol mass of HDD = 258.44 g/mol, quantity HDD used in typical reaction = 0.050 g, number of Cu_2S seeds used in a typical reaction = 3.729E15.

$$SA\ per\ NC = 4\pi r^2 = 4\pi(\frac{NC\ diameter}{2})^2 = 4 * \pi * \left(\frac{13.01\ nm}{2}\right)^2 = 531.4\ nm^2/NC$$

$$HDD\ per\ NC = \frac{\frac{g\ HDD\ used\ in\ reaction}{mol\ mass\ HDD} * 6.0221 * 10^{23}\frac{molecules}{mol}}{number\ of\ seed\ NCs\ per\ reaction} = \frac{\frac{0.0500\ g\ HDD}{258.44\frac{g}{mol}} * 6.0221 * 10^{23}\frac{molecules}{mol}}{3.729 * 10^{15}\ seed\ NCs} = 31246\ HDD/NC$$

$$HDD\ per\ nm^2 = \frac{31245\ HDD\ molecules}{531.4\ nm^2} = 58.80\ HDD/nm^2$$

Calculating density of crystal-bound DDT molecules. Based on TGA (refer to Figure S9) the total sample mass = 5.5727 mg, mass that vaporized from 186.43 ˚C to 258.28 ˚C = 0.443 mg, mass of Cu_2S is 5.13 mg. The high chalcocite unit cell has 2 sulfur atoms and 4 copper atoms and a volume of 0.094925 nm^3.[126] Other important values: molar mass of 1-dodecene = 168.319 g/mol, molar mass of Cu = 63.55 g/mol, molar mass of S = 32.06 g/mol. Note: 1-dodecene is released when crystal-bound 1-dodecanethiol is heated to temperatures 200-300 ˚C.[62]

$$Volume\ per\ NC = \frac{4}{3}\pi r^3 = \frac{4}{3}\pi(\frac{NC\ diameter}{2})^3 = \frac{4}{3}\pi(\frac{13.01\ nm}{2})^3 = 1151.9\ nm^3$$

$$dodecene\ vaporized\ in\ TGA = \frac{sample\ mass\ loss}{molar\ mass} * 6.0221 * 10^{23}\frac{molecules}{mol}$$
$$= \frac{\frac{0.443\ mg}{1000\frac{mg}{g}}}{168.319\frac{g}{mol}} * 6.0221 * 10^{23}\frac{molecules}{mol}$$
$$= 1.58 * 10^{18}\ dodecene/TGA\ sample$$

$$mass\ per\ unit\ cell = \frac{2 * S\ mol\ mass + 4 * Cu\ mol\ mass}{6.022 * 10^{23}\ atoms/mol} = \frac{(2 * 32.06\frac{g}{mol} + 63.55\frac{g}{mol})}{6.022 * 10^{23}\ atoms/mol}$$
$$= 5.29 * 10^{-22} g/unit\ cell$$

$$mass\ per\ nanoparticle = \frac{mass\ per\ unit\ cell}{unit\ cells\ per\ NC} = \frac{5.29 * 10^{-22}\ g/unit\ cell}{\frac{1151.9\ nm^3/NC}{0.094925\ nm^3/unit\ cell}}$$
$$= 6.41\ * 10^{-18}\ g/NC$$

$$\#\ of\ NCs\ in\ TGA\ sample = \frac{mass\ of\ NCs\ in\ TGA\ sample}{mass\ of\ each\ NC} = \frac{\frac{5.13\ mg\ NCs}{1000\frac{mg}{g}}}{6.41\ * 10^{-18}\frac{g}{NC}}$$
$$= 8.00\ * 10^{14}\ NCs/TGA\ sample$$

$$DDT\ per\ nm^2 = \frac{\#\ of\ dodecene\ molecules\ in\ TGA}{SA\ of\ NCs\ in\ TGA\ sample} = \frac{1.58 * 10^{18}\ dodecene/TGA\ sample}{531.4\frac{nm^2}{NC} * 8.00 * 10^{14}\frac{NCs}{TGA\ sample}}$$
$$= 3.73\ DDT/nm^2$$

Chapter 3

DIRECT SYNTHESIS OF NOVEL $Cu_{2-x}Se$ WURTZITE PHASE

3.1 Abstract

This chapter discusses the unprecedented direct synthesis of a recently discovered metastable wurtzite phase of $Cu_{2-x}Se$. Nanocrystals of $Cu_{2-x}Se$ were synthesized employing dodecyl diselenide as the selenium source and ligand. Optical characterization performed with UV−vis−NIR spectroscopy in solution showed a broad plasmonic band in the NIR. Structural characterization was performed with X-ray diffraction (XRD) and transmission electron microscopy. Variable-temperature XRD analysis revealed that the wurtzite nanocrystals irreversibly transform into the thermodynamic cubic phase at 151 °C. Replacement of dodecyl diselenide with dodecyl selenol yielded cubic phase $Cu_{2-x}Se$, allowing for polymorphic phase control. An aliquot study was performed to gain insight into the mechanism of phase selectivity. The direct synthesis of this novel wurtzite phase could enable the discovery of new phenomena and expand the vast application space of Cu_xSe_y compounds.

3.2 Introduction

The phase of a material is critical in determining the properties exhibited. For example, wurtzite and zinc blende CdSe have a direct and indirect band gap, respectively.[130] Similarly, PbO-type FeSe exhibits superconductivity while the NiAs-type does not.[131] However, phase control in the synthesis of polymorphic systems, in particular

access to metastable phases, remains a challenge and is the focus of intense research efforts.[132–139] The $Cu_{2-x}Se$ (x=0-0.2) system is of particular interest because this p-type direct band gap semiconductor can exhibit plasmonic properties, superionic conductivity and low thermal conductivity based on composition.[140–143] These characteristics make this material ideal for applications in solar energy, bioimaging,[144] opto-electronics,[142,145] and thermoelectrics.[146]

Controlling the structure of $Cu_{2-x}Se$ (x=0-0.2) in synthesis presents a challenge because the Cu-Se phase diagram is compositionally rich and additionally includes Cu_3Se_2, CuSe, and $CuSe_2$. Furthermore, bulk and nanoscale $Cu_{2-x}Se$ have been reported to crystallize in monoclinic, tetragonal, orthorhombic, and cubic crystal systems.[141,143,146–148] Recently Gariano et al. synthesized hexagonal Cu_2Se with the wurtzite phase via cation exchange of wurtzite-CdSe with Cu^+.[106] While there is very little known about this novel phase, the anisotropic nature of the crystal system and the high mobility of Cu^+ in copper chalcogenides could enable the discovery of new phenomena and the utilization in applications like those mentioned above. Additionally, wurtzite $Cu_{2-x}Se$ can serve as a host material in cation exchange reactions to access metastable phases of other selenides with unique properties.[149,150]

There have been a few literature reports of direct synthetic control of the crystal structure of Cu_2Se. Liu and coworkers developed a synthetic scheme in which Cu nanowires reacted with TOP:Se yielded tetragonal or cubic phase Cu_2Se based on the reaction temperature.[147] Low et al. employed a solventless thermolysis of a copper(I) phenylselenoate polymer under vacuum or inert atmosphere to obtain orthorhombic or cubic Cu_2Se, respectively.[151] However, the direct synthesis of the hexagonal phase has

remained elusive because current reaction schemes rely on Se precursors, such as TOP:Se, ODE:Se, and OLAM:Se, that require temperatures ≥ 180 °C to decompose. The higher temperatures likely facilitate formation of the thermodynamic phase. The use of diorganyl dichalcogenides in nanocrystal synthesis has gained momentum in recent years and notably often at more moderate synthetic temperatures.[134,139,145,152–156] In particular, the Brutchey group has exploited these synthons to yield the metastable hexagonal wurtzite phases of $CuInS_2$, $CuInSe_2$, and Cu_2SnSe_3.[152] Reported herein is the direct synthesis and characterization of metastable hexagonal wurtzite $Cu_{2-x}Se$ employing didodecyl diselenide (DD_2Se_2) as the Se precursor.

3.3 Results and Discussion

In a typical synthesis, $Cu(acac)_2$ and DD_2Se_2 were mixed in octadecene and heated to 155 °C for 1 hr (see experimental methods section for details). The reaction mixture was cooled down to room temperature and the nanocrystals were separated by centrifugation and purified by washing with acetone. The reaction temperature was selected based on an observed change from a turbid mixture to an optically clear solution indicative of nanocrystal nucleation. Figure 3.1 illustrates the powder XRD pattern of the as-synthesized

Element	Atomic #	Series	unn. C	norm. C	Atom. C	Error (1 Sigma)
			[wt.%]	[wt.%]	[at.%]	[wt.%]
Cu	29	K-series	64.22	64.22	69.04	1.97
Se	34	K-series	35.78	35.78	30.96	1.13

Table 3.1. Quantitative EDS data of wurtzite $Cu_{2-x}Se$ NCs. Copper atomic percent may be higher than expected 66.7% due to precursor material that was not removed during cleaning. Reprinted with permission from Hernández-Pagán, E. A., et al. *Chem. Mater.* **2019**, *31* (12), 4619. Copyright 2019 American Chemical Society.

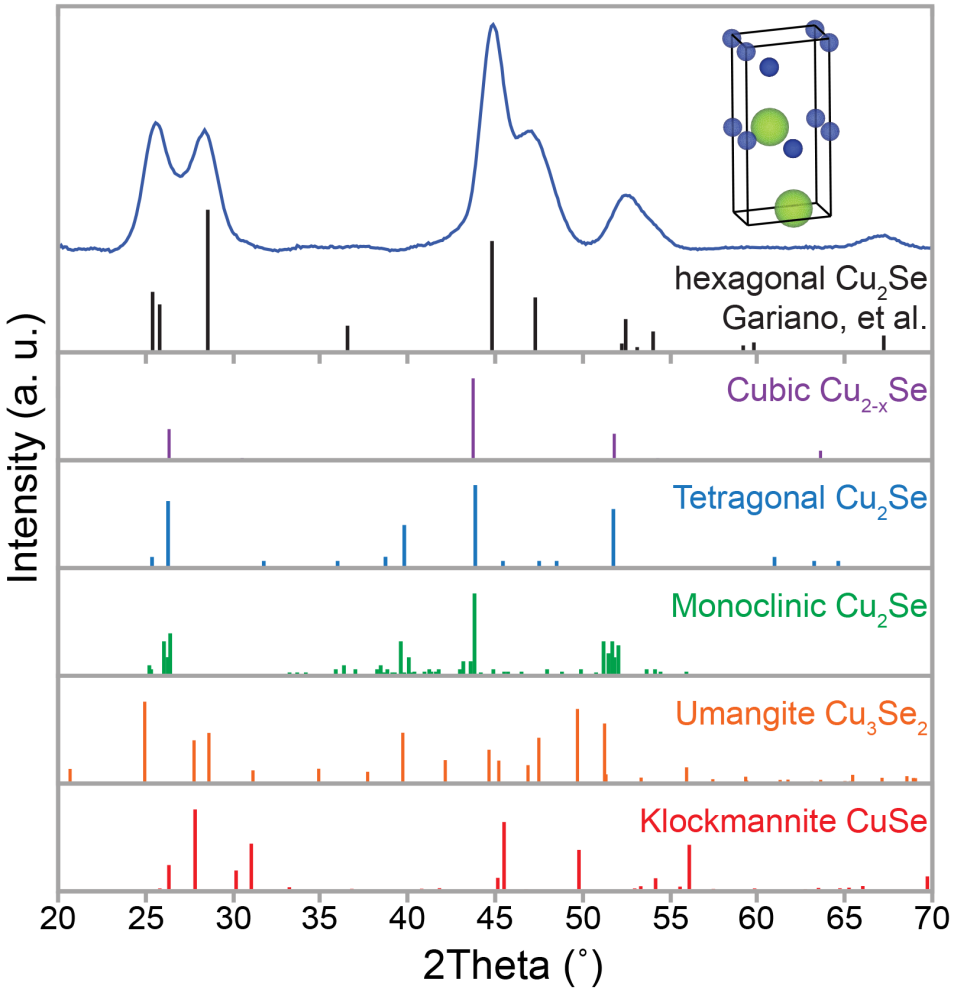

Figure 3.1. Powder XRD of the wurtzite $Cu_{2-x}Se$ nanocrystals (top), with unit cell and the reference pattern obtained from Gariano, et al., cubic (ICSD: 181661), tetragonal (JCPDS: 29-0575), monoclinic (JCPDS: 27-1131), umangite (ICSD: 16949) and klockmannite (ICSD: 82331) phases of copper selenide. Reprinted with permission from Hernández-Pagán, E. A., et al. *Chem. Mater.* **2019**, *31* (12), 4619. Copyright 2019 American Chemical Society.

nanocrystals. The diffraction peaks match that of the calculated pattern reported by Gariano et al. that corresponds to metastable wurtzite $Cu_{2-x}Se$ (space group $P6_3mc$),[106] not those of cubic $Cu_{2-x}Se$, tetragonal and monoclinic Cu_2Se, tetragonal umangite (Cu_3Se_2) and hexagonal klockmannite (CuSe). Moreover, quantitative energy-dispersive X-ray spectroscopy (EDS) provided a composition close to Cu_2Se (Table 3.1). Transmission Electron Microscopy (TEM) analysis revealed the $Cu_{2-x}Se$ nanocrystals have a disk morphology (Figure 3.2) with an average diameter of 13.8 ± 1.0 nm. (n=150) and thickness

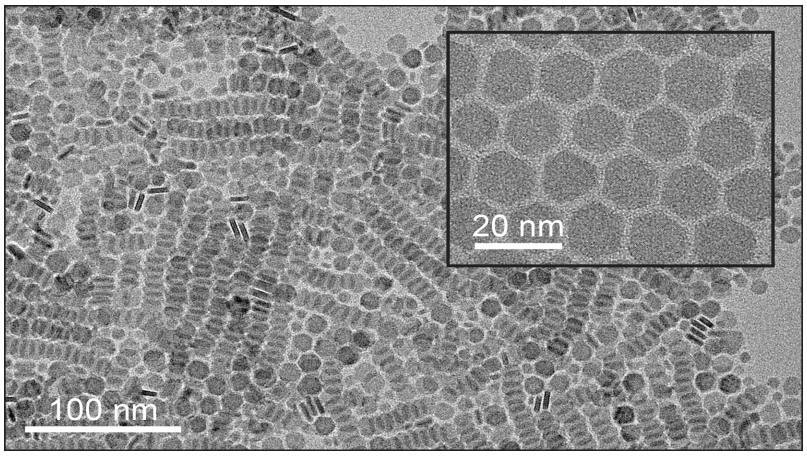

Figure 3.2. TEM image of disk-shaped $Cu_{2-x}Se$ nanocrystals aligned in rows. Inset: hexagonal morphology highlighted with close-packed NCs. Reprinted with permission from Hernández-Pagán, E. A., et al. *Chem. Mater.* **2019**, *31* (12), 4619. Copyright 2019 American Chemical Society.

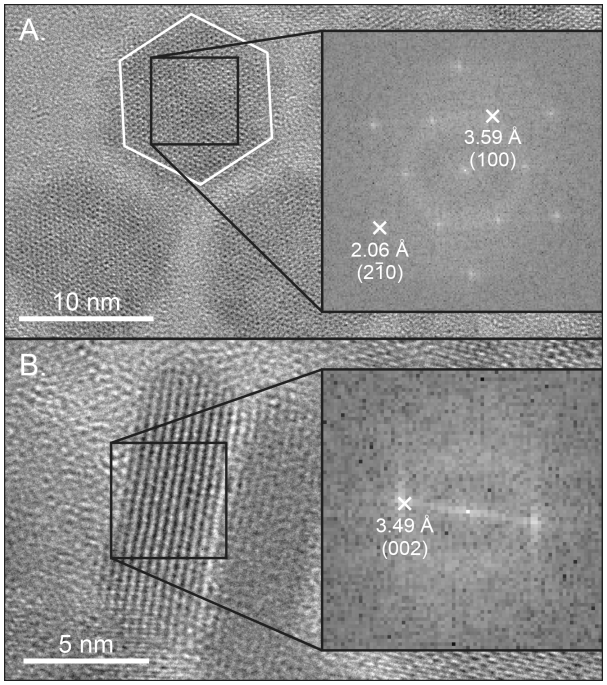

Figure 3.3. HR-TEM of NCs with inset FFT characterizing anisotropic hexagonal crystal structure. A. View down the $Cu_{2-x}Se$ c-axis reveals the hexagonal atomic arrangement. B. Viewed perpendicular to <002>. Reprinted with permission from Hernández-Pagán, E. A., et al. *Chem. Mater.* **2019**, *31* (12), 4619. Copyright 2019 American Chemical Society.

of 3.7 ± 0.2 nm (n=65). Further examination with high-resolution TEM (HR-TEM) and fast Fourier transform (FFT) of the images (Figures 3.3A-B) reveal an anisotropic crystal structure with the hexagonally close-packed layers stacked along the c-axis. The selected area electron diffraction (SAED) in Figure 3.4 is consistent with the XRD data (though

variation from the reference pattern can be attributed to the experimental differences between the TEM and XRD).

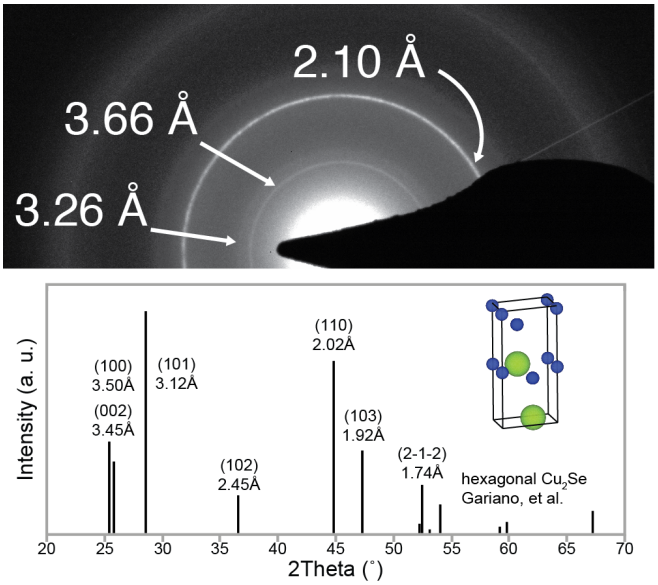

Figure 3.4. SAED of nanocrystals with Gariano, et al. reference pattern. SAED detects the (100)/(002) peak in the innermost ring (3.66Å), the (101) peak at 3.26Å, and the (110) peak at 2.10Å. Reprinted with permission from Hernández-Pagán, E. A., et al. *Chem. Mater.* **2019**, *31* (12), 4619. Copyright 2019 American Chemical Society.

Based on the bulk Cu-Se phase diagram, berzelianite (cubic) $Cu_{2-x}Se$ ($0 < x \leq 0.2$) is the thermodynamic phase in the copper-rich region at temperatures below 1000 K.[157] Although the effects of surface energy and ligands in nanoscale materials can alter the phase diagram, it has been shown that synthesized monoclinic and tetragonal Cu_2Se nanocrystals transform to berzelianite $Cu_{2-x}Se$ upon exposure to air.[141,143] In those systems, oxidation of copper and conversion to the thermodynamic substoichiometric $Cu_{2-x}Se$ phase are closely related and occur in concert. Copper migration from the NC core to the surface accounts for the stoichiometric "loss" of oxidized Cu in the cubic phase (however, the precise location of Cu^{2+} may not be known, and could remain in the core after oxidation[158]). This oxidation results in an increase of charge carrier density giving rise to a plasmon band in the NIR region.[141,143,158] The synthesized nanocrystals were purified under ambient conditions, thus one could expect to see this plasmon band.

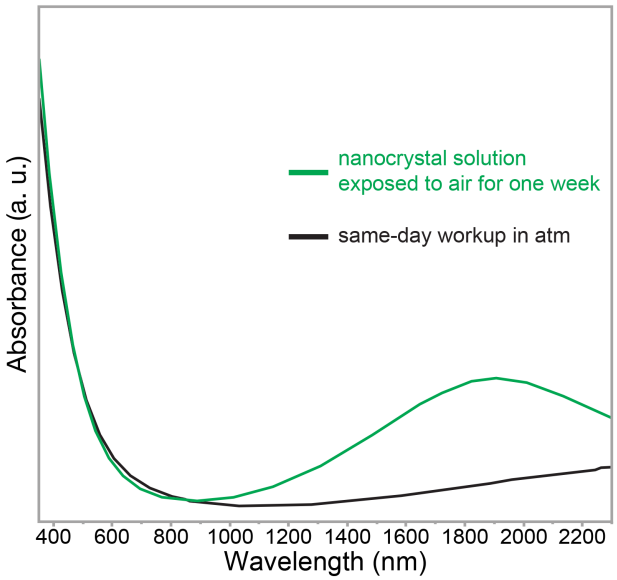

Figure 3.5. UV-vis-NIR spectra of wurtzite $Cu_{2-x}Se$ nanocrystals after the work up and after one week of storage, both under ambient conditions. Reprinted with permission from Hernández-Pagán, E. A., et al. *Chem. Mater.* **2019**, *31* (12), 4619. Copyright 2019 American Chemical Society.

Optical characterization was performed by UV-Vis-NIR spectroscopy in solution. The absorbance spectrum is shown in Figure 3.5. Interestingly, the absorbance spectrum does not exhibit a significant plasmon band in the NIR region. One week of exposure to ambient conditions was required for a broad plasmon band centered at 1900 nm to develop. This is in contrast to observations by Dorfs et al. where cubic $Cu_{1.96}Se$ nanocrystals exhibited a plasmon band at ~ 1600 nm after one minute under ambient conditions.[159] Similarly, Kriegel et al. observed the emergence of an intense plasmon band in the spectral region *ca* 1300-1400 nm as tetragonal Cu_2Se nanocrystals oxidized to cubic $Cu_{1.8}Se$ within 5.5 hrs.[143] The red shifted plasmon band observed here suggests a composition close to stoichiometry Cu_2Se, in agreement with the EDS results (Table 3.1). Furthermore, the relatively slow formation of a NIR surface plasmon and its position indicate that our synthetic conditions and ligand environment yield nanocrystals that are only weakly susceptible to oxidation. It should be noted the wurtzite $Cu_{2-x}Se$ NCs remained in the

hexagonal crystal structure and with similar morphology after weeks of air exposure (Figures 3.6 and 3.7).

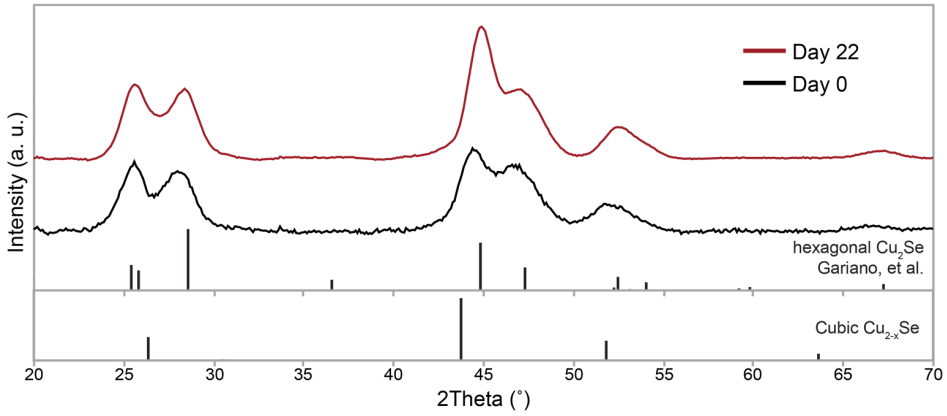

Figure 3.6. Powder XRD pattern of $Cu_{2-x}Se$ NCs acquired after synthesis, and a follow-up scan three weeks later. Cubic reference pattern ICSD: 181661. Reprinted with permission from Hernández-Pagán, E. A., et al. *Chem. Mater.* **2019**, *31* (12), 4619. Copyright 2019 American Chemical Society.

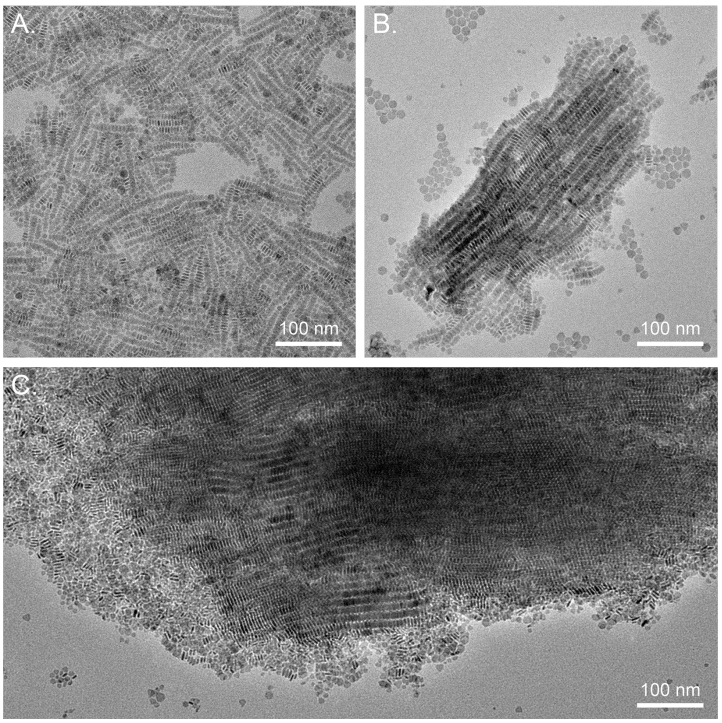

Figure 3.7. TEM images of wurtzite $Cu_{2-x}Se$ NCs. A and B. TEM images acquired two days after synthesis, Fig. A highlights the chains of monodisperse disks and B shows a lattice of chains. C. TEM image acquired two weeks after synthesis with NCs stored in chloroform in ambient conditions. The striated pattern seen in Fig. C is indicative of monodisperse nanocrystals arranged in a superlattice. Reprinted with permission from Hernández-Pagán, E. A., et al. *Chem. Mater.* **2019**, *31* (12), 4619. Copyright 2019 American Chemical Society.

In light of the prolonged stability of the hexagonal phase of the nanocrystals, variable temperature XRD was employed to force a phase transition at elevated temperatures. Data in Fig. 3.8A shows XRD patterns collected from 37 ˚C to 186 ˚C with some key features. Diagnostic of the phase change, the reflection corresponding to the (111) plane of berzelianite $Cu_{2-x}Se$ emerges as the temperature increases at the expense of

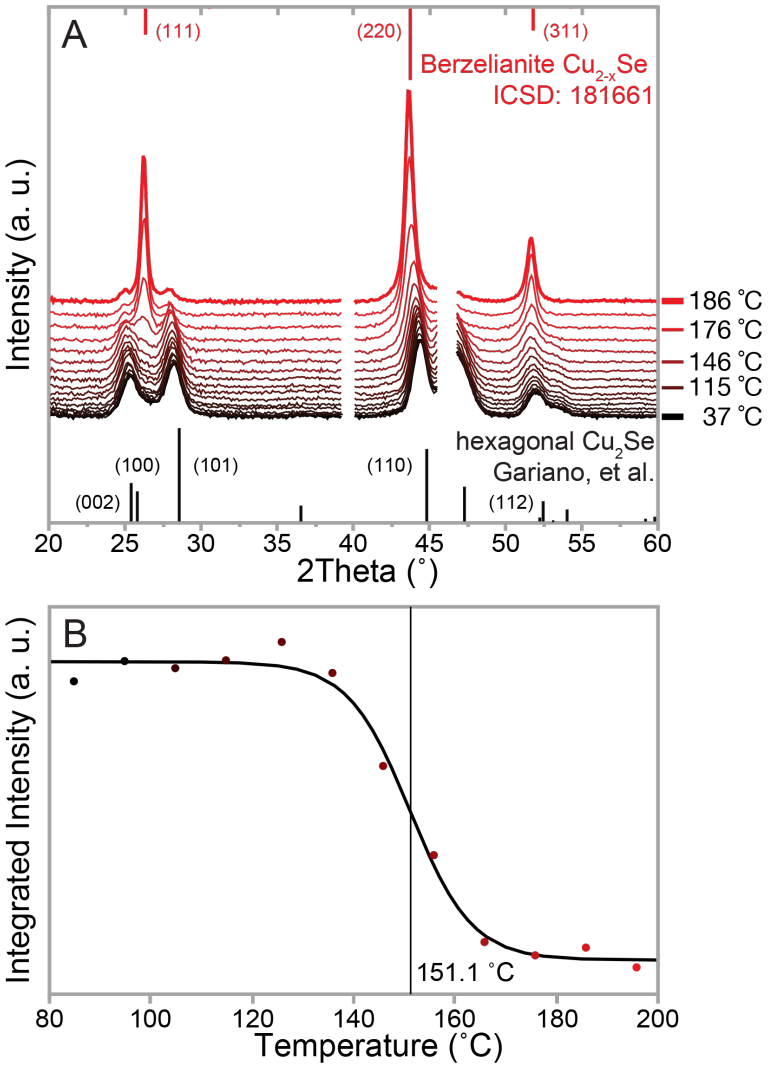

Figure 3.8. A. Variable temperature powder XRD of wurtzite $Cu_{2-x}Se$ nanocrystals along with the reference patterns for wurtzite and berzelianite $Cu_{2-x}Se$. Platinum reflections at 39.8˚ and 46.2˚ due to the sample holder have been omitted. B. The wurzite 25.2˚ reflections were integrated and plotted versus temperature to calculate the phase transition temperature of 151 ˚C per Rivest et al. Reprinted with permission from Hernández-Pagán, E. A., *et al.* Chem. Mater. **2019**, 31 (12), 4619. Copyright 2019 American Chemical Society.

the (002), (100) and (101) reflections of the wurtzite structure. Following the work of Rivest et al.,[160] the phase transition temperature was calculated by fitting a Boltzmann function to the integrated intensity of the diminishing wurtzite peak at 25.2˚. As depicted in Figure 3.8B, the transition temperature from the wurtzite to berzelianite crystal structure was found to be approximately 151 ˚C. To verify the transition temperature, the synthesized nanocrystals were cleaned and subsequently heated in octadecene at 150 ˚C for 1 hr; as was expected the nanocrystals transformed into the berzelianite (cubic) phase (Figure 3.9). We

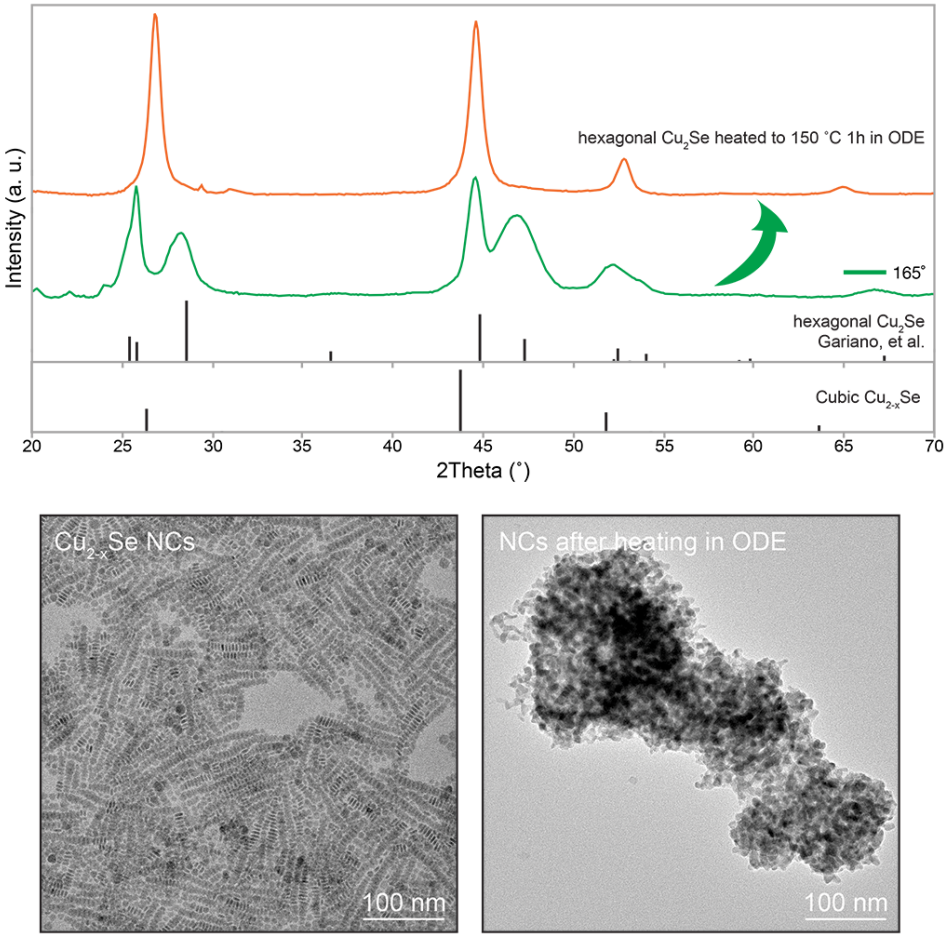

Figure 3.9. (Top) Powder XRD pattern of $Cu_{2-x}Se$ particles that were synthesized at 165 ˚C, and then cleaned following the outlined experimental procedure. The particles were then heated in ODE to **150 ˚C** for 1 hour, cleaned, and analyzed by XRD. XRD revealed the NCs had converted to the cubic crystal phase. Cubic reference pattern ICSD: 181661 (Bottom) TEM images of the NCs before and after heating in ODE showing that the particles had aggregated. Reprinted with permission from Hernández-Pagán, E. A., et al. *Chem. Mater.* **2019**, *31* (12), 4619. Copyright 2019 American Chemical Society.

found that the product NCs from this experiment were aggregated and sintered together, a process that has been shown to facilitate phase transition in other NC crystal structure systems.[161] In a follow-up experiment, a standard synthesis was extended from 1h to 4h at 155 ˚C, and the resulting phase was surprisingly still wurtzite $Cu_{2-x}Se$. TEM in Figure 3.10

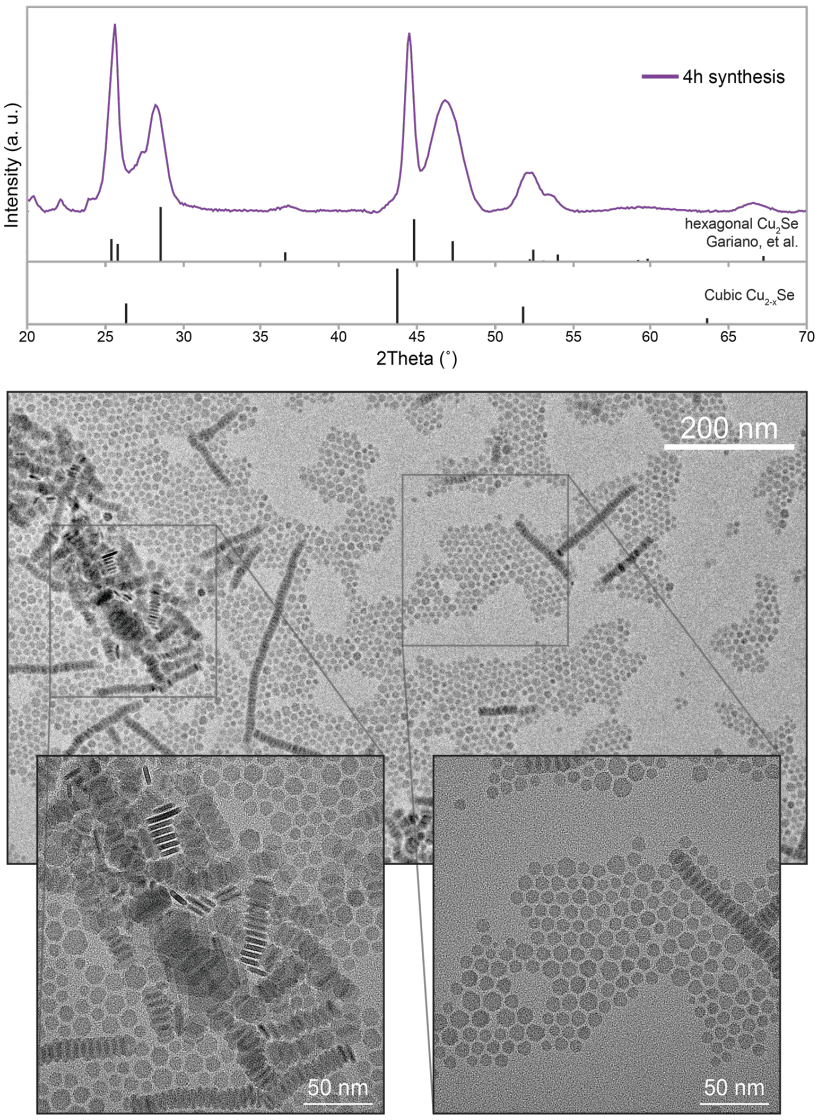

Figure 3.10. (Top) XRD pattern of $Cu_{2-x}Se$ NCs synthesized under typical reaction conditions (see Experimental Section) and left to react for 4h. Cubic reference pattern ICSD: 181661. (Bottom) TEM images of $Cu_{2-x}Se$ NCs reacted for 4h. The extended reaction time leads to larger, more polydisperse particles. The average length and width of particles measured on their sides were 18 ± 5 nm and 3.7 ± 0.3 nm (n = 80), respectively. In comparison to the standard 1h reaction time the thicknesses are statistically similar, however NC length is larger on average with more variation (see left inset with larger platelets). Reprinted with permission from Hernández-Pagán, E. A., et al. *Chem. Mater.* **2019**, *31* (12), 4619. Copyright 2019 American Chemical Society.

showed that the particle size distribution was polydisperse relative to the 1h standard synthesis, but the nanocrystals were isolated from one another due to the stability provided by the ligand corona. The fact that the phase-change temperatures in the variable-temperature XRD experiment and the experiment involving heating NCs in ODE were lower than the NC synthesis temperatures may be due to the lack of additional stabilizing surface chemistry.

The transition temperature being close to the synthesis temperature and the susceptibility to sintering-induced phase change highlight the advantages of reagents and coordinating solvents active at moderate temperatures. Reaction aliquots taken below 155°C showed no evidence of nanocrystal formation, yet a distinct color change from blue to brown was observed at 155°C as nanocrystals formed. Control syntheses performed at 165 ˚C and 175 ˚C yielded predominantly wurtzite nanocrystals but with phase impurities (Figure 3.11). At 185 ˚C, berzelianite $Cu_{2-x}Se$ nanocrystals were obtained. It appears the

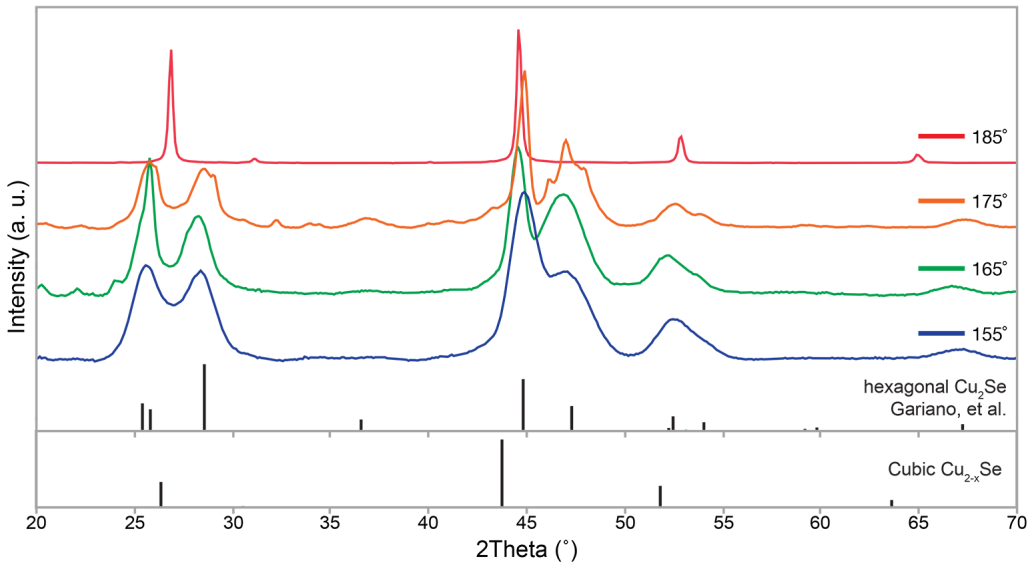

Figure 3.11. XRD patterns for $Cu_{2-x}Se$ NCs synthesized at 155 ˚C, 165 ˚C, 175 ˚C and 185 ˚C. Unidentified impurities become prevalent at higher temperatures though the wurtzite $Cu_{2-x}Se$ dominates the XRD pattern, however at 185 ˚C the product is cubic. Cubic reference pattern ICSD: 181661. Reprinted with permission from Hernández-Pagán, E. A., et al. *Chem. Mater.* **2019**, *31* (12), 4619. Copyright 2019 American Chemical Society.

reactivity of DD_2Se_2 is at a bare minimum to achieve the phase purity of the metastable phase observed. A reagent any less reactive and requiring higher reaction temperatures or longer times would have resulted in significant impurities of the thermodynamic cubic phase.

To test if the lower reaction temperature was the only factor responsible for the formation of the wurtzite phase, DD_2Se_2 was replaced with dodecyl selenol (DDSeH). When DDSeH was used under otherwise identical conditions, the reaction yields the thermodynamic product, berzelianite $Cu_{2-x}Se$ (Figure 3.12) instead of the wurtzite product.

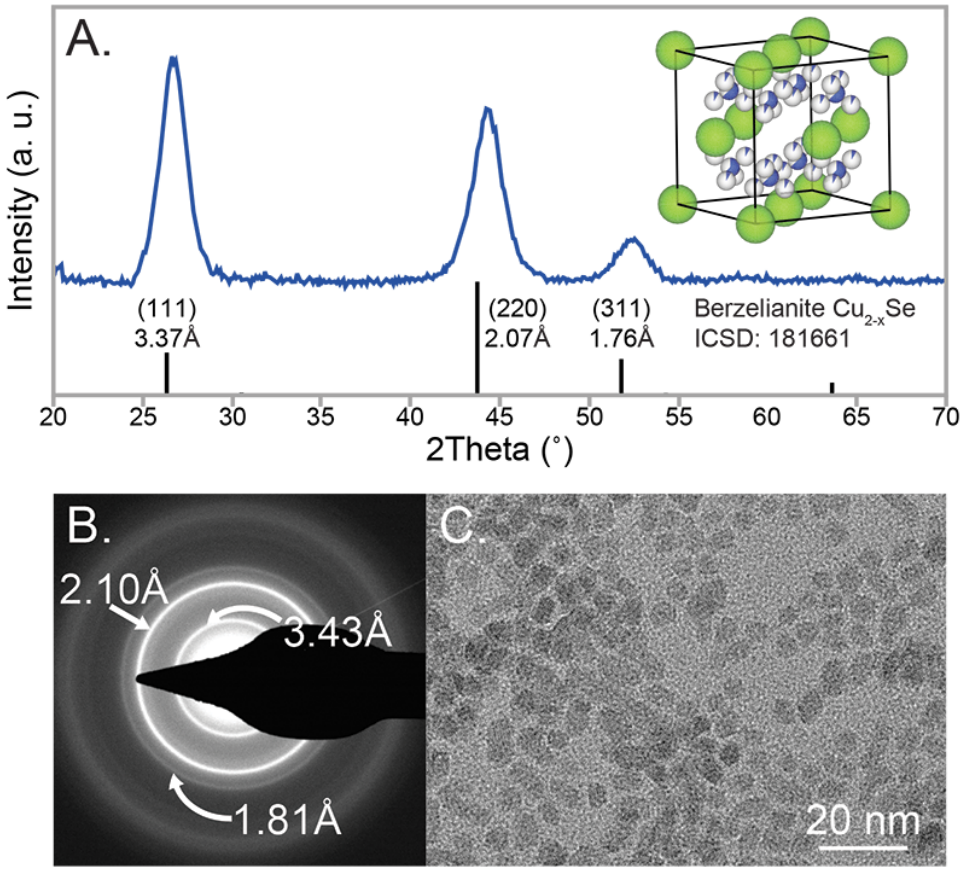

Figure 3.12. Cubic $Cu_{2-x}Se$ synthesized when dodecaneselenol is used as the selenium precursor.[127] A. Powder XRD of cubic NC sample with Berzelianite $Cu_{2-x}Se$ reference (ICSD: 181661). B. SAED with rings corresponding to cubic $Cu_{2-x}Se$. C. TEM image of cubic $Cu_{2-x}Se$ NCs, avg. diameter 5.6 ± 1.2 nm (N=115). Reprinted with permission from Hernández-Pagán, E. A., et al. *Chem. Mater.* **2019**, *31* (12), 4619. Copyright 2019 American Chemical Society.

Previous literature reports have shown control of the product phase when using dialkyl dichalcogenides with different substituents and with dialkyl dichalcogenides vs alkyl thiol/selenol.[139,152] The phase control has been attributed in part to the relative strength of the C-X and X-X (X=Se, S) bonds, and consequently the chalcogenide transfer rate. More easily cleaved bonds in the organochalcogenide lead to the thermodynamic products. For example, in the synthesis of $CuInSe_2$, Tappan et al.[153] were able to selectively obtain the thermodynamic chalcopyrite or the metastable wurtzite $CuInSe_2$ product employing dibenzyl diselenide (C-Se 43 kcal/mol) or diphenyl diselenide (C-Se 65 kcal/mol), respectively, as the Se source. Similarly, the copper selenide intermediates of these reactions showed a similar trend. The reaction progressed through the thermodynamically stable intermediates of berzelianite $Cu_{2-x}Se$ and klockmannite CuSe when dibenzyl or dimethyl diselenide (weaker C-Se bonds) were employed. Conversely, reactions involving diphenyl diselenide (stronger C-Se bonds) progressed via the metastable intermediate umangite Cu_3Se_2.

DFT calculations (Figure 3.13) revealed C-Se bond strengths of 55.4 kcal/mol and 67.8 kcal/mol for DD_2Se_2 and DDSeH, respectively, following the same trend as previously reported for other organochalcogenides. Given the above hypothesis, one would expect the DD_2Se_2 to give the thermodynamic phase and DDSeH to give the metastable phase, yet the results here are the opposite. Therefore, other factors are at play.

To shed some light on the mechanistic details that lead to phase control, aliquots of the reactions taken at 80 °C, 120 °C, 0 min@155 °C, and 5 min@155 °C were analyzed with XRD. Figure 3.14A shows the patterns for the syntheses with DDSeH. The XRD

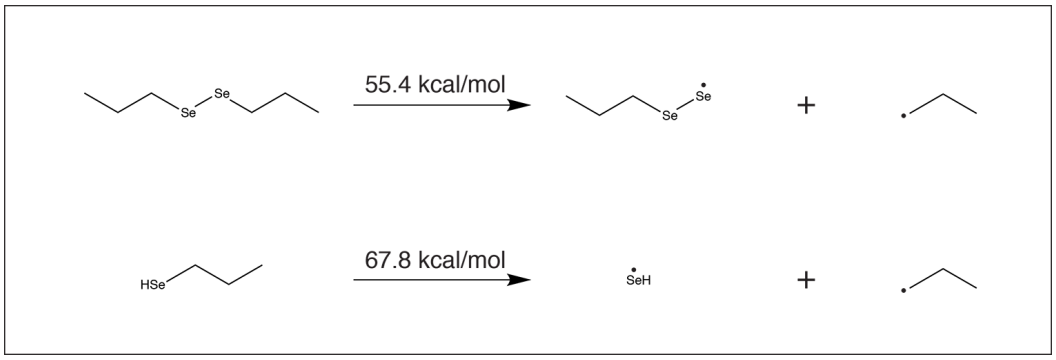

Figure 3.13. DFT calculations of C-Se bond dissociation energies for DD_2Se_2 and DDSeH. Reprinted with permission from Hernández-Pagán, E. A., et al. *Chem. Mater.* **2019**, *31* (12), 4619. Copyright 2019 American Chemical Society.

pattern for the 80 °C aliquot reveals the formation of a Cu-selenoate complex ($CH_3(CH_2)_{10}CH_2Se$-Cu). This complex was also observed in the work of Bryks et al.[155] and Berends et al.[154] This Cu-selenoate complex is a lamellar mesophase analogous to the well documented metal-thiolate complexes, which have been exploited in the synthesis of metal and metal sulfide nanocrystals.[162–164] The reflections corresponding to the complex remained present at 120 °C, yet subsided significantly when the system reached the reaction temperature (0 min@155 °C). After 5 min at 155 °C, the complex was no longer present, indicative of the nucleation onset of $Cu_{2-x}Se$. In contrast, for DD_2Se_2 (Figure 3.14B), the XRD patterns of the four corresponding aliquots early in the reaction sequence

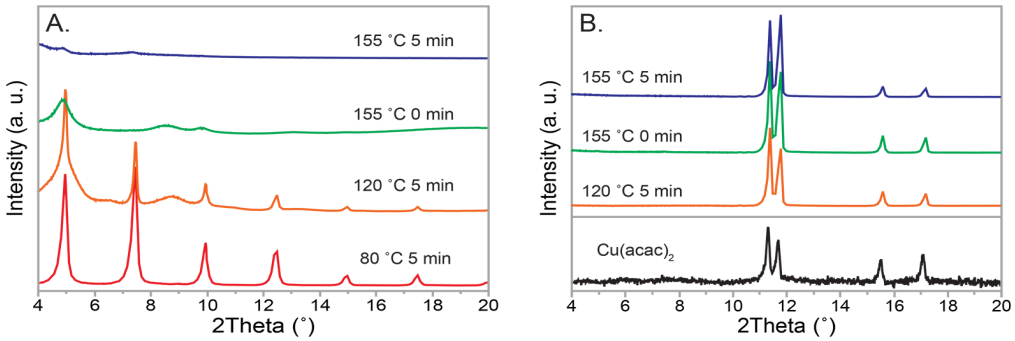

Figure 3.14. Aliquot XRD study of the precursor formation during $Cu_{2-x}Se$ syntheses. A. When dodecaneselenol is used in a NC synthesis, the selenol reacts with Cu early on in the heat-up to reaction temperature of 155 °C, generating a lamellar mesophase similar to that observed by Bryks, et al. results with Cu_2S. B. Didodecane diselenide shows less reactivity during the heat-up and only $Cu(acac)_2$ is detected with XRD. Reprinted with permission from Hernández-Pagán, E. A., et al. *Chem. Mater.* **2019**, *31* (12), 4619. Copyright 2019 American Chemical Society.

matched the reflections for $Cu(acac)_2$. The presence of the diselenide bond prevents formation of the Cu-selenoate complex as presumably a homolytic cleavage of the Se-Se bond would be required as opposed to a simple ligand exchange.

In the context of the previous observations of others of phase control based on bond strength of the precursors, we posit that the formation of the complex results in Cu withdrawing electron density from Se, weakening the C-Se bond for the DDSeH. Since the copper-thiolate complex does not readily form as an intermediate for DD_2Se_2, this reagent is the less reactive of the two. Thus, in agreement with the previous observations in the literature, the more-reactive precursor leads to the thermodynamically favored cubic phase under synthetic conditions.

It is known that ligands can direct the phase of the products in other metal-chalcogenide systems,[103,138,139] and the copper selenide system is similarly susceptible. As mentioned earlier, a Cu-selenoate complex was observed to form in the work by Bryks et al.[155] and Berends et al.,[154] however these two reactions yielded different products. The solventless thermolysis of a Cu-selenoate complex performed by Bryks et al. formed the thermodynamic product, berzelianite $Cu_{2-x}Se$. This system is similar to ours, but without the non-coordinating solvent octadecene present in our reaction, which facilitates the diffusion of reactants. In contrast, the reaction system employed by Berends et al. contained additional ligands (e.g. trioctylphosphine oxide, oleylamine) and lead to nanocrystals of umangite Cu_3Se_2. Similarly, Tappan et al. observed umangite Cu_3Se_2 *en route* to wurtzite $CuInSe_2$ in the presence of oleic acid and oleylamine. Care must therefore be taken when comparing results with differing ligands present. The reaction system in the present work was intentionally simplified by utilizing a non-coordinating solvent, and DD_2Se_2 or

DDSeH as both the selenium source and ligands. Ligands may play unrecognized roles in the decomposition mechanism of the organochalcogenide reactants. Our lab has shown, for example, that oleylamine plays a key role in the decomposition of allyl disulfide.[139]

Similarly, the Hogarth group recognized amines were changing the reactive organometallic intermediate decomposition mechanism of nickel dithiocarbamates, influencing the phase of the resultant nickel sulfide.[165] Ligands may also alter the surface energies of the growing nuclei,[103] and our group has previously shown that thiol sulfur precursors can provide highly bridged surface chemistries of the thiol ligands.[62,166] Further work in the corresponding organoselenide chemistry is in progress.

3.4 Conclusion

In summation, a direct synthesis for the recently discovered copper(I) selenide wurtzite phase was developed using didodecyl diselenide as a nanocrystal selenium source and ligand. XRD confirmed the hexagonal phase initially discovered by Gariano, et al., and TEM revealed a platelet-like morphology. A high-temperature study showed that the metastable wurtzite phase converted to the thermodynamic berzelianite phase at approximately 151 ˚C. DDSeH alternatively provided the cubic Cu_2Se product, through a copper selenoate intermediate with a hypothesized weaker C-Se bond than DD_2Se_2. The synthesis of other metal selenides with DD_2Se_2 and DDSeH as ligands/selenium source is currently in progress, as well as an investigation into how the additional ligands (e.g. TOP) alter the resulting phase as previously observed by others.

3.5 Experimental Methods

Materials. Selenium powder (≥99.5 trace metals basis), 1-bromododecane (97%), formic acid (≥95% reagent grade), anhydrous N,N-dimethylformamide (DMF, 99.8%), tetrahydrofuran (THF, ≥99.9%), and 1-octadecene (ODE, 90% technical grade) were obtained from Sigma Aldrich. Sodium borohydride and hydrochloric acid (ACS Plus) were obtained from Fisher Chemicals. $Cu(acac)_2$ (≥98%) was obtained from Strem Chemicals. All materials were used as received without additional purification.

Synthesis of Didodecyl Diselenide. $C_{24}H_{50}Se_2$ was synthesized following a previously reported procedure.[167] A 1L three-neck round bottom flask was flushed with argon and maintained under inert atmosphere throughout. 75 mL of deionized H_2O was added, followed by 9.3 g (0.12 mol) of selenium powder. The reaction was stirred and cooled on an ice bath for 10 min. 9.8 g (0.26 mol) of $NaBH_4$ was added portion-wise so that the evolution of hydrogen gas did not cause a rapid increase in temperature. The reaction was then allowed to stir for 20 min. Another 9.3 g (0.12 mol) of selenium powder was added and the reaction was allowed to cool to room temperature followed by an additional 20 min. of stirring at room temperature. The flask was then heated to 70 °C and temperature maintained for 20 min. resulting in a clear dark red solution. The reaction was allowed to cool to room temperature. 1-bromododecane (58.6 g, 0.24 mol) and 280 mL of tetrahydrofuran were added dropwise over 30 min. under vigorous stirring. The reaction was then allowed to react at 50 °C for 18 hours, and then it was cooled to room temperature. The phases were separated. The organic layer was washed once with deionized H_2O, then combined organic layers were washed with brine and dried over $MgSO_4$. The solvent was

removed under reduced pressure. The crude product was recrystallized from heptane and isopropyl alcohol over an ice bath to yield yellow needles. Yield: 53.5%.

^{1}H NMR (400MHz, $CDCl_3$) δ 2.92 (t, 4H, J=7.6 Hz), 1.73 (quint, 4H, J=7.5 Hz), 1.27 (m, 36H), 0.88 (t, 3H, J=7.1 Hz).^{13}C NMR (100 MHz, $CDCl_3$) δ 31.86, 30.93, 30.20, 29.61, 29.58, 29.55, 29.47, 29.30, 29.10, 22.63, 14.04. ^{77}Se NMR (76 MHz, $CDCl_3$) δ 307.7.

Synthesis of Dodecyl Selenol. $C_{12}H_{25}SeH$ was synthesized following a previously reported procedure.[167] A 250 mL three-neck round bottom flask was flushed with argon and maintained under inert atmosphere throughout. To the flask was added selenium powder (4.6 g, 0.06 mol) and sodium borohydride powder (4.5 g, 0.12 mol). Anhydrous ethanol (21 mL) as added slowly to the solution. With 20 min. of stirring, a white/grey solid gradually formed. Anhydrous DMF (100 mL) was slowly added. The reaction turned a rufous color, then gradually turned clear and colorless over 30 min. Formic acid (4.6 mL, 0.125 mol) was then added dropwise and the reaction was allowed to stir for 20 min. 1-bromododecane (12 mL, 0.05 mol) was added slowly to the mixture and the reaction was allowed to stir for 4-6 hours, dependent on completion of reaction as verified by quenched aliquots with TLC. (Note: failure to allow reaction to run to completion results in a mixture of dodecyl selenol and dodecyl bromide, which forms an azeotrope during distillation and is otherwise challenging to separate by other common purification methods). The reaction was then hydrolyzed with 100 mL of 10% HCl. 50 mL of H_2O was added to the mixture, and the organic layer was extracted 3x with 50ml of Et_2O. The combined organics were washed once with 10% HCl and dried over $MgSO_4$. The solvent was removed under reduced pressure. Vacuum distillation produced pure dodecyl selenol. ^{1}H NMR (400MHz,

$CDCl_3$) δ 2.58 (q, 2H, J=7 Hz), 1.69 (quint, 2H, J=7.5 Hz), 1.26 (m, 18H), 0.88 (t, 3H, J=7.0 Hz), -0.70 (t, 1H, J=6.8 Hz). ^{13}C NMR (100 MHz, $CDCl_3$) δ 33.95, 31.85, 29.58, 29.57, 29.54, 29.49, 29.45, 29.28, 28.92, 22.62, 17.63, 14.04. ^{77}Se NMR (76 MHz, $CDCl_3$) δ -13.1.

Synthesis of hexagonal $Cu_{2-x}Se$ NCs. Standard Schlenk line techniques were used throughout with N_2 as the inert gas. In a typical synthesis, 1.1 mmol of didodecyl diselenide, 0.5 mmol of $Cu(acac)_2$, and 5 mL of octadecene were mixed in a 25 mL 3-necked flask. The flask was put under vacuum and the temperature was raised to 80 ˚C for 30 min. Then the flask was put under inert atmosphere and the temperature was raised to 155 ˚C for 1 hour. The flask was allowed to cool to room temperature, and the post-reaction mixture was precipitated in acetone three times and resuspended in chloroform.

Synthesis of cubic $Cu_{2-x}Se$ NCs. The same procedure as described for the hexagonal $Cu_{2-x}Se$ NCs was followed except a stoichiometric amount of dodecyl selenol was used in place of didodecyl diselenide.

Instrumentation. Transmission Electron Microscopy (TEM) was performed on a FEI Technai Osiris digital 200 kV S/TEM system. Solution absorption spectra were obtained on a Jasco V-670 UV-Vis-NIR spectrophotometer in tetrachloroethylene. X-ray diffraction (XRD) measurements were done using a Rigaku SmartLab powder X-ray diffractometer with a CuKα (λ = 0.154 nm) radiation source set to 40 kV and 44 mA, and a D/teX Ultra 250 1D silicon strip detector. XRD patterns were acquired using a step size of 0.1 degrees

at 1 or 10 degrees per minute. High temperature XRD measurements were performed using a Rigaku Multipurpose High Temperature Attachment and a PTC-EVO temperature controller, with a ramp rate of 2 degrees per minute and a holding time of 2 min. The furnace temperature was measured using an R type thermocouple with an accuracy of ± 1.5 ˚C. ^{1}H NMR spectra were taken using a Bruker DRX-400 (tuned to 400 MHz) spectrometer. Spectra were calibrated to residual solvent signals of 7.26 ppm in $CDCl_3$. ^{13}C and ^{77}Se NMR spectra were taken using a Bruker DRX-500 (tuned to 100 MHz or 76 MHz for ^{13}C or ^{77}Se, respectively) spectrometer. ^{13}C spectra were calibrated to residual solvent signals of 77.0 ppm in $CDCl_3$.

Computational Methods. The computational methods performed herein were adapted from the works of Guo et al.[156] and Rhodes et al.[139] Bond dissociation energies were calculated using Gaussian with density functional theory (DFT) and the Boese-Martin Kinetics (BMK) functional. Molecular geometry optimization was performed using the 6-31G(d) basis set and single-point energy calculations were performed using the 6-311G(d,p) basis set.

Chapter 4

PHASE AND MORPHOLOGICAL CONTROL INVESTIGATION OF COPPER(I) TELLURIDE USING A DITELLURIDE PRECURSOR

4.1 Abstract

In this chapter, the synthesis of $Cu_{2-x}Te$ nanocrystals of different phases and morphologies is discussed. Using didodecyl ditelluride and without the need for phosphine precursors, nanocubes, nanorods, and 2-D nanosheets were synthesized in the pseudo-cubic phase ($Cu_{1.5}Te$) and in Vulcanite (CuTe). Nanosheets of what appear to be the substoichiometric Vulcanite phase were synthesized which do not have a precedent in the literature. Materials discussed in this chapter were characterized with TEM, powder XRD and UV-Vis-NIR absorbance spectroscopy.

4.2 Introduction

Copper(I) telluride nanocrystals are an emerging member of the copper chalcogenide nanomaterial family and, like the corresponding sulfides and selenides, copper telluride has an advantageous capacity for facile cation exchange to obtain other novel metal telluride nanomaterials.[168,169] Additionally, copper telluride is a direct bandgap semiconductor (1.1-1.5 eV) and the copper vacancies in substoichiometric $Cu_{2-x}Te$ phases give the material plasmonic properties.[170,171] While not as prevalent in the literature as its sulfide counterpart, copper telluride has generated recent interest for its optical,[168,172] photothermal,[170,173,174] thermoelectric,[175,176] photocatalytic,[177] and electrochemical properties.[178] The Cu-Te phase diagram is noted for being extremely complex (seven

known compounds, most of which are polymorphic),[179,180] with little known about many of the different phases.

Early literature examples of copper telluride nanoscale materials dating to the first decade of the 2000s were made using microwave-based syntheses,[181,182] and hydrothermal methods,[183,184] which primarily resulted in crystalline aggregates. In 2013, Li, et al. published a solvothermal synthesis for colloidal $Cu_{2-x}Te$ nanocrystals and achieved some control over morphology using lithium bis(trimethylsilyl) amide as a precursor activating agent.[170] The authors were able to synthesize cubes, platelets and nanorods of an (at that time) unidentified metastable $Cu_{2-x}Te$ phase that was not known in bulk materials. This particular pseudo-cubic phase was synthesized in a number of instances in the literature,[170,173] but not definitively characterized until aberration-corrected TEM analysis was performed by both Willhammar, et al.,[172] and later Mugnaioli, et al.[185] Mugnaioli, et al. found that the orthorhombic unit cell (a = 7.5(1) Å, b = 22.8(2) Å, c = 29.6(3) Å) consisted of 96 Te atoms arranged in a pseudo-cubic lattice with 124 Cu atoms tetrahedrally coordinated by Te. Tu, et al. found that $Cu_{2-x}Te$ nanocrystals of this new phase were an effective parent material for cation exchange with Pb^{2+}, Sn^{2+}, Cd^{2+} and Hg^{2+}.[169] The authors found that the product materials' final crystal structure determined the type of heterostructure intermediates that would form; core-shells of $Cu_{2-x}Te$@PbTe and $Cu_{2-x}Te$@SnTe (tetrahedrally-coordinated cations), and Janus-like nanocrystals of $Cu_{2-x}Te$/CdTe and $Cu_{2-x}Te$/HgTe (octahedrally-coordinated cations). Interestingly, the hexagonal phase of the HgTe nanocrystals synthesized through cation exchange had not been seen in the bulk before.

In the work presented in Chapter 3 of this text, a diselenide precursor was used to directly synthesize a unique phase of $Cu_{2-x}Se$ that is not known in the bulk,[186] and had only been reported once previously.[106] This chapter discusses the application of a similar ditelluride precursor in the synthesis of $Cu_{2-x}Te$ nanocrystals. While attempts were made to synthesize a tellurol analogous to the selenol used in Chapter 3, the high degree of reactivity made processing the tellurol impractical. Syntheses with the ditelluride resulted in nanocrystals with known phases of CuTe and $Cu_{2-x}Te$, with interesting morphological characteristics. Fast-Fourier Transform (FFT) analysis of two-dimensional nanosheets of copper telluride appeared to reveal the phase Vulcanite (CuTe). To the author's knowledge, this represents the first solvothermal synthesis of this phase and morphology combination.

4.3 Results and Discussion

The ditelluride analogue to the diselenide used in Chapter 3 was synthesized following an adapted procedure from the literature[187] by collaborator Prof. Ahmed Nuriye (see Experimental Methods section). The didodecyl ditelluride (DD_2Te_2) was a solid at room temperature making handling relatively straightforward, similar to the diselenide precursor. It followed that a tellurol analogue to the selenol should be synthesized in order to compare the phase of the Te-containing nanocrystal products. However, unlike the selenol precursor's synthesis (dodecyl selenol), the tellurol proved to be much more difficult to process due to its predisposition to oxidation. Synthesis of the tellurol was attempted through three different routes, though none yielded an isolable product. Adapting the previously used selenol syntheses from Berends, et al.[154] (see Chapter 5) and Dilimon, et al.[167] (see Chapter 3) failed in both instances. Lastly, attempts were made to reduce the

ditelluride to a tellurol using $NaBH_4$ following the work of Uemura, et al.,[188] and the results seemed more promising than the previous attempts. However, after the reduction of the ditelluride, oxidation would begin within the reaction flask (as evidenced by the accumulation of yellow solids on the flask walls and a subsequent change in the reaction solution from colorless to red). The deleterious reactivity of tellurols in terms of handling is noted in the literature,[152,189] and the probability of removing reaction impurities post-synthesis or chemically-stable long-term storage seemed unlikely. It was decided to proceed with the ditelluride alone.

The first NC synthesis experiments were modeled on the work presented in Chapter 3 and probed the nucleation temperature of $Cu_{2-x}Te$ in octadecene using $Cu(acac)_2$ and DD_2Te_2. The nucleation temperature was found to be approximately 115 ˚C based on the presence of crystalline material in XRD samples, but the product was relatively large, as evidenced by the narrow peaks in XRD and a lack of colloidal stability.

Following this, the copper telluride nanocrystal syntheses used a coordinating solvent to mitigate NC size, like oleylamine (OlAm) and oleic acid (OA). Later, to prevent unwanted interactions between the ditelluride and the coordinating solvents, experiments were performed in a non-coordinating solvent (dioctyl ether) to control the dissociation of DD_2Te_2. A range of synthesis temperatures were explored from 115˚C to 180 ˚C, this was prompted by the fact that synthesis temperature had a marked effect on phase in the $Cu_{2-x}Se$ work of Chapter 3.[186]

When $Cu_{2-x}Te$ was synthesized in the presence of OlAm, cube-shaped NCs similar to the results of Li, et al.[170] were seen in the majority of samples (see Figure 4.1A), with other morphologies, such as rod-like nanocrystals and nanosheets, present after higher

temperatures and longer reaction times. Figure 4.1 depicts the products of a heat-up synthesis (A and B) and a hot-injection synthesis (C and D) of copper(I) telluride NCs performed in OlAm. In Figure 4.1A, colloidally stable cube-like NCs with edge lengths of

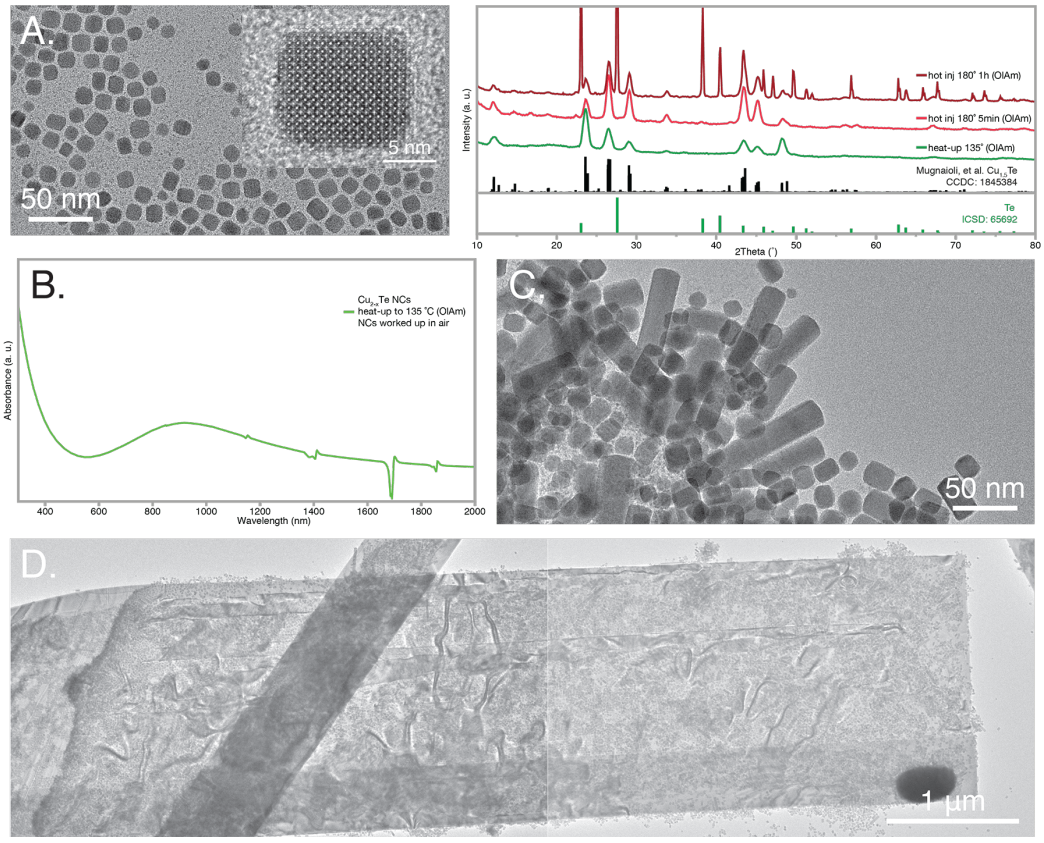

Figure 4.1. A. TEM image of $Cu_{1.5}Te$ cubes from a heat-up synthesis (30 min. at 135 ˚C) in OlAm with edge length 11.9 ± 1.8 nm (N=100), with corresponding XRD pattern (green trace) that is matched to the pseudo-cubic $Cu_{1.5}Te$ phase. Inset HRTEM image highlights the lattice fringing of this cube-like morphology. B. UV-Vis-NIR absorbance spectrum of the sample in A, with surface plasmon resonance centered at approximately 900 nm. C and D. Results of a hot-injection synthesis (1 hour at 180 ˚C) in OlAm that include a mixture of cube-like NCs and nanorods. The dimensions of this mix were an average length of 29 ± 21 nm and width of 16 ± 3 nm (N=100). XRD patterns for this hot-injection product were matched to the pseudo-cubic $Cu_{1.5}Te$ phase (CCDC: 1845384) and, after one hour at reaction temperature, a tellurium impurity is also present (ICSD: 65692). C is a composite image of an approximately 7.2 by 1.8 µm two-dimensional nanosheet of $Cu_{2-x}Te$ which covers a layer of NCs like those shown in B.

11.9 ± 1.8 nm (N=100) resulted from a heat-up synthesis to 135˚C for 30 minutes. The UV-Vis-NIR absorption spectrum in Figure 4.1B shows a localized surface plasmon resonance centered around approximately 900 nm, which was comparable to the spectrum obtained by Li, et al.[170]

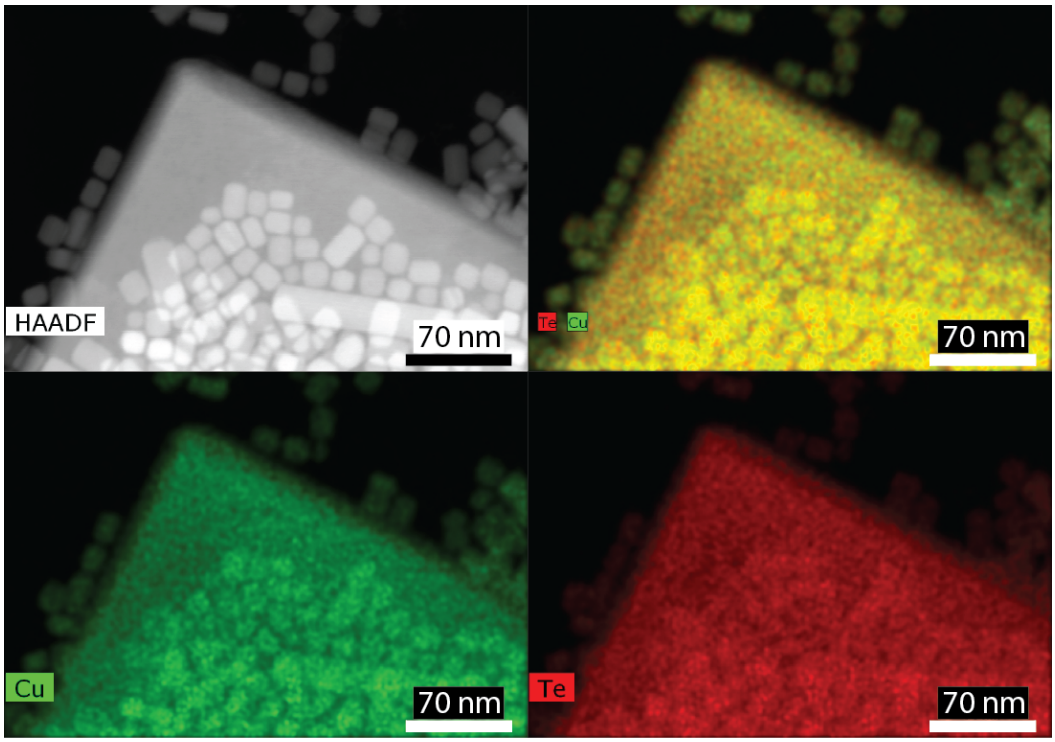

Figure 4.2. STEM EDS mapping of a nanosheet revealing the presence of copper and tellurium.

Cube-like nanocrystals also resulted after 5 minutes in a hot-injection synthesis performed at 180˚C. After an hour at temperature, nanosheets were also seen in addition to the cubes and nanorods (depicted in 4.1C and D). Nanosheets of copper telluride have at least two precedents in the literature with Nethravathi, et al. synthesizing nanosheets of hexagonal $Cu_{1.75}Te$,[175] and Mugnaioli, et al. synthesizing sheets with the pseudo-cubic $Cu_{1.5}Te$ phase.[185] Nanosheets were present in subsequent reactions and more in-depth analysis was performed to determine the phase of this product (vide infra).

Also shown in Figure 4.1, XRD characterization revealed that the dominant crystal structure present in 135 ˚C heat-up syntheses and 180 ˚C hot injection (5 min.) was the pseudo-cubic phase $Cu_{1.5}Te$, which was characterized in depth by Willhammar, et al.,[172] and Mugnaioli, et al.[185] XRD analysis shows that when the hot-injection reaction proceeded

for one hour, the $Cu_{1.5}Te$ phase is accompanied by an elemental Te impurity, which raised the possibility that the nanosheets were composed of Te alone.[190–192] STEM-EDS analysis of the nanosheets, shown in Figure 4.2, revealed that the two-dimensional sheets actually

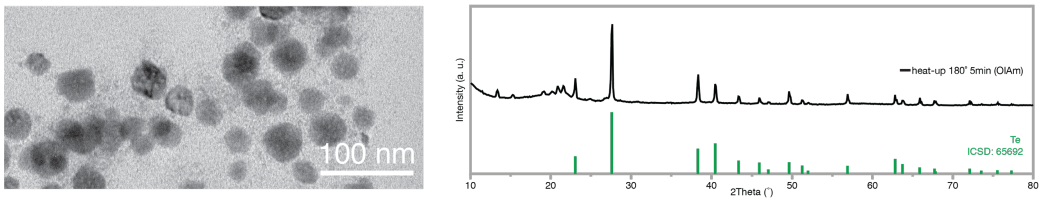

Figure 4.3 TEM and XRD analysis of Te(0) nanocrystals synthesized in OlAm at 180 ˚C for 5 minutes.

comprised copper and tellurium. It was found in subsequent experiments that didodecyl ditelluride would actually nucleate elemental tellurium at the reaction temperature of 180 ˚C (Figure 4.3), which accounts for the presence of the Te(0) signals in the XRD data since an excess of the ditelluride precursor was used.

Replacing OlAm with oleic acid resulted in the products depicted in Figure 4.4. At low temperatures and shorter reaction times, the products are primarily cube-like in morphology. In a heat-up synthesis to 135 ˚C for 30 minutes, the cube-like product had a size of 39 ± 13 nm (N = 100), closely resembling the TEM image of the hot-injection product shown in Fig. 4.4. A hot-injection synthesis at 180 ˚C resulted in cube-like NCs

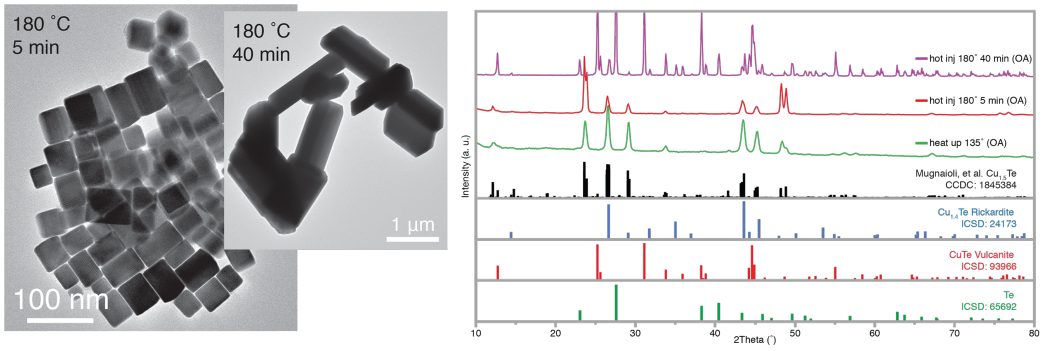

Figure 4.4. TEM images and XRD analysis of copper(I) telluride NCs. TEM images are of NC product from a hot-injection synthesis at 180 ˚C in OA. The NCs depicted were 48 ± 15 nm (N = 100) in the 5-minute aliquot, but at 40 minutes the crystals were on the order of microns in size. XRD patterns of the two samples shown are presented in addition to a heat-up synthesis at 135 ˚C which also resulted in cube-like NCs. In addition to the pseudo-cubic phase ($Cu_{1.5}Te$, CCDC: 1845384) seen in the heat-up synthesis and 5 minute hot-injection aliquot, the 40 minute hot-injection sample was indexed to Rickardite ($Cu_{1.4}Te$, ICSD: 24173), Vulcanite (CuTe, ICSD: 93966) and elemental tellurium (ICSD: 65692).

measuring 48 ± 15 nm (N = 100) after 5 minutes, but left for a total of 40 minutes the product had reached the micron-scale. XRD revealed the familiar pseudo-cubic $Cu_{1.5}Te$ crystal structure at low temperatures and shorter reaction times. However, the 40 minute 180 ˚C sample was indexed to a mixture of $Cu_{1.4}Te$, CuTe and elemental Te (Fig. 4.4 XRD).

These results reveal an interesting dichotomy between OlAm and OA surface chemistry in the $Cu_{2-x}Te$ NC system. The coordination of OlAm to the surface of the NCs is rather complex, with several morphologies resulting from syntheses performed at higher temperatures. In this case, there is a notable absence of disordered aggregation; instead nanorods and nanosheets are seen in the final product. OA appears to adsorb weakly in comparison, based on the micron-scale crystals that appeared at elevated temperatures, which is evidence of Ostwald ripening and/or aggregation. XRD analysis of the samples generated in coordinating solvents shows that the pseudo-cubic $Cu_{1.5}Te$ phase is the prevailing crystal structure. Longer reactions at higher temperatures lead to the presence of elemental Te in both solvents. This could be due to the nucleation of excess DD_2Te_2 as a function of time, or the instability of crystalline $Cu_{2-x}Te$ at high temperatures. The latter point may also explain the presence of substoichiometric $Cu_{2-x}Te$ phases in the OA hot-injection synthesis shown in Figure 4.4.

The possibility of the coordinating solvents (namely OlAm) interfering with the decomposition of DD_2Te_2 was potentially problematic, as the subsequent release of Te-containing species could be affected. There are examples in the literature of OlAm being used to prepare Te-containing NC precursors,[193,194] and if the OlAm were complexing with Te prior to monomer formation and nucleation, the unique chemistry of the dichalcogenide

would be nullified. With this in mind, an additional series of heat-up experiments was performed in dioctyl ether (DOE).

Figure 4.5 shows the results of syntheses performed at 135 ˚C and 155 ˚C in DOE. Unlike the $Cu_{2-x}Se$ product (Chapter 3) obtained in the non-coordinating solvent ODE, the lack of an additional ligand species yielded nanocrystalline products that were much larger and less uniform in morphology compared to the commonly seen nanodisks of $Cu_{2-x}Se$. Without the added coordinating ligand (OlAm or OA), the nanosheet morphology was prevalent in these samples, appearing alongside larger cube/rod-like NCs at 135 ˚C, then as the primary morphology at 155 ˚C. Large aggregates of material were seen in the TEM images of samples synthesized at 155 ˚C (see inset Figure 4.5), similar to the samples prepared at elevated temperatures in OA (Figure 4.4). XRD analysis still showed trace amounts of the pseudo-cubic $Cu_{1.5}Te$ phase, however substoichiometric phases were more prevalent in addition to elemental Te. Aggregation is an issue in these examples, which is

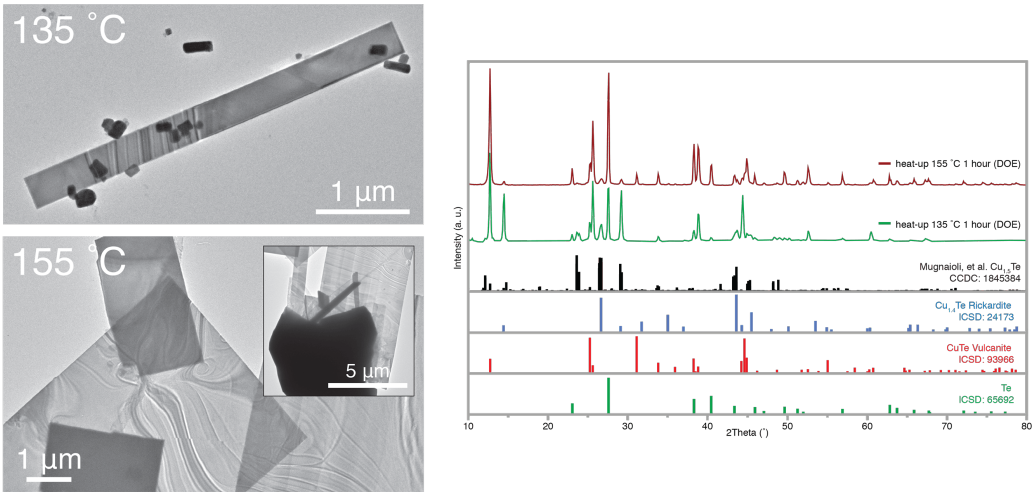

Figure 4.5. TEM images and XRD analysis of $Cu_{2-x}Te$ NCs resulting from heat-up syntheses to 135 and 155 ˚C in DOE for 1 hour. TEM reveals the formation of nanosheets similar to the results of the hot-injection syntheses in OlAm. At 135 ˚C, some rod-like NCs are present, but these are absent in the 155 ˚C sample. The inset image at 155 ˚C shows an aggregated mass of material from which several nanosheets emanate. Both samples can be indexed to the pseudo-cubic phase ($Cu_{1.5}Te$, CCDC: 1845384), Rickardite ($Cu_{1.4}Te$, ICSD: 24173), Vulcanite (CuTe, ICSD: 93966) and elemental tellurium (ICSD: 65692).

not surprising due to the lack of coordinating solvents (in addition to DD_2Te_2), and the sintering of particles (and nanosheets) could account for the wide range of crystal structures present in the XRD analysis of these samples. It has been shown previously that nanocrystal sintering can facilitate phase change;[161] this coupled with a lack of stabilizing surface

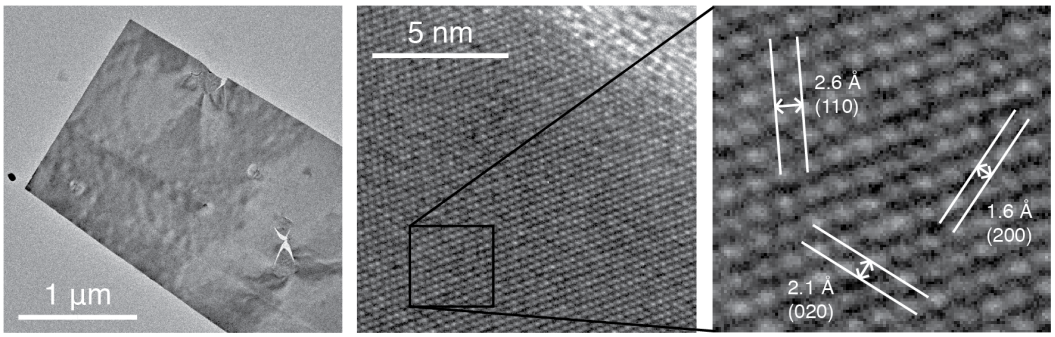

Figure 4.6. TEM images of a $Cu_{2-x}Te$ nanosheet with HR-TEM images indexed to Vulcanite CuTe (ICSD: 93966).

chemistry and the mobility of Cu ions in the copper telluride system[179] could potentially cause a range of phases in the sample as a whole if the Cu:Te stoichiometry was in flux.

Quantitative EDS analysis of the nanosheets seen in Figure 4.5 (155 ˚C) showed the nanosheets were composed of 46.4% Cu and 53.6% Te. HR-TEM images shown in Figure 4.6 revealed lattice fringing that could be indexed to the Vulcanite (CuTe) crystal structure. FFT analysis was used to identify the lattice planes (200), (020) and (110), and results were matched to a Vulcanite reference pattern (ICSD: 93966). Measured d-spacings were 1.6 Å for (200), 2.1 Å for (020) and 2.6 Å for (110), compared with reference values of 1.58 Å, 2.05 Å and 2.50 Å, respectively. The crystal structure of Vulcanite is orthorhombic and stacked along its c-axis with layers of CuTe. A layered structure is also characteristic of the hexagonal Cu_2Te phase, of which nanosheets have also been synthesized.[175] However, the stoichiometry determined by quantitative EDS makes the hexagonal phase unlikely in this case. One other instance of 2-dimensional Vulcanite nanomaterials is present in the literature, as She, et al. were able to electrochemically grow

"nanoribbons" of that material on an ITO electrode.[195] Preliminary in-plane XRD analysis of the sample shown in Figure 4.6 proved inconclusive, though additional work in this area is planned.

The primary phase seen in the diffraction patterns presented here, pseudo-cubic $Cu_{1.5}Te$, is metastable per Mugnaioli, et al., and there are several additional phases in the ~1.5:1 Cu:Te stoichiometry range[180] which could be accessed through different NC precursors. Phase control may be possible with an additional ditelluride precursor, or a tellurol could be processed through a redesigned synthesis, which could lead to a more-thermodynamically favored crystal structure if the NC synthesis follows the same pattern as the $Cu_{2-x}Se$ system. Density functional theory (DFT) analysis of the Te precursors shown in Figure 4.7 follows a trend similar to the corresponding diselenide and selenol discussed in Chapter 3, though the Te precursors are markedly more reactive overall. Determining whether a single-source precursor is formed through the reaction of a tellurol and copper(I) precursor (behavior seen in copper sulfides and selenides) is of significant investigatory interest, as this precursor complex formation was crucial to the synthesis of the thermodynamic $Cu_{2-x}Se$ phase in Chapter 3.

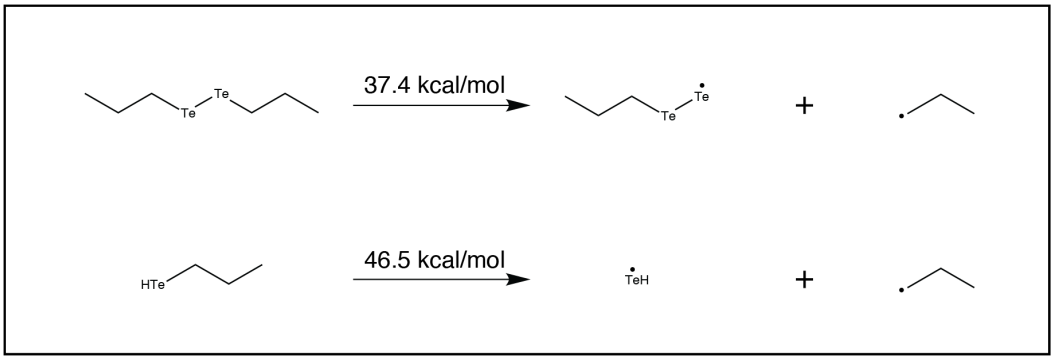

Figure 4.7. DFT analysis of C-Te bond dissociation energies for DD_2Te_2 and DDTeH. For comparison, the DD_2Se_2 and DDSeH C-Se BDE values were 55.4 and 67.8 kcal/mol, respectively.

4.4 Conclusion

In this chapter, the synthesis of $Cu_{2-x}Te$ NCs was explored using a ditelluride precursor. Several tellurol syntheses were attempted, but instability due to a tendency toward oxidation prevented processing and the possibility of straightforward handling. Future attempts at this synthesis could involve the use of a glovebox and measures preventing photooxidation. NC syntheses using OlAm and OA primarily resulted in particles with the pseudo-cubic $Cu_{1.5}Te$ crystal structure. Low temperatures and short reaction times typically resulted in cube-like particles in OlAm and OA. At higher temperatures and longer reaction times rod-like particles and nanosheets were seen in OlAm, but micron-scale crystals were produced in OA. In the non-coordinating solvent DOE, larger NCs and nanosheets were synthesized. Powder XRD indicated a range of stoichiometries resulted from the syntheses in DOE, including the pseudo-cubic $Cu_{1.5}Te$ phase, Rickardite ($Cu_{1.4}Te$), Vulcanite (CuTe) and elemental Te. Further development of this synthesis would aim to produce the Vulcanite nanosheets without the accompanying aggregations that may be the source of the additional phases seen in XRD analysis. Nanosheets were indexed to the Vulcanite phase, to the author's knowledge marking the first such instance of nanosheets of this crystal structure. Further investigation of the nanosheet phase using in-plane XRD is planned.

4.5 Experimental Methods

Materials. Dioctyl ether (98%), oleic acid (90%, technical grade), 1-octadecene (ODE, 90% technical grade), oleyl amine (70%, technical grade) were obtained from Sigma

Aldrich. Sodium borohydride was obtained from Fisher Chemicals. $Cu(acac)_2$ (≥98%) was obtained from Strem. All materials were used as received without additional purification.

Synthesis of didodecyl ditelluride. This synthesis was adapted from the work of Li, et al.[187] by collaborator Prof. Ahmed Nuriye. A mixture of Te powder (3 g, 23.6 mmol) and $NaBH_4$ (0.71 g) in 30 mL dimethylformamide (DMF) was refluxed at 85 ˚C for 20 minutes. Separately, 5.67 mL (23.6 mmol) of 1-bromododecane was mixed with 10 mL of DMF, added to the dark purple solution and stirred for 3 hours. The mixture was filtered to remove unreacted Te, and the red solution was extracted with hexane/water. Hexane was evaporated to leave a solid product of didodecyl ditelluride (DD_2Te_2).

Synthesis of dodecyl tellurol. This synthesis was adapted from the work of Uemura, et al.[188] Standard Schlenk-line techniques were used throughout this procedure. Into an oven-dried vial, 1.68 mmol of didodecane ditelluride was added and degassed for 1 hour while being warmed in a water bath to melt the ditelluride. In a 100 mL round-bottom flask, 2.64 mmol of $NaBH_4$ was placed under vacuum for 1 hour and subsequently placed under Ar gas. The ditelluride was then transferred into a nitrogen-containing glovebox where it was dissolved in 7 mL of anhydrous hexanes and added to a syringe. A second syringe was prepared with 10 mL of anhydrous ethanol. The round bottom flask was placed in an ice bath, and the ethanol was added slowly to the $NaBH_4$. The red ditelluride solution was then slowly added to the flask over 60 seconds, bubbling was observed and the solution became colorless. Evaporating the low-boiling solvents with vacuum left a yellow-white solid that

would not melt with a heat gun. Left overnight under vacuum the contents of the flask had turned red, indicative of oxidation.

Synthesis of $Cu_{2-x}Te$ nanocrystals. Standard Schlenk line techniques were used throughout with Ar as the inert gas. In a typical heat-up synthesis, 0.55 mmol of didodecyl ditelluride, 0.25 mmol of $Cu(acac)_2$, and either 2.5 or 5 mL of solvent (ODE, OlAm, OA, DOE) were mixed in a 25 mL 3-necked flask. In a hot-injection synthesis, 0.55 mmol of didodecyl ditelluride was mixed in 0.5 mL of the solvent used in the reaction flask in an N_2-filled glovebox. The flask was put under vacuum and the temperature was raised to 80 ˚C for 30 min. Then the flask was put under inert atmosphere and the temperature was raised to the reaction temperature. At this point in a hot-injection synthesis, the ditelluride was injected. The reaction flask was held at temperature from 30 minutes to 2.5 hours. The flask was allowed to cool to room temperature, and the post-reaction mixture was precipitated in acetone three times and resuspended in chloroform.

Instrumentation. Transmission Electron Microscopy (TEM) was performed on a FEI Technai Osiris digital 200 kV S/TEM system. Solution absorption spectra were obtained on a Jasco V-670 UV-Vis-NIR spectrophotometer in tetrachloroethylene. X-ray diffraction (XRD) measurements were done using a Rigaku SmartLab powder X-ray diffractometer with a CuKα (λ = 0.154 nm) radiation source set to 40 kV and 44 mA, and a D/teX Ultra 250 1D silicon strip detector. XRD patterns were acquired using a step size of 0.1 degrees at 1 or 10 degrees per minute.

Computational Methods. The computational methods performed herein were adapted from the works of Guo et al.[156] and Rhodes et al.[139] Bond dissociation energies were calculated using Gaussian 16 with density functional theory (DFT) and the Boese− Martin kinetics (BMK) functional. Molecular geometry optimization was performed using the def2SVPD basis set which includes a 28-electron pseudopotential on tellurium, and single-point energy calculations were performed using the def2TZVPD basis set with the same pseudopotential on tellurium.

Chapter 5

CONCEPTS AND PRELIMINARY WORK

5.1 Phase Control of Additional Semiconductor NCs Using Selenol and Diselenide

Concurrent with the initial investigation and publication covering the synthesis of wurtzite and cubic $Cu_{2-x}Se$ using two different selenium-containing precursors (discussed in Chapter 3), work was expanded to other semiconductor systems. The goal was to explore whether phase control was possible in these additional metal selenide systems based upon the reactivity of the diselenide and selenol precursor species. What follows is a discussion of the preliminary results acquired pertaining to that end. In total, metal selenide NCs were synthesized of ZnSe, PbSe, NiSe, Ag_2Se, and CdSe. Smaller nanoparticles lacking easily-identified powder diffraction reflections of nickel selenide were also synthesized. Primarily, the groundwork was laid with the selenol precursors to develop standardized syntheses for each material, for which diselenide-based syntheses could later be investigated.

Zinc selenide NCs were studied initially due to its prevalence in the literature, and its well-known zinc blende and wurtzite polytypism. ZnSe is a direct bandgap semiconductor[196] with a bulk bandgap of 2.7 eV, known for emitting blue light bordering on the UV.[197] Initial experiments involved heat-up syntheses to 290 ˚C using $Zn(OAc)\bullet 2H_2O$ and tetradecyl selenol as NC precursors in the non-coordinating solvent dioctyl ether (DOE). The thermodynamically stable zinc blende ZnSe phase[198] resulted, though colloidal stability was poor and morphologically the NCs were non-uniform and aggregated (as seen in TEM, results not shown). The reaction mixture was cloudy (though

orange-red in color), which made identifying the beginning of nucleation difficult. This was likely due to the lack of a stable surface ligand at the high temperature of 290 ˚C. Colloidally stable fluorescent zinc blende ZnSe NCs resulted when the Zn precursor was heated to 280 ˚C in the presence of a 2:1 stoichiometric amount of oleic acid, which formed an optically colorless solution prior to the injection of the selenol. The results of this synthesis can be seen in Figures 5.1 and 5.2. Using a Zn-carboxylate compound as a precursor to ZnSe was suggested by Li, et al., of Xiaogang Peng's group.[199] However, their synthesis used Se/phosphine precursors and reaction temperatures of 310˚ to 330˚.

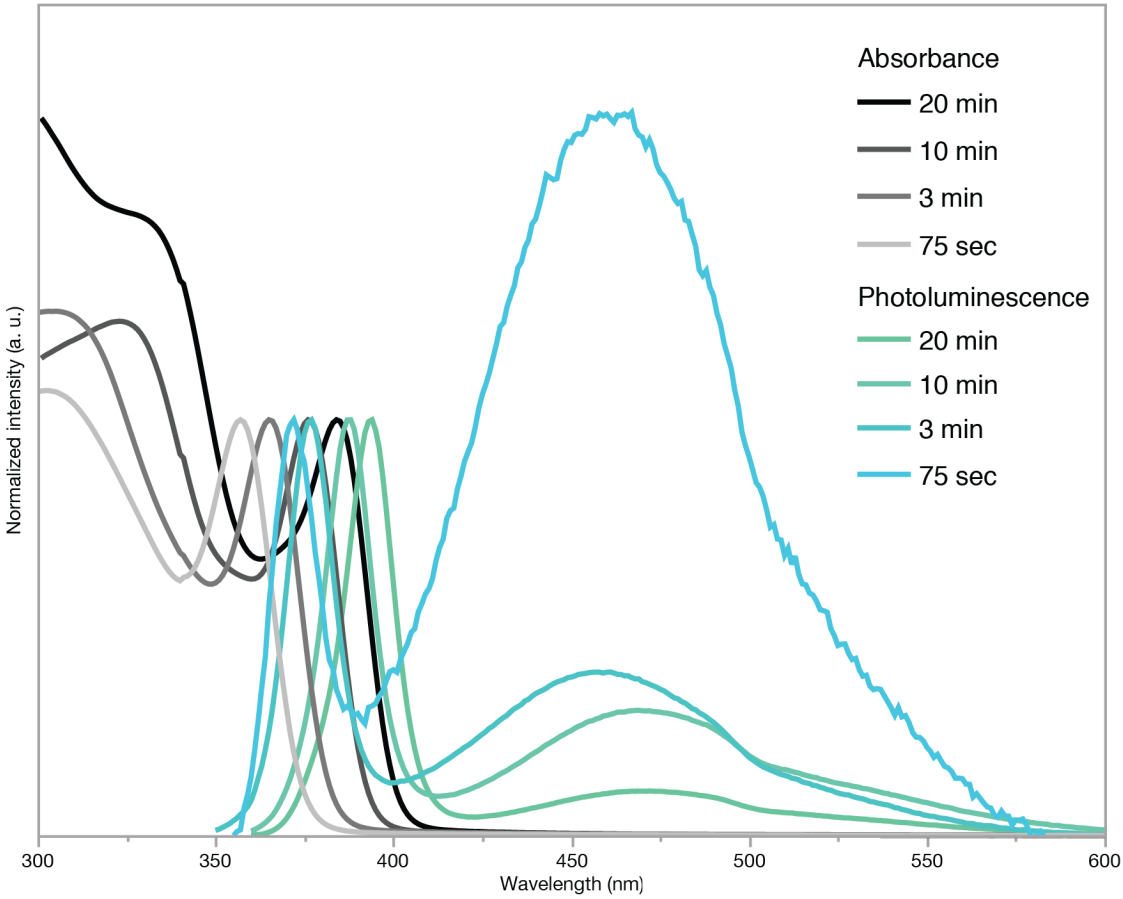

Figure 5.1. UV-Vis and photoluminescence spectra of colloidal ZnSe nanocrystals in hexanes. Samples were acquired at 75 seconds, 3, 10 and 20 minutes after the injection of the selenol. Band edge photoluminescence is seen in the range 372 to 394 nm.

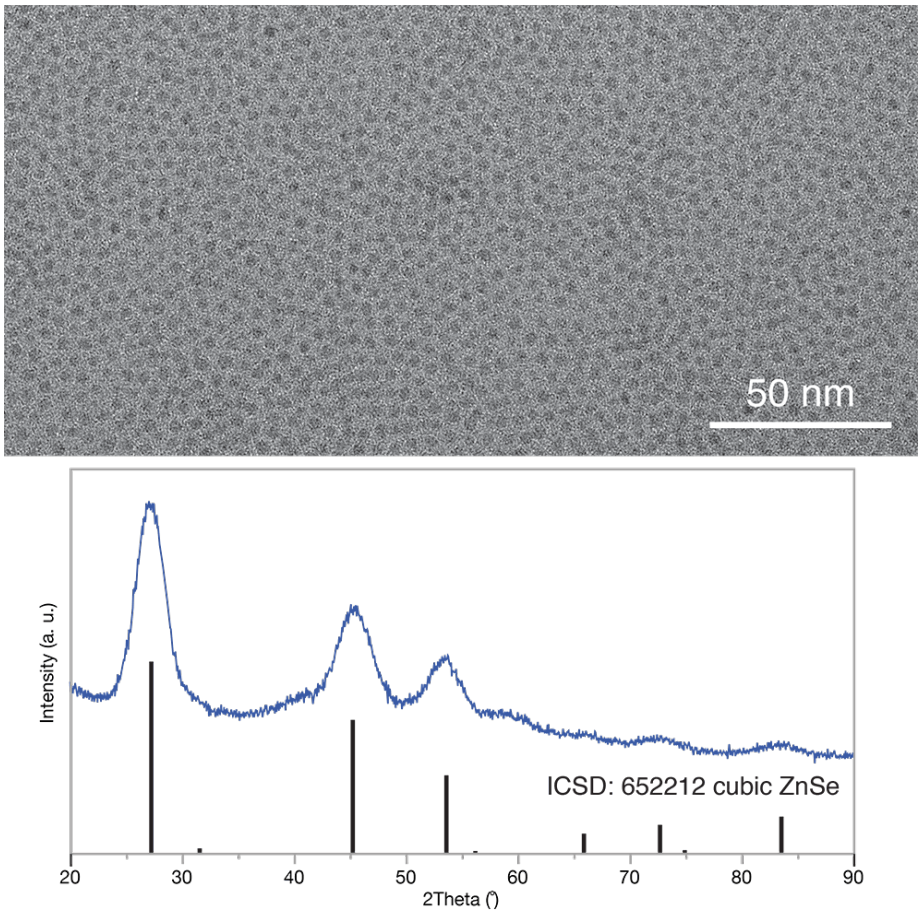

Figure 5.2. TEM of ZnSe NCs, and powder XRD which identified the phase as zinc blende (ICSD: 652212). Both samples are from the 20-minute aliquot from Figure 5.1.

The results from 20 minutes at the reaction temperature of 280 ˚C (Fig. 5.2) have a photoluminescence quantum yield (PLQY) of ~3.5%,[166] which is in agreement with Li, et al. who wrote that ZnSe NCs grown solely with oleic acid typically had weak PLQY (below 10%), though the presence of amines during synthesis could improve this dramatically.[199] The photoluminescence full-width-at-half-max of the NCs described by Li, et al. was 12-15 nm, while the results reported here were approximately 16 nm for the 20 minute sample from band edge emission in Figure 5.1.

Ultimately, as the work with the $Cu_{2-x}Se$ NC system progressed, the Se precursors were changed from the tetradecyl selenol synthesized following Berends, et al.[154] to the

dodecyl selenol and didodecyl diselenide of Dilimon, et al.[167] This change was done due to the ease of processing the dodecyl selenol (liquid at room temperature), its higher purity (due to a vacuum distillation step) and the reliability of the Dilimon *diselenide* synthesis (initially, diselenide had ostensibly been synthesized by exposing selenol to air, however NMR revealed several oxidation products resulted in addition to the diselenide). A new ZnSe NC synthesis with the higher-purity dodecyl selenol was developed (results not shown here), however didodecyl diselenide (discussed in Chapter 3) did not react when substituted directly into the ZnSe synthesis discussed above. The post reaction mixture contained no appreciable amount of nucleated nanocrystals, rather a white powder that was likely zinc oleate. Further development could result in a ZnSe synthesis with the diselenide precursor; as was found in Chapter 3, the selenol was actually more reactive than the diselenide due to the formation of metal selenoate complexes. Higher temperatures and longer reaction times could be explored to foster nucleation of ZnSe.

Lead selenide nanocrystals were also investigated, though there was no precedent for a hexagonal phase with that material (similar to the copper(I) selenide system in which there was only one literature precedent for the hexagonal phase[106]). Preliminary results with the selenol being substituted for the sulfur precursor bis(trimethylsilyl)sulfide (TMS) in a PbS synthesis reported by Scholes, et al.[200] resulted in the familiar rock-salt PbSe NCs depicted in Figure 5.3. The groundwork is laid for additional experimentation with diselenide precursors.

Subsequently, the investigation of nickel selenide yielded several different morphologies under a range of reaction conditions. Ni_xSe has several known phases based on differing stoichiometries but has not been exhaustively explored in the literature. This

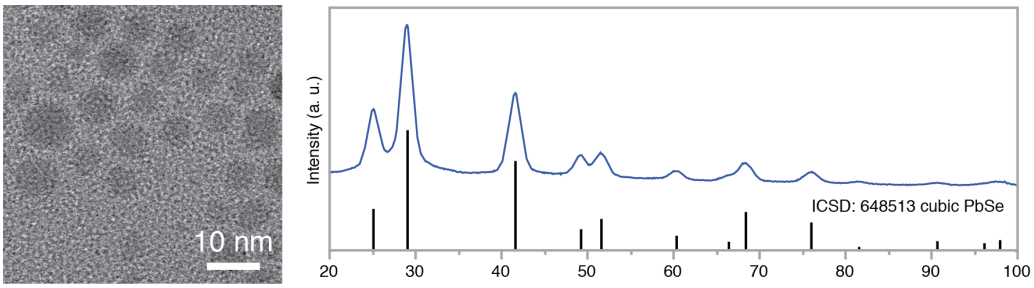

Figure 5.3. TEM and XRD analysis of cubic PbSe nanocrystals matched to reference pattern ICSD: 648513.

material holds promise as a replacement for precious metals in catalytic applications.[201] Herein it was observed that Ni precursors (like $Ni(acac)_2$ and $NiCl_2$) would react with the selenol and nanoparticles would nucleate at room temperature (Figure 5.4) and in one case 2 ˚C.

The low-temperature Ni_xSe syntheses yielded results that were difficult to characterize with XRD; this was due to the broadness of the reflections which can be attributed to the very small domains. These cluster-like domains may have a high degree of atomic mobility,[202] further affecting the XRD characterization. One relatively sharp peak

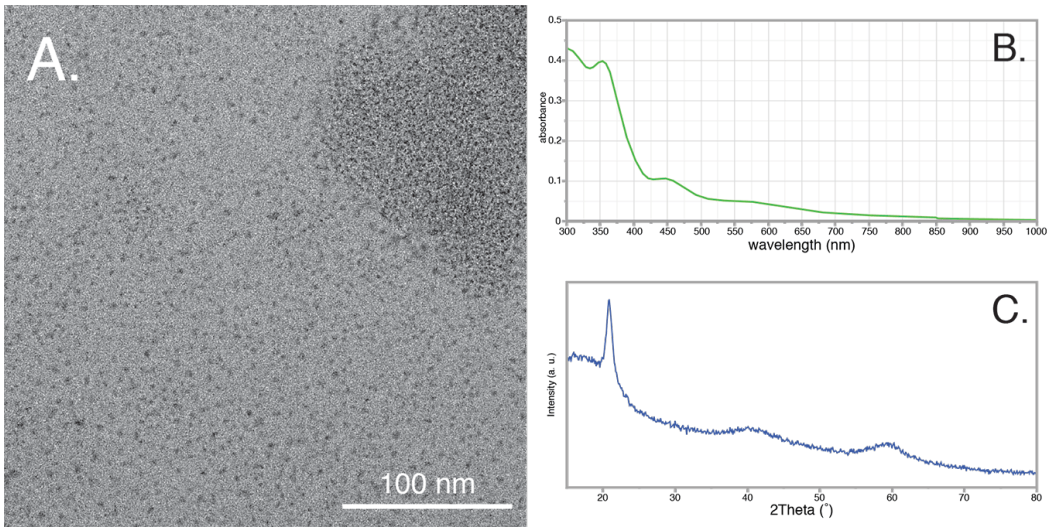

Figure 5.4. TEM, UV-Vis and XRD characterization of two similar Ni_xSe reactions. A and B represent a synthesis using $Ni(acac)_2$, ODE and DDSeH, which were mixed at room temperature for 45 minutes. The XRD pattern in C is the result of mixing $Ni(acac)_2$ in pure DDSeH for 45 minutes. Qualitatively, the results are similar based on the TEM and XRD of both samples. When the nickel precursor is mixed with selenol, there is an instantaneous color change from pale green [solution or powder] to brown/black. Note that the XRD pattern has not been baseline corrected to preserve the broad signals.

in the XRD pattern at 21˚ remains unidentified, though this could be unreacted precursor or reaction side-products that were not removed during cleaning. Similar cluster-like particles of PdSe were synthesized by Dr. Emil Hernandez that also had a corresponding single peak in the XRD pattern (with two accompanying broad signals), though to this point no further investigation has been conducted.

Following these experiments, different nickel precursors were used as well as higher reaction temperatures to foster growth of larger crystalline particles. Making Ni-oleate in situ and injecting selenol at 250 ˚C resulted in large aggregated crystals like those in Figure 5.5. These large crystals were indexed to the well-known hexagonal NiSe phase Sederholmite,[203] however this material was not colloidal.

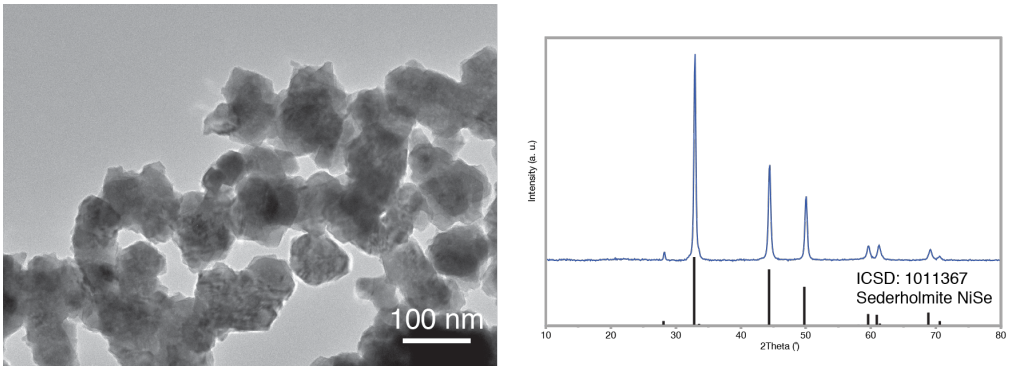

Figure 5.5. TEM and XRD analysis of NiSe nanocrystal aggregates, XRD pattern is indexed to Sederholmite ICSD: 1011367

A promising middle ground was found using oleyl amine and NiCl at 200 and 250 ˚C that resulted in nanocrystals of NiSe. Figure 5.6 highlights these results and shows that the crystallites are on the order of 10's of nanometers in diameter. Compared to the cluster-like particles of Fig. 5.4, the UV-Vis spectra in Fig. 5.6 is indicative of scattering and possibly polydispersity (evidence for quantum confinement has been seen in flower-like crystals of NiSe that had dimensions qualitatively comparable to the NCs discussed here, though specifics on the Bohr radius were not provided[204]). The scattering could be

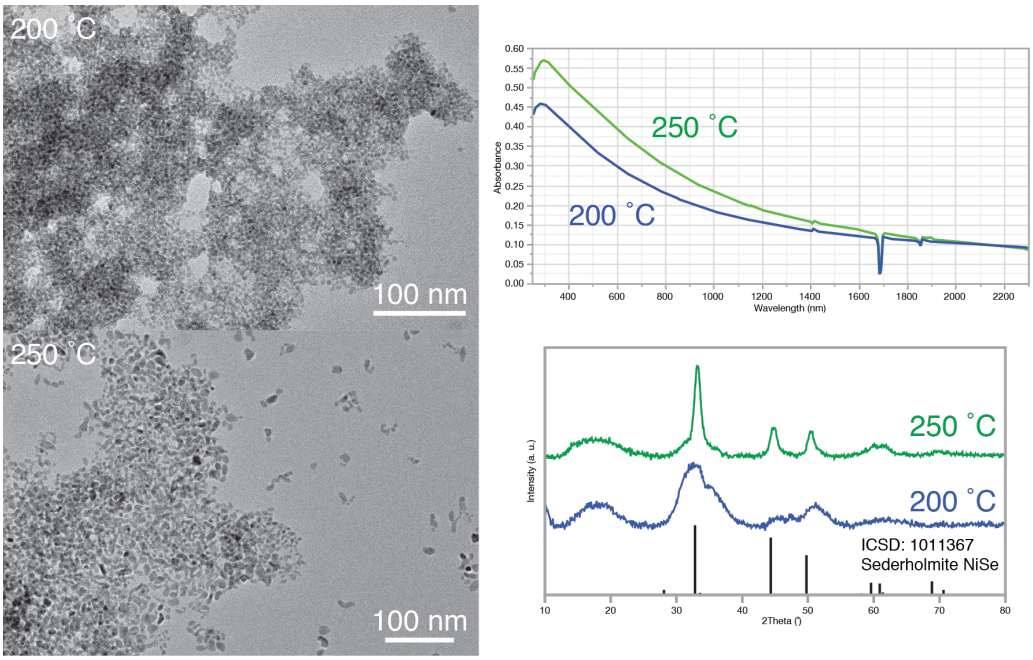

Figure 5.6. TEM, UV-Vis and XRD of Ni_xSe nanocrystals synthesized at 200 and 250 ˚C

attributed to a lack of colloidal stability in the particles that result from this synthesis. Additional work can be done to improve the colloidal stability of these NCs, as the particles tended to flocculate with time. Quantitative EDS revealed that the 200 ˚C sample was composed of 54.4% Se and 45.6% Ni, and the 250 ˚C sample was 50.6% Se and 49.4% Ni. The slightly higher concentration of selenium in the first sample is likely due to the smaller-sized particles and their larger relative surface area being Se-rich due to the presence of selenium-containing ligands.

Diselenide syntheses were briefly explored, but the temperature at which crystalline material would nucleate was difficult to identify. Further work in this area could develop a comparable synthesis scheme between the selenol and diselenide precursors.

Lastly, with the Ni_xSe system, attempts were made to crystallize the cluster-like particles from Figure 5.4, using the short ligand 4-tert-butylbenzyl selenol. This ligand was synthesized following the standard selenol synthesis of Dilimon, et al.,[167] which was used

in Ch. 3. Adapting the conditions used by Dieter Fenske's group for copper sulfide clusters (see experimental section for details, Fenske's work is also discussed later in section 5.2),[205] samples with varying stoichiometric ratios of Ni precursor to selenol were prepared, but attempts to crystallize the material were unsuccessful. The implication of this is that the particles are not uniform in weight or morphology.

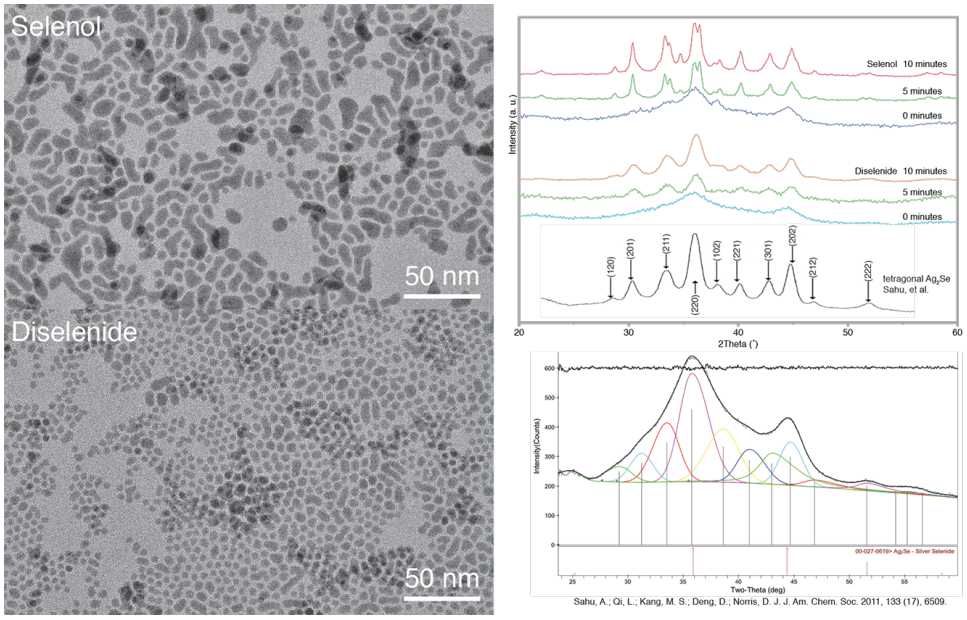

Figure 5.7. TEM and XRD analysis of Ag_2Se nanocrystals synthesized using dodecyl selenol and didodecane diselenide at 200 ˚C. TEM images are of aliquots taken at 0 minutes of reaction time (having just reached 200 ˚C). XRD reflections can be attributed to the metastable tetragonal phase described by Sahu, et al. in both the selenol and diselenide syntheses. As noted by Sahu, smaller NCs (in this case from shorter reaction times) may appear to match cubic Ag_2Se, however Sahu was able to achieve a better fit for these XRD patterns with the metastable tetragonal phase that they described (see Sahu's figure on bottom right). For reference, two components of this figure were reprinted from the publication by Sahu, et al., they are the reference pattern for the tetragonal phase (below the six XRD patterns), and the peak-fitting figure on the bottom right which highlights the signals attributed to the tetragonal phase. Reprinted with permission from *J. Am. Chem. Soc.* 2011, 133, 17, 6509-6512. Copyright 2011 American Chemical Society.

Silver selenide NCs were also synthesized with both selenium-containing precursors. Ag_2Se has a low temperature orthorhombic phase, a high temperature cubic phase that has desirable superionic conducting properties,[206] and a metastable tetragonal phase only present in nanoscale samples that was identified in 2011 by David Norris's group.[207] Experiments with this material yielded the metastable tetragonal phase with both selenol and diselenide precursors as depicted in Figure 5.7. As noted by Sahu, et al. (of the

Norris group), smaller tetragonal NCs can nonetheless be fit to the metastable phase's pattern, even though they may appear to be of the cubic phase (see Fig. 5.7 bottom right). Additional work could lead to phase control with the other documented phases, as there are many potential precursor and reaction condition combinations that could be explored.

Finally, the CdSe NCs were briefly investigated, however it was found that the zinc blende phase resulted when either selenol or diselenide were used under similar conditions (Figure 5.8). As discussed in the introductory chapter, the CdSe system has two characteristic phases (zinc blende and wurtzite) that are very close in energy as noted by Peng's group.[101] Further work with these diselenide/selenol precursors may realize phase control with the CdSe system.

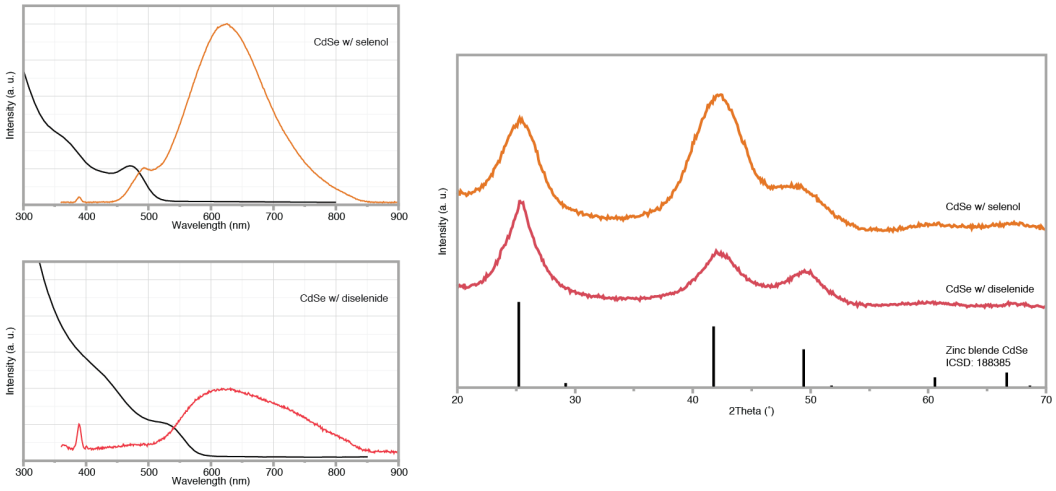

Figure 5.8. UV-Vis, fluorescence and XRD data for CdSe NCs synthesized with dodecyl selenol and didodecane diselenide. Spectroscopic data has been normalized. XRD patterns were matched to zinc blende CdSe (ICSD: 188385).

The preliminary work detailed in this section warrants further investigation, namely with the diselenide precursor. Promising results were achieved using the selenol precursors with ZnSe, PbSe, Ni_xSe, Ag_2Se and CdSe, though all of the phases obtained had literature precedents. Additional work with the diselenide could yield metastable phases of these

materials due to its reactivity differences in a synthesis environment compared to the selenol.

These results not only serve as foundational work for further study, but also (through comparison) highlight the unique chemistry of the $Cu_{2-x}Se$ NC phase control syntheses discussed in Chapter 3. Though phase control with the diselenide/selenol may be possible with the materials discussed above, the dynamics of $Cu_{2-x}Se$ NC synthesis include several significant factors that warrant exposition in light of these results. First, no additional stabilizing ligands are necessary with $Cu_{2-x}Se$ NCs synthesized with these Se-containing precursors, however the presence of additional ligands was found to be necessary with all of the materials discussed above. Added ligands complicate the reaction mixture and undoubtedly have effects on precursor decomposition and NC surface chemistry, both of which are key factors in NC crystal structure formation.

The $Cu_{2-x}Se$ NC *nucleation temperature* also fortuitously coincides with the *phase transition temperature* from hexagonal to cubic. Importantly, there is also a qualitative correlation with the diselenide and Cu-selenoate *decomposition temperatures*. This confluence of reaction characteristics results in a slow, controlled nucleation of $Cu_{2-x}Se$ which is crucial for formation of the monodisperse, metastable hexagonal phase NCs. For comparison, the ZnSe NCs discussed at the beginning of this section nucleated at 280 ˚C and required the presence of oleic acid to complex and dissolve the Zn precursor (and likely stabilize the nascent NCs). Se-precursor decomposition temperature could change depending on the metal and metal precursor, but the ZnSe NC synthesis takes place at over 100 ˚C beyond the $Cu_{2-x}Se$ NC synthesis. This may or may not obscure the different effects of the two Se-precursors.

Going forward, materials that nucleate closer to the 150-180 ˚C range could be investigated to enable coordination of the Se-containing ligand species (which likely were too labile or decomposed at higher temperatures), making additional ligand species and their effects unnecessary. If a known (or heretofore unknown) phase transition exists in this temperature range for these materials, the diselenide/selenol system may be able to access those metastable phases.

5.1.1 Experimental Methods

Materials. $Zn(OAc)\bullet 2H_2O$, dioctyl ether (98%), PbO, $Ni(acac)_2$ (95%), $NiCl\bullet 4H_2O$ (99.9%), $NiOAc_2\bullet 4H_2O$, Ag(acac) (98%), oleic acid (90%, technical grade), 1-octadecene (ODE, 90% technical grade), oleyl amine (70%, technical grade) were obtained from Sigma Aldrich. All materials were used as received without additional purification.

Synthesis of 1-tetradecyl selenol. This synthesis was adapted from the work of Berends, et al.,[154] and the selenol product was stored in a N_2-filled glovebox to prevent oxidation.

Synthesis of 1-dodecyl selenol. This synthesis was adapted from the work of Dilimon, et al.,[167] and a procedure identical to the one presented in Chapter 3 was followed.[186]

Synthesis of ZnSe Nanocrystals. This synthesis was partially adapted from the work of Li, et al.[199] Standard Schlenk line techniques were used throughout with argon as the inert gas. In a typical synthesis, 0.5 mmol of $Zn(OAc)\bullet 2H_2O$, 2.15 mL of dioctyl ether and 1.0 mmol of oleic acid were mixed in a 25 mL 3-necked flask. The flask was put under vacuum

and the temperature was raised to 120 ˚C for 4 hours. The solution would become transparent. In a glovebox, 1-tetradecyl selenol was warmed (just above ambient temperature) to melt and withdrawn with a syringe (0.5 mL total). The syringe needle was stopped with a rubber septum to prevent selenol oxidation prior to injection. The flask was put under inert atmosphere and the temperature was raised to 280 ˚C and the 0.5 mL of 1-tetradecyl selenol was injected. The reaction was left to proceed with aliquots being taken at different intervals. The flask was allowed to cool to room temperature, and the post-reaction mixture was precipitated in 1:1 2-propanol and methanol three times and resuspended in hexanes.

Synthesis of PbSe Nanocrystals. This synthesis was partially adapted from the work of Scholes, et al.[200] Standard Schlenk line techniques were used throughout with argon as the inert gas. In a typical synthesis, 0.4 mmol of PbO and 4 mL of oleic acid were mixed in a 25 mL 3-necked flask. The flask was put under vacuum and the temperature was raised to 150 ˚C overnight. In a glovebox, 0.2 mmol dodecyl selenol and 2 mL of octadecene were added to a syringe. The syringe needle was stopped with a rubber septum to prevent selenol oxidation prior to injection. The flask was put under inert atmosphere and the temperature was left at 150 ˚C and the dodecyl selenol was injected. The reaction was left at temperature for 1 hour. The flask was allowed to cool to room temperature, and the post-reaction mixture was precipitated in acetone three times and resuspended in hexanes.

Synthesis of Ni_xSe Cluster-like Nanoparticles. Standard Schlenk line techniques were used throughout with argon as the inert gas. In a typical synthesis, 0.5 mmol of $Ni(acac)_2$

and 5 mL of octadecene were mixed in a 25 mL 3-necked flask. The flask was put under vacuum at room temperature. In a glovebox, 1.915 mmol dodecyl selenol was added to a syringe. The syringe needle was stopped with a rubber septum to prevent selenol oxidation prior to injection. The flask was put under inert atmosphere and the temperature was left at room temperature and the dodecyl selenol was injected. The reaction was left at temperature for 45 minutes. The flask was allowed to cool to room temperature, and the post-reaction mixture was precipitated in acetone, and then 2-propanol and resuspended in hexanes. Alternatively, 0.1 mmol of $Ni(acac)_2$ was added to a 1-dram vial with a stirbar, and transferred into a glovebox. Then 3.8 mmol of dodecyl selenol were added and the reaction was stirred for 45 minutes, at which time the sample was removed from the glovebox. The sample was precipitated in a mix of 2-propanol and MeOH four times and resuspended in hexanes.

Synthesis of Larger NiSe Aggregates. Standard Schlenk line techniques were used throughout with argon as the inert gas. In a typical synthesis, 0.5 mmol of $NiOAc_2 \bullet 4H_2O$ and 5 mL of oleic acid were mixed in a 25 mL 3-necked flask. The flask was put under vacuum and the temperature was raised to 120 ˚C for 2 hours. In a glovebox, 0.5 mmol dodecyl selenol and 0.37 mL of dioctyl ether were added to a syringe. The syringe needle was stopped with a rubber septum to prevent selenol oxidation prior to injection. The flask was put under inert atmosphere and the temperature was left at 250 ˚C and the dodecyl selenol was injected. The reaction was left at temperature for 4 minutes. The flask was allowed to cool to room temperature, and the post-reaction mixture was precipitated in 2-propanol three times and resuspended in $CHCl_3$.

Synthesis of NiSe Nanocrystals. Standard Schlenk line techniques were used throughout with argon as the inert gas. In a typical synthesis, 0.5 mmol of $NiCl_2$•$6H_2O$ and 5 mL of oleyl amine were mixed in a 25 mL 3-necked flask. The flask was put under vacuum and the temperature was raised to 120 ˚C for 1.5 hours. In a glovebox, 0.5 mmol dodecyl selenol and 0.37 mL of dioctyl ether were added to a syringe. The syringe needle was stopped with a rubber septum to prevent selenol oxidation prior to injection. The flask was put under inert atmosphere and the temperature was left at either 200 ˚C or 250 ˚C and the dodecyl selenol was injected. The reaction was left at temperature for 3 minutes. The flask was allowed to cool to room temperature, and the post-reaction mixture was precipitated in 2-propanol three times and resuspended in $CHCl_3$.

Synthesis of NiSe Clusters for Single Crystal Analysis. The precursor quantities used and crystallization strategy outlined here were adapted from the work of Bestgen, et al.[205] In a nitrogen-filled glovebox, $Ni(acac)_2$ was added to five 1-dram vials in the following amounts: 0.444, 0.222, 0.111, 0.075 and 0.0375 mmol. 3 mL of anhydrous toluene were added to each vial with stirring. To each vial, 0.222 mmol of 4-tertbutylbenzyl selenol (synthesized following the work of Dillimon[167]) was added with stirring. After 40 minutes, the vials were put under vacuum on a Schlenk line to remove the solvent. In a glovebox, 4.2 mL of heptane was added to each vial, followed by sonication and centrifugation. The supernatant from each vial was then transferred into five clean vials and stored in the glovebox refrigerator for five days. The precipitated material was then washed with

pentane, and small quantities were transferred into Parabar oil. Investigation under a light microscope revealed that the precipitated material was greasy, black and not crystalline.

Synthesis of Ag_2Se Nanocrystals. Standard Schlenk line techniques were used throughout with argon as the inert gas. In a typical synthesis, 0.5 mmol of Ag(acac) and 5 mL of oleyl amine were mixed in a 25 mL 3-necked flask. Different Se-containing precursors were added at this point. For didodecyl diselenide, 1.1 mmol of the solid was added to the flask. For dodecyl selenol, in a glovebox, 1.1 mmol of the dodecyl selenol was added to a syringe. The syringe needle was stopped with a rubber septum to prevent selenol oxidation prior to addition to the room temperature flask. The flask was put under vacuum and the temperature was raised to 80 ˚C for 1 hour. The flask was put under inert atmosphere and the temperature was heated to 200 ˚C. The reaction was left at temperature and aliquots were taken at 0, 5, 10, 30 minutes, and the reaction was stopped at 60 minutes. The flask was allowed to cool to room temperature, and the aliquots and the post-reaction mixture were precipitated in 2-propanol three times and resuspended in $CHCl_3$.

Synthesis of CdSe Nanocrystals. Standard Schlenk line techniques were used throughout with argon as the inert gas. In a typical synthesis, 0.5 mmol of $Cd(OAc)\bullet 2H_2O$ and 2.5 mL of oleic acid were mixed in a 25 mL 3-necked flask. The flask was put under vacuum and the temperature was raised to 120 ˚C for 2 hours. In a glovebox, 0.25 mL dodecyl selenol or didodecyl diselenide were added to a syringe. The syringe needle was stopped with a rubber septum to prevent selenol oxidation prior to injection. The flask was put under inert atmosphere and the temperature was raised to 250 ˚C and the Se precursor was injected.

The reaction was left at temperature until the reaction mixture turned red. For the selenol reaction this took approximately 25 seconds, for the diselenide reaction the color change took approximately 106 seconds. The flask was allowed to cool to room temperature, and the post-reaction mixture was precipitated in 2-propanol three times and resuspended in hexanes.

Instrumentation. Transmission Electron Microscopy (TEM) was performed on a FEI Technai Osiris digital 200 kV S/TEM system. Solution absorption spectra were obtained on a Jasco V-670 UV-Vis-NIR spectrophotometer in hexanes or chloroform. Fluorescence spectra were acquired using a Jasco FP-3800 spectrofluorometer. X-ray diffraction (XRD) measurements were done using a Rigaku SmartLab powder X-ray diffractometer with a CuKα ($\lambda = 0.154$ nm) radiation source set to 40 kV and 44 mA, and a D/teX Ultra 250 1D silicon strip detector. XRD patterns were acquired using a step size of 0.1 degrees at 1 or 10 degrees per minute.

5.2 Monovalent Copper Sulfide Clusters

Nanocrystals with a single targetable surface moiety are a valuable tool in biolabeling applications. These “monovalent” NCs (quantum dots in a biolabeling application) enable attachment of a single bio-active molecule and/or protein (i.e., Streptavidin) which can then be tracked through a cell by monitoring the fluorescence of the quantum dot.[208] Several post-synthesis processing strategies exist for monovalent QDs, including using gel electrophoresis to separate particles by the number of attached

species,[71] using special DNA molecules to completely encapsulate the QD,[74] and designing large ionic ligands that repel each other and prevent multivalent attachment.[73]

The goal of this project was to synthesize clusters of copper(I) sulfide that were morphologically unique in such a way that generated chemically targetable points on the cluster surface, as opposed to end-of-line NC processing like the methods referenced above, thereby advancing our understanding of surface chemistry and morphology control at the nanocluster scale. The idea for this project was sparked by the work of Brandi Cossairt's group and their investigation of InP nanomaterials. Gary, et al. published single crystal analysis of an InP cluster with an anisotropic morphology, and they observed the coordination of a single water molecule to one particular indium atom.[209] As noted by the authors, the implications of this observation were intriguing, because one may potentially use this site for controlled ligand adsorption. Gary, et al. have since followed this publication with an investigation into the attachment of amine ligands to this In site.[210]

Reading this work begged the question whether one could induce morphological anisotropy in clusters of other materials like copper(I) sulfide, a versatile semiconductor used as the parent material for many ternary and quaternary nanomaterials.[211] Work began with duplicating a synthesis developed by Dieter Fenske's group (specifically a publication by Bestgen, et al.[205]) to make copper sulfide clusters, with the ultimate goal of modifying this synthesis to induce changes to the morphology.

Initial results were positive replicating the work of Bestgen, et al., whose publication discussed the synthesis of the cluster $(Cu_2S)_{12}@[(CuSCH_2C_6H_4tBu)_{28}(PPh_3)_8]$ from a copper thiolate complex, triphenylphosphine and bis(trimethylsilyl)sulfide.[205] This synthesis was replicated in order to become familiar with cluster synthesis, crystallization,

and the subsequent characterization with single-crystal x-ray crystallography. With the help of Prof. Nathan Schley, the single crystal structure shown in Figure 5.9 was characterized based on this copper sulfide cluster synthesis.

Moving beyond this starting point, additional copper thiolate precursors were synthesized. These used 4-chlorobenzyl mercaptan and 4-tertbutylbenzene thiol in addition to Bestgen's 4-tertbutylbenzyl mercaptan to make Cu-thiolate precursor complexes (see Experimental Methods). Two large experiments were run in which these precursors were mixed in different ratios basing the procedure on the synthesis from Bestgen, et al. Unfortunately, when the cluster syntheses were being run prior to single-crystal analysis, it became apparent that the work involved to process the diffraction data would be logistically impractical. A crucial part of these experiments was identifying the terminal functional group of the surface ligand (Cl- or t-Bu-), as later on these could be used as handles to correlate precursor reactivity to cluster morphology control. When analyzing single-crystal data, uncertainty begins to compound as one moves outward from the core of the cluster, with much of the data processing time going to analyzing the ligand shell.

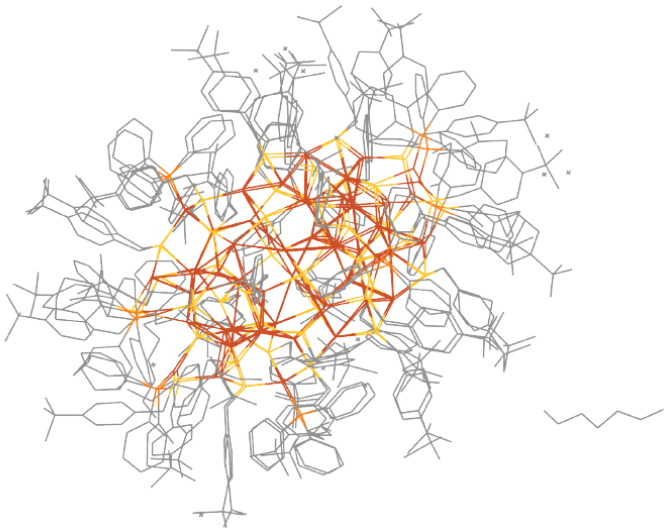

Figure 5.9. Copper sulfide cluster $(Cu_2S)_{12}@[(CuSCH_2C_6H_4tBu)_{28}(PPh_3)_8]$ single crystal structure determined with the help of Prof. Nathan Schley. The synthesis is a duplicate of the work by Bestgen, et al.

Prof. Schley processed the original data to generate the cluster unit cell shown in Figure 5.9, which had required several hours of work. Prof. Schley's crystallography data processing skills would be indispensable to this project, but in the long term this arrangement was unsustainable. With these logistical issues in mind and recognizing my own limitations with crystallography, it was decided to move on from this project. Going forward, the development of crystallographic analytical skills and skills with cluster crystallization would be crucial for this project.

5.2.1 Experimental Methods

Materials. 4-tertbutylbenzyl mercaptan (98.9%), 4-chlorobenzyl mercaptan, 4-tertbutylbenzenethiol (97%), ammonium hydroxide (28-30% solution), copper(II) sulfate pentahydrate, n-pentane (99%, anhydrous), n-heptane (99%, anhydrous), ethanol (200 proof, anhydrous), and bis(trimethylsilyl)sulfide, were obtained from Sigma Aldrich. Triphenylphosphine (99%) was obtained from Strem. Hydroxylamine hydrochloride (99%) was obtained from Alfa Aesar. All materials were used as received without additional purification.

Copper Thiolate Precursor Complex Synthesis. These syntheses were adapted from Nguyen, et al.[212] To a 100 mL three-necked flask, 20 mL deionized water and 5 mL NH_4OH were added, stirred and the flask was placed ice bath. 5 mmol $CuSO_4 \bullet 5H_2O$ was added to the flask, then 11.2 mmol $NH_2OH \bullet HCl$ was slowly added to the flask over 30 minutes. The ice bath was removed from the flask and the flask was sealed with a rubber septum. An Ar purge needle was inserted into the solution and the flask was vented. The flask was allowed

to mix until the solution turned colorless indicating the copper had been reduced to Cu(I) (approximately 3 hours). While the flask was purging, 25 mL anhydrous EtOH was added to a 50 mL flask. To this flask, 5 mmol of the thiol to be used in the cluster synthesis was added. Using air-free techniques, the thiol/EtOH solution was withdrawn into a 30 mL syringe and injected into the Cu-containing flask. The reaction was allowed to mix for five minutes, then the powder was washed in a Buchner funnel with deionized water, EtOH and Et_2O. The powder was dried under vacuum overnight and stored in a glovebox to prevent oxidation.

Copper Sulfide Cluster Synthesis. This synthesis was adapted from the work of Bestgen, et al.[205] 1.43 mmol of triphenylphosphine was added to a 50 mL round bottom flask and transferred into a glovebox. 1.85 mmol of the Cu-thiolate precursor complex was added, then 25 mL of anhydrous toluene was added and the contents of the flask were sonicated to break up the precursor powder. Then, while stirring, 0.38 mmol of bis(trimethylsilyl)sulfide was added to the flask. Over the course of five days the reaction was stirred in an Ar environment whereupon the color changed from a cloudy yellow to dark red. At this point, the toluene was removed by evaporation, and 35 mL of n-heptane was added to the flask and the solid dissolved. A portion of the dark red solution was centrifuged to remove any remaining solids, and the supernatant was transferred into a Schlenk tube where it remained for a period of three weeks. Small red crystals could be seen on the flask walls, which were washed in a glovebox with n-pentane. The crystals were transferred into Parabar in preparation for single-crystal analysis.

5.3 Charge Transfer Between Cobalt(III) Complexes and Quantum Dots

Charge transfer in nanocrystal systems is a concept that is essential to both foundational research and end-of-line applications. Successful transfer of an exciton from a photon-absorbing nanocrystal in a solar cell to a circuit, for example, is essential before the charges recombine and the usable energy is lost. Solar cell components must be carefully chosen to facilitate this charge transfer, and the same is true in photocatalytic applications. The project introduced here looked at charge transfer between fluorescent quantum dots and special cobalt complexes that possess vastly different reorganization energies/self-exchange rates.

This project began in the wake of publications by the Alivisatos group, in which hole transfer between fluorescent quantum dots and substituted ferrocene ligands that had a range of different oxidation potentials was investigated.[213,214] The authors made interesting observations about the rate of hole transfer under higher driving force conditions and noted that the system did not follow an inverted Marcus pattern, but instead

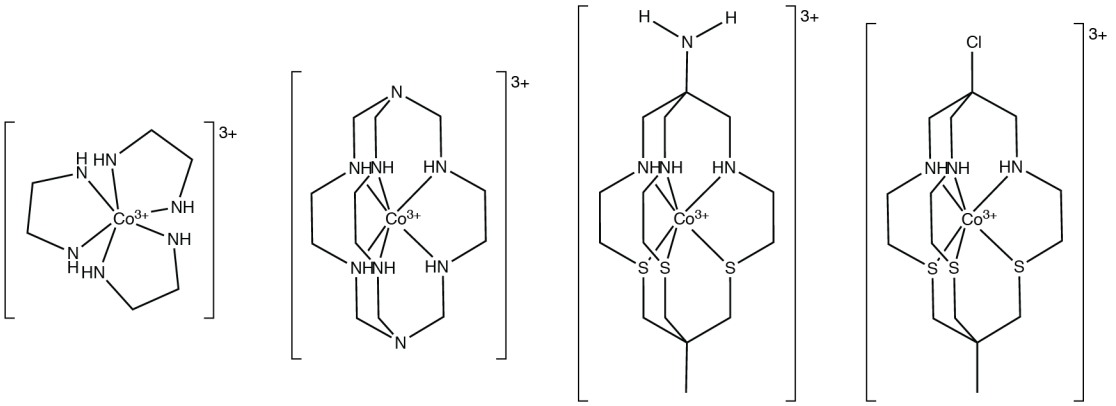

	$[Co(en)_3]^{3+}$	$[Co(sep)]^{3+}$	$[Co(NH_2MeN_3S_3sar)]^{3+}$	$[Co(ClMeN_3S_3sar)]^{3+}$
$E_{1/2}$ =	-0.13 V vs. NHE [a]	-0.26 [a]	-0.08 (pH 7) [c]	-0.01 (pH 7) [c]
SE rate =	$2.0 * 10^{-5}\ M^{-1}s^{-1}$ [b]	5.1 [b]	~10^4 [c]	~10^4 [c]

Figure 5.10. Cobalt (III)/(II) complexes with a broad range of self-exchange rates from the rate of $2.0 * 10^{-5}\ M^{-1}s^{-1}$ (tris(ethylenediamine) complex) to the rates of approximately $10^4\ M^{-1}s^{-1}$ (sarcophagine complexes). Values were obtained from Creaser, et al.,[a] Chou, et al.,[b] and He, et al.[c]

the rate of transfer stabilized after the initial increase (which they attributed to an Auger-assisted mechanism).[213]

This led Janet Macdonald and I to question to what degree the vastly different reorganization energies and self-exchange rates of Co(III)/(II) complexes might affect the charge transfer in that system. The cobalt complexes depicted in Figure 5.10 possess a considerable range of self-exchange rates from 2.0 * 10^{-5} $M^{-1}s^{-1}$ to approximately 10^4 $M^{-1}s^{-1}$,[215,216] and have a 250 mV range of redox potentials (vs. NHE).[216,217] It was hoped that for the purposes of the investigation into the effect of self-exchange rate on charge transfer, the driving force potentials would be in a sufficiently narrow range to compare these complexes to one another.

Tris(ethylenediamine)cobalt(III) chloride is commercially available, however the other three complexes in Figure 5.10 needed to be acquired through other means. Fortunately, Prof. Paul Bernhardt (University of Queensland) was willing to provide the two N_3S_3 sarcophagine (sar) complexed species,[218] and a synthesis for the sepulchrate (sep) complex existed in the literature (see Experimental Methods).[219]

Designing the charge transfer experiment was complicated due to the sheer number of different ways in which it could be orchestrated. The choice between an aqueous or organic environment would dictate the surface chemistry of the QDs and complexes, and deciding between either hole or electron transfer would dictate whether the experiment could be run in air and how the Co complexes were prepared.

In short, it was ultimately decided to pursue electron transfer from QDs to Co(III) complexes in an aqueous environment, but this was decided after months of attempting to prepare Co(II) complexes (for hole transfer) in both aqueous and organic solvents. As noted

by Olshansky, et al., hole transfer has less of a presence in the literature, even though it is an important efficiency-limiting process in some QD-sensitized solar cells and hydrogen production applications.[213] A hole transfer experiment would require the preparation of reduced Co species, which could be accomplished through a number of routes.

Historically, reduction of Co(III) complexes to Co(II) used Hg alloys (amalgams) with other elements like Zn.[215,220] Co(II) complexes have also been prepared electrochemically (though with a Hg electrode).[221] A safer option is to simply use Zn dust[220] to reduce the Co(III) complexes, which was found here to reduce the Co complexes indicated by the color change from brown to [nearly] colorless.[221] The resulting solution had a pink coloration which could be due to hydrated Co^{2+}, which could have ultimately interfered with spectroscopic analysis and made this route problematic. Electrochemical reduction was also attempted, and with greater success given the resulting Co(II) solution was completely colorless post-reduction. However, it was found that the Co(II) solutions were extremely susceptible to oxidation (even in a glovebox set up specifically for this purpose) and would chemically change to species with significantly higher molar absorptivity upon exposure to air. Thus, due to the high probability of a non-zero amount of oxidation, and the subsequent lack of reproducibility that would cause, it was decided to pursue electron transfer of QDs to Co(III) species.

The decision to run the charge transfer experiments in water came after synthesizing core/shell quantum dots[222] that experienced a significant drop in PLQY after attempting to transfer the QDs into water with a ligand exchange. High-PLQY water soluble QDs were purchased from Sigma Aldrich. Co(III) complexes were made soluble in organic solvents (tetrahydrofuran) through counter-ion exchange with tetraphenylborate

salts,[223] but after the water soluble QDs were acquired pursuing charge transfer in organic solvents was halted. This could be resumed in the future to investigate the effects of solvent on the reorganization of the cobalt complexes in question.

It was hypothesized that complexes with the faster self-exchange rates would accept charge from the QDs faster than those complexes with slower rates with evidence being seen in fluorescence quenching. Indeed this was the case as seen in Figure 5.11, as the $[Co(III)(sep)_3]^{3+}$ complex has a self-exchange rate over five orders of magnitude faster than the $[Co(III)(en)_3]^{3+}$ complex. However, when an excessive amount of the $[Co(III)(en)_3]^{3+}$ was added (data not shown), the fluorescence signal did in fact begin to quench, though the intensity would change with time, rather dramatically, implying an equilibrium had not yet been reached. This fact meant that the experiment needed to be redesigned to further control the variables of Co-complex solution addition and temporal fluorescence variability.

Due to the precedence of other projects this work was put on hold temporarily, but Madeline Fort has since continued this investigation with a new and improved iteration of the charge transfer experiment.

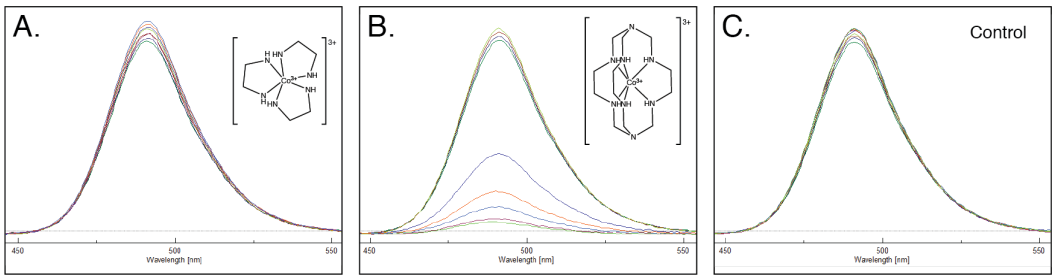

Figure 5.11. QD fluorescence measurements (ex. 348 nm). Initially, four measurements were taken every 30 minutes to establish that the fluorescence was stable. Then, in A and B, three 10 µL injections and one 50 µL injection of Co(III) complex (80 µM) are added. In C, the control sample, nothing is added and fluorescence measurements are taken at the same time intervals as the samples in A and B.

5.3.1 Experimental Methods

Materials. Formaldehyde (37%), ammonium hydroxide (28-30%, ACS Reagent), lithium carbonate, sodium diethyldithiocarbamate trihydrate (>98%), tris(ethylenediamine)cobalt(III) chloride dihydrate, mercaptoacetic acid, CdSeS/ZnSe alloyed quantum dots (Sigma 754226, carboxylic acid functionalized, 1 mg/mL, emission wavelength 490 nm) were obtained from Sigma Aldrich. All materials were used as received without additional purification.

Synthesis of cobalt(III) sepulchrate. This synthesis was modified from the work of Gahan, et al.[219] Li_2CO_3 (1.15g, 15.6 mmol) and 1.3 mmol $[Co(en)_3]Cl_3$ were placed in a 100 mL round-bottom flask with 10 mL of deionized water and stirred. 7 mL of NH_4OH was diluted to 25 mL with deionized water and added to a syringe. 25 mL of aqueous formaldehyde was also added to a syringe, and both syringes were placed in automatic syringe injectors. The injection program was set to take place over 1 hour. At that time, the reaction was allowed to stir for an additional 20 minutes. The post reaction mixture was filtered to remove Li_2CO_3, and 1.25 g $Na[S_2CNEt_2]\bullet 3H_2O$ (in 25 mL deionized water) was added to the reaction mixture and stirred for 30 minutes. The opaque red mixture was centrifuged, and the recovered red powder ($[Co(sep)][S_2CNEt_2]_3$) was vortexed and centrifuged in an 80:20 mixture of hexanes:dichloromethane three times and dried under vacuum. 250 mg of this product was placed in 5 mL of acetonitrile and sonicated; to this mixture 250 µL of concentrated HCl was added and stirred for 10 minutes. The resulting orange powder was mixed with acetonitrile and centrifuged four times until the supernatant was colorless. The powder was then dissolved in a minimal amount of water and allowed

to crystallize in air over three days. The resulting red crystalline material was analyzed by ^{1}H NMR in D_2O with signals matching the analysis of Creaser, et al.[220] See Appendix A1 for NMR spectrum.

Fluorescence Quenching of QDs with Co(III) Complexes. The quantum dots obtained from Sigma Aldrich were diluted to a concentration of 30 μM in a solution of 169 μM mercaptoacetic acid (MAA) in deionized water, which equated to approximately 50 additional ligands/nm^2. Separately, solutions of Co-complexes were prepared at 80 μM using deionized water. Prior to the experiment, quartz cuvettes were cleaned in a base bath overnight and thoroughly rinsed with deionized water. Into four clean cuvettes 2.5 mL of the quantum dot/MAA solution was added with a clean stirbar. The cuvettes were capped, stirred at 700 rpm, and analyzed using UV-Vis and fluorescence spectrophotometry (ex. 348 nm) every 30 minutes for two hours to establish that the emission and colloidal suspensions were stable. Following this step, 10 μL doses of the Co-complex solutions were added to each cuvette using a volumetric pipet approximately every 25 minutes. Following each addition, the sample would be stirred for 60 seconds, then analyzed on a fluorimeter, and finally on a UV-Vis spectrophotometer. After the three additions, one 50 μL addition of the Co-complex solution was added.

Instrumentation. Solution absorption spectra were obtained on a Jasco V-670 UV-Vis-NIR spectrophotometer in deionized water. Fluorescence spectra were acquired using a Jasco FP-3800 spectrofluorometer. ^{1}H NMR spectra were taken using a Bruker DRX-400

(tuned to 400 MHz) spectrometer. Spectra were calibrated to residual solvent signals of 4.79 ppm in D_2O.

Chapter 6

CONCLUSION

6.1 Summary

The work presented here discussed the control of crystal structure and morphology of copper(I) chalcogenide nanocrystals. In addition, the techniques developed with $Cu_{2-x}Se$ in Chapter 3 were applied to other semiconductor nanocrystals and the groundwork was laid for a charge transfer investigation involving Co(III) complexes.

Chapter 2 covered the oriented attachment of Cu_2S nanocrystals with crystal-bound ligands through the use of 1,2-hexadecanediol as a surface stabilizer. After Michael Turo had observed the oriented attachment phenomenon in an Ru-shelling experiment, I was tasked with reproducing this result and characterizing the nanorod system. I found that the HDD was crucial to facilitating the attachment process, and the reaction temperature needed to be sufficient to destabilize the crystal-bound ligands on the higher-energy NC facets. XRD analysis showed that the fully stoichiometric Cu_2S crystal structure was maintained from the seed precursors to the final product, which was further supported by the lack of a plasmon in the UV-Vis absorbance spectrum of the colloidal nanorods.

HDD is typically used as a reducing agent in NC syntheses, though in this case it was found to act as a loosely-bound ligand species. When too much or too little HDD was used the effects were problematic, with the ideal amount being approximately 50 molecules per nm^2 of NC surface area. Based on an aliquot study, the oriented attachment process took place continuously over the course of the hour at 220 ˚C. Early aliquots showed the NCs aligning with one another into short chains of particles, and later fully formed

nanorods would appear. Nearing the end of the hourlong reaction, nanorods that had formed early on would show signs of Ostwald ripening, so the process would be halted.

Ultimately, this project resulted in a viable Cu_2S nanorod synthesis that could be suitable for cation exchange to the ternary copper sulfides, and it joins the handful of instances in which oriented attachment has been observed and controlled at the nanoscale.

Chapter 3 discussed our discovery and development of a direct synthesis for wurtzite $Cu_{2-x}Se$. One fortuitous aliquot early on resulted in our discovery of the wurtzite phase with our ligand system (Figure 6.1). Ultimately, using a diselenide precursor, we were able to synthesize nanodisks of $Cu_{2-x}Se$ that had the metastable hexagonal crystal structure which had only been seen once previously by Gariano, et al.[106] The thermodynamic cubic phase of $Cu_{2-x}Se$ was synthesized through the use of a selenol precursor.

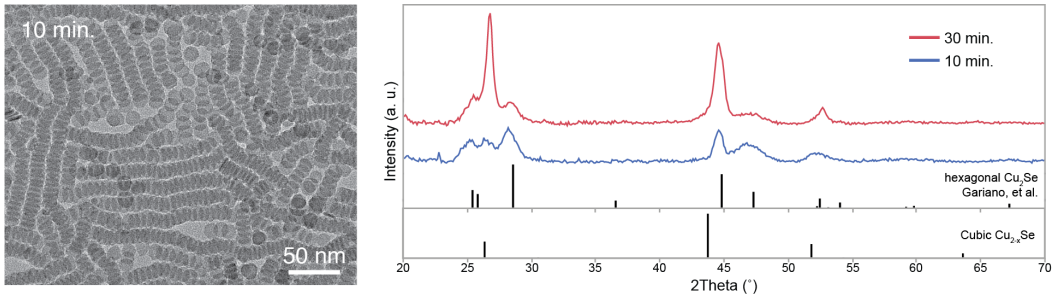

Figure 6.1. TEM and XRD of an early $Cu_{2-x}Se$ synthesis in which an aliquot I took showed something other than the cubic crystal structure we were expecting. Here, the XRD pattern is compared to the Gariano, et al. reference pattern about which we would later become aware. The 10-minute aliquot (and even the 30-minute sample) seems to be a mixture of the hexagonal and cubic phases. Subsequent optimization of the synthesis would yield better phase control. The TEM images of the nanodisks were also promising due to the particle monodispersity. Cubic reference pattern ICSD: 181661.

Chapter 3 includes characterization of the NCs that revealed the formation of a plasmon in the NIR upon exposure to air, but that the hexagonal phase was stable for at least three weeks after synthesis (as characterized with XRD). A phase change to the thermodynamic cubic crystal structure could be induced at higher temperatures, and variable temperature XRD was used to that end. Particle sintering was identified as the

likely cause of phase change from the hexagonal phase to the cubic phase, as the change was irreversible.

Trends in the literature had shown previously that organoselenide precursors with lower C-Se bond-dissociation energy (BDE) values led to the formation of the thermodynamic phase in polymorphic systems, while precursors with higher BDE lead to metastable phases.[153] The results in Chapter 3 follow this trend despite the counterintuitive fact that the selenol has a higher BDE than the diselenide. The selenol (like primary thiols) reacts with Cu precursors to form a copper selenoate complex that actually breaks down faster and at lower temperatures than the diselenide, and this leads to formation of the thermodynamically stable phase. The diselenide reacts more slowly, and this results in the metastable hexagonal phase.

The next logical step from studies involving diselenides/selenols was to investigate ditellurides/tellurols and $Cu_{2-x}Te$. Chapter 4 highlights the unpublished results of an investigation into the relative newcomer to the copper(I) chalcogenide nanocrystal scene. Attempts were made to synthesize a tellurol in order to do a proper study analogous to the investigation in Chapter 3, but the tellurol proved to be too unstable. Results with didodecyl ditelluride, while interesting on their own, primarily yielded the metastable pseudo-cubic phase $Cu_{1.5}Te$ which had previously been characterized.[170] Syntheses in coordinating solvents like OlAm and OA resulted in cubes of that crystal structure. High temperature syntheses and reactions in non-coordinating solvents yielded nanosheets of what was indexed to CuTe (Vulcanite). The possibility of Vulcanite nanosheets was interesting in that they had not been synthesized solvothermally; only through electrochemistry had "nanoribbons" of Vulcanite been previously synthesized.[195]

Chapter 5 discussed the use of the selenol NC precursor from Chapter 3 to synthesize nanocrystals of known phases of ZnSe, PbSe, Ni_xSe, Ag_2Se and CdSe. Zinc blende ZnSe NCs were synthesized with a selenol precursor that showed variation in emission wavelength based on reaction time. PbSe NCs of the known Clausthalite (rock salt) crystal structure were synthesized with the selenol precursor, as well as Ni_xSe NCs of the hexagonal Sederholmite phase. Cluster-like particles of Ni_xSe were also synthesized but proved difficult to characterize with XRD and TEM. Both the selenol and diselenide were used to synthesize Ag_2Se NCs, however both sets of experiments resulted in the metastable tetragonal phase identified by Sahu, et al. in 2011.[207] Lastly, CdSe was investigated though the ZB phase resulted from both precursors.

Chapter 5 contains additional work done on Cu_2S clusters that were synthesized in an attempt to make monovalent nanocrystals. The work was inspired by the InP NC publications by Dylan C. Gary of Brandi Cossairt's group,[209,210] and the experimental syntheses were adapted from a publication by Bestgen, et al.,[205] whose cluster ($(Cu_2S)_{12}@[(CuSCH_2C_6H_4tBu)_{28}(PPh_3)_8]$) was synthesized and characterized using single-crystal x-ray crystallography with the help of Prof. Nathan Schley. A second experiment designed to analyze the cluster surface chemistry when different ligand species were used was in progress when the project was halted. This was due to the unsustainable amount of time required on Prof. Schley's part to process the crystallography data.

Lastly, Chapter 5 concludes with a charge transfer project that was inspired by publications from the Alivisatos group,[213,214] and the fact that certain cobalt complexes possess radically different self-exchange rates and reorganization energies. The investigation would determine if the self-exchange rates of four Co(III)/(II) complexes

ranging from 2.0 * 10^{-5} $M^{-1}s^{-1}$ to approximately 10^4 $M^{-1}s^{-1}$,[215,216] would have an effect on QD fluorescence. Preparing Co(II) complexes in aqueous and organic media was investigated for the purposes of a hole transfer experiment, but ultimately Co(III) electron transfer in an aqueous environment was settled upon. QD fluorescence quenched appreciably in the presence of Co(III)(sep) in comparison to $Co(III)(en)_3$ which correlated with their respective self-exchange rates. However, it was determined that there were significant time-dependent fluctuations in QD fluorescence quenching, and the experiment needed to be redesigned to account for those effects.

6.2 On Phase and Morphological Control of the Copper Chalcogenides

The copper chalcogenide family of nanomaterials offers much to the materials chemist, notably as a platform for cation exchange to make various ternary and quaternary semiconductor nanocrystals. Additionally, $Cu_{2-x}S$, $Cu_{2-x}Se$ and $Cu_{2-x}Te$ NCs share a number of different chemical and electronic attributes, namely their predisposition to oxidation-induced development of plasmonic absorption features, which allow the position and intensity of plasmonic absorbance to be tuned (primarily in $Cu_{2-x}S$ and $Cu_{2-x}Se$) through prescribed air exposure.[143] Also, the copper chalcogenides present a collection of facile NC syntheses through which the fundamentals of nanomaterials chemistry can be explored. It is with this last concept in mind that the unique surface chemistry and crystal structures of this family of materials and their effects on NC phase and morphology control were investigated in the works presented here.

The synthesis of Cu_2S is quite unique in that one can synthesize monodisperse NCs with a copper source (for example, $Cu(acac)_2$) and dodecanethiol (the sulfur source, ligand

and reaction solvent), without the need for additional precursor materials. This synthesis reaction is particularly noteworthy due to the confluence of factors at the reaction temperature, including: precursor decomposition, NC nucleation, and the stability of the surface chemistry during synthesis. The thiol reacts with the Cu precursor forming Cu-thiolate complexes that break down, rearrange, and decompose at increasing temperatures. Monodisperse nanocrystals then nucleate and grow slowly (making the need for hot-injection unnecessary), and the nanocrystals possess the unique crystal-bound ligand surface chemistry first described by Turo, et al.[62]

Moving to the more-reactive $Cu_{2-x}Se$ synthesis, one can still produce monodisperse nanocrystals without the need for additional coordinating ligands and at significantly lower temperatures (155 ˚C as opposed to 200 or 215 ˚C for Cu_2S). In this case, the surface chemistry provided by the diselenide (or one of its currently unidentified decomposition products) is sufficient to keep the particles stable up to 175 ˚C. Though in the absence of an excess of DD_2Se_2, the NCs were shown to sinter together at 150 ˚C. In a selenol-based synthesis, Cu-selenoate complexes form similar to the Cu-thiolate complexes mentioned above, though in the Cu-selenoate case their high reactivity (faster decomposition) relative to the diselenide leads to the thermodynamic cubic phase.

With that being said, the syntheses for $Cu_{2-x}Te$ NCs grown with a ditelluride analogue proved to be much more reactive than the Se counterpart. This was unsurprising considering the substantially lower C-Te BDE values (shown in Ch. 5). In this case, the precursor decomposition and nucleation temperatures, as well as the NC growth rate and surface chemistry stability did not align beneficially, to the detriment of the NC product. Frequently observed in syntheses of $Cu_{2-x}Te$ NCs, very small quantities of large crystals

would be present in the post reaction mixtures, implying that the rate of precursor decomposition did not correlate with the relatively fast rate of NC growth (possibly due to a lack of surface stability). In this case, to achieve monodisperse particles similar to those obtained with Cu_2S and $Cu_{2-x}Se$ a coordinating solvent like oleylamine or oleic acid needed to be added to control growth and prevent agglomeration.

The phase of these materials was crucial to understanding the growth of the obtained nanocrystals and ultimately the morphologies that resulted. The anisotropic chalcocite crystal structures of Cu_2S contain S atoms that are arranged in hexagonal layers, and in order to maintain charge balance, the terminal facets along that c-axis are either sulfur- or copper-rich. The dipole that this atomic configuration produces was responsible for the inter-particle attraction and oriented attachment phenomenon seen in Ch. 2. The wurtzite phase of $Cu_{2-x}Se$ is also anisotropic and layered, which may also enable oriented attachment at a suitable temperature and in the presence of 1,2-hexadecanediol or a similar species.

Morphologically, the quasi-spherical Cu_2S seeds in Ch. 2 were shown to be susceptible to the presence of OlAm at higher temperatures, which favored the terminal (c-axis) facets of the NCs resulting in platelet-like NCs. It has been shown previously that OlAm binds strongly to Cu,[128] and in the case reported here the ripening was only seen in the dimensions lateral to the terminal facets in question. Interestingly, the $Cu_{2-x}Se$ NCs of Ch. 3 were naturally platelet-like without the need for additional coordinating solvents, implying fast growth along the (100)- and (110)-type facets which (qualitatively) must not be as stable in the presence of the diselenide (or its decomposition products), which enables fast adsorption of monomer units (i.e., nanocrystal growth).

It is interesting that the $Cu_{2-x}Te$ favors a substoichiometric phase closer to x=0.5 when a Cu:Te ratio similar to the $Cu_{2-x}Se$ NC synthesis was used. $Cu_{2-x}Te$ is known for its ionic conductivity,[148] and the mobility of the Cu ions at elevated temperature could account for the inability of the crystal lattice to retain those ions. In unpublished work, I observed the formation of a plasmonic absorbance feature in smaller (6-10 nm) $Cu_{2-x}S$ NCs when left at the synthesis reaction temperature for extended time intervals—implying copper loss in an inert environment. This is relevant here because Cu_2S is comparatively less-susceptible to Cu loss through oxidation, at least in comparison to $Cu_{2-x}Se$. It is this loss of Cu in $Cu_{2-x}Te$ which could account for the formation of the substoichiometric Vulcanite phase (CuTe) seen at higher temperatures. (Note that a report on controlled oxidation of the copper chalcogenides by Kriegel, et al.[143] wrote that $Cu_{2-x}Te$ did not show susceptibility to oxidation as it *already was* in a plasmonic substoichiometric phase post-synthesis)

This tendency for $Cu_{2-x}Te$ to favor stoichiometries with *lower* Cu content enables access to the unique nanosheet morphology (possible with Vulcanite CuTe) which was not seen in the Cu_2S or $Cu_{2-x}Se$ cases. Covellite (CuS) and Klockmannite (CuSe) are analogous crystal structures to one another,[224,225] with a layered structure that could potentially be exploited to make nanosheets of the other copper chalcogenides. However, the relative stability of the Cu_2S and $Cu_{2-x}Se$ phases at higher Cu:S/Se ratios, and the comparatively lower reactivity in comparison of $Cu_{2-x}Te$, precludes the formation of nanosheets of those materials in the works presented here.

Ultimately, the copper chalcogenides offer fertile ground for exploration of the fundamentals of nanomaterials chemistry. Due to their diverse families of polymorphic

crystal structures at a range of stoichiometries, the copper chalcogenides were an ideal candidate for investigating phase and morphology control.

6.3 Future Directions

Much of the work discussed in this thesis has led to or contributed to projects that are currently being executed. The nanorods in Chapter 2 have been used by Christopher Sharp, of the Macdonald lab, for cation exchange to $CuFeS_2$. Additionally, work has been done to synthesize Cu_2S from quantum confined seed nanocrystals, but it was found that the rods quickly ripen beyond the limits of confinement in that material (~5 nm Bohr radius[109]). It may be possible to accomplish this goal using additional ligand species that stabilize the lateral facets of the narrower rods.

The $Cu_{2-x}Se$ NCs discussed in Chapter 3 are an exciting prospect for cation exchange, as the copper(I) chalcogenides are known for being viable parent materials for ternary and quaternary semiconductor NCs.[169,226,227] Christopher Sharp is currently investigating or plans to investigate cation exchange with a number of 3+ cations. Dr. Emil Hernandez has also investigated cation exchange with these NCs at the University of Pennsylvania. The wurtzite phase of $Cu_{2-x}Se$ is still relatively new, and very little is known about its properties. This opens the possibilities for a number of investigations into the optical and electronic properties of this material.

The $Cu_{2-x}Te$ nanocrystal syntheses in Chapter 4 need to be optimized to achieve phase-pure results prior to publication. The possibility of Vulcanite (CuTe) nanosheets is unique as they have not been reported in the literature, but the XRD analysis of these products indicates the presence of other impurities, namely elemental Te and to a lesser

degree Rickardite ($Cu_{1.4}Te$) and pseudo-cubic $Cu_{1.5}Te$. Manipulation of the Cu:Te ratio could prevent the unwanted nucleation of excess elemental Te in the reaction. In-plane XRD analysis should have revealed the crystal structure of planar materials parallel to the substrate surface, but the results were inconclusive. According to the instrument manufacturer, a more-sensitive X-ray detector could be used for this experiment to better detect signals from the material.

Going forward, the materials investigated in Chapter 5 can be synthesized with the diselenide precursor. As discussed in Chapter 3, the diselenide produced the metastable phase of $Cu_{2-x}Se$ due to its comparatively low reactivity. There are a number of materials discussed in Chapter 5 for which the diselenide was not used as a precursor, so the opportunities exist to pursue further phase control with our ligand system. Also discussed in Chapter 5, the charge transfer experiment is currently being investigated by Madeline Fort. The second iteration of the fluorescence quenching study has been designed to accommodate the equilibrium effects that were seen in the initial experiments. This has been accomplished through the use of a fluorimeter that is capable of continuously monitoring the fluorescence of the QDs, while the Co complex solutions are continuously added via a syringe injector. A collaborator at Emory (Wenxing Yang of Tianquan Lian's group) is performing transient absorption analysis to complement this investigation.

6.4 Outlook

The field of nanocrystal chemistry continues to grow, with promising end-of-line applications becoming a reality. With the inclusion of fluorescent quantum dots in commercially available televisions, the advantageous characteristics of these materials are

already reaching the broader public. That being said, to me the most important potential applications of semiconductor nanomaterials are their integration into devices that use solar energy for the purposes of photocatalysis or photovoltaics electricity production.

When I was at the University of Oregon studying semiconductor device processing, one of the concepts that was made clear to me was how difficult it is to produce a boule of pure silicon. Semiconductor nanocrystals, on the other hand, can be synthesized cheaply with simple equipment. This makes them attractive device components at the bench scale, but much work needs to be done to compete with the existing infrastructure that the semiconductor industry has. I am interested to see which industries choose to buy in to nanocrystal technologies for their applications in the future, and to what degree nanocrystals will play a role in our daily lives.

As stated in the introduction, humankind has had a marked effect on the planet and halting manmade climate change should be at the forefront of everyone's minds. As a scientist, it is my hope that emerging technologies like nanocrystals will contribute to greener energy production as soon as possible.

APPENDIX

A. Additional Images

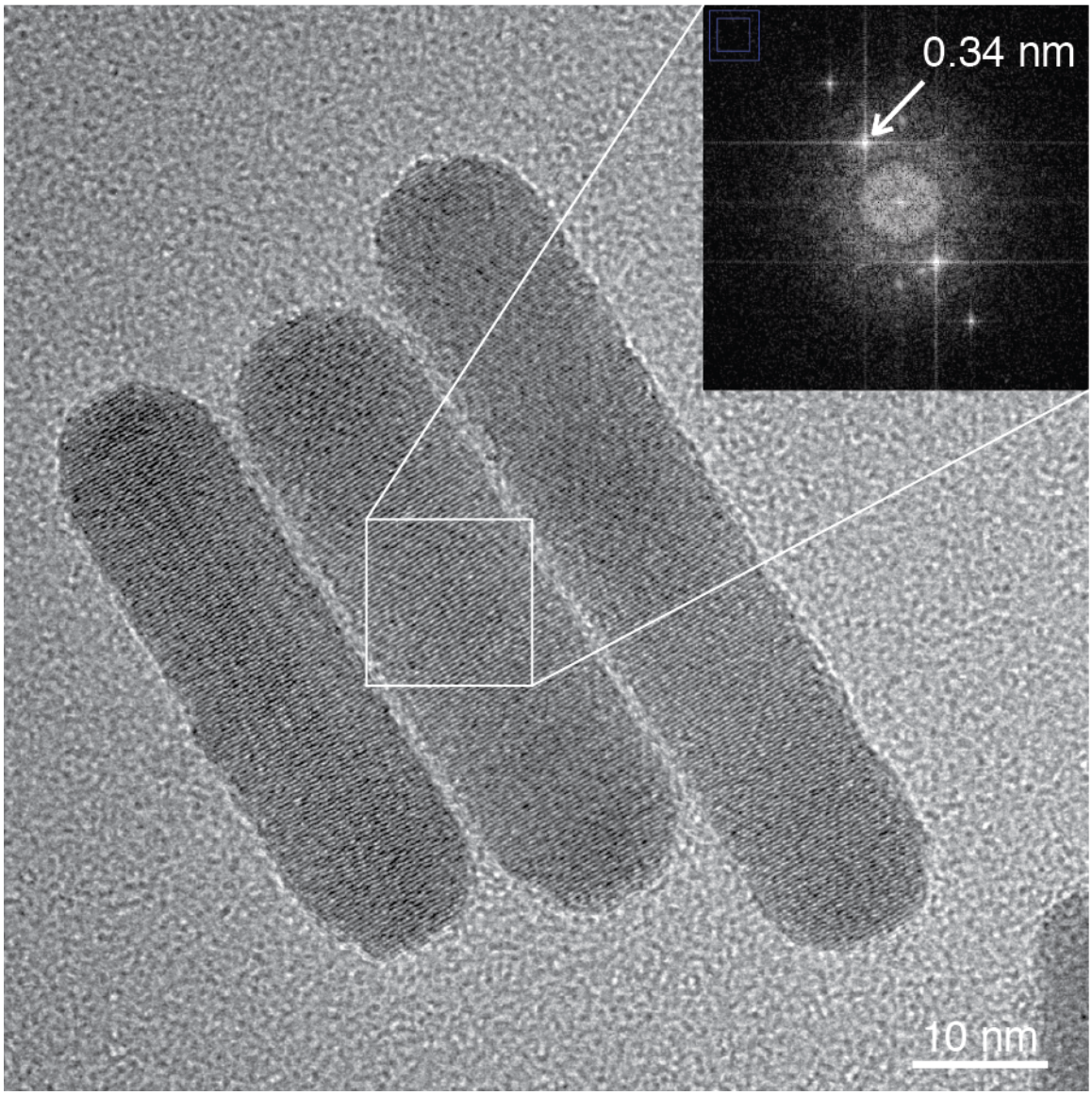

Figure A2.1. HRTEM image of the final Cu_2S nanorod product and FFT of d-spacings correlate to the c-axis (002) plane of high chalcocite (JCPDS 26-1116). Comparing this image to the peapods shown in Figures 2.3 and 2.4 show that the lateral facets have smoothened over resulting in a homogenization of the surface chemistry. Reprinted with permission from Robinson, E. H., et al. *Chem. Mater.* **2017**, *29* (9), 3854. Copyright 2017 American Chemical Society.

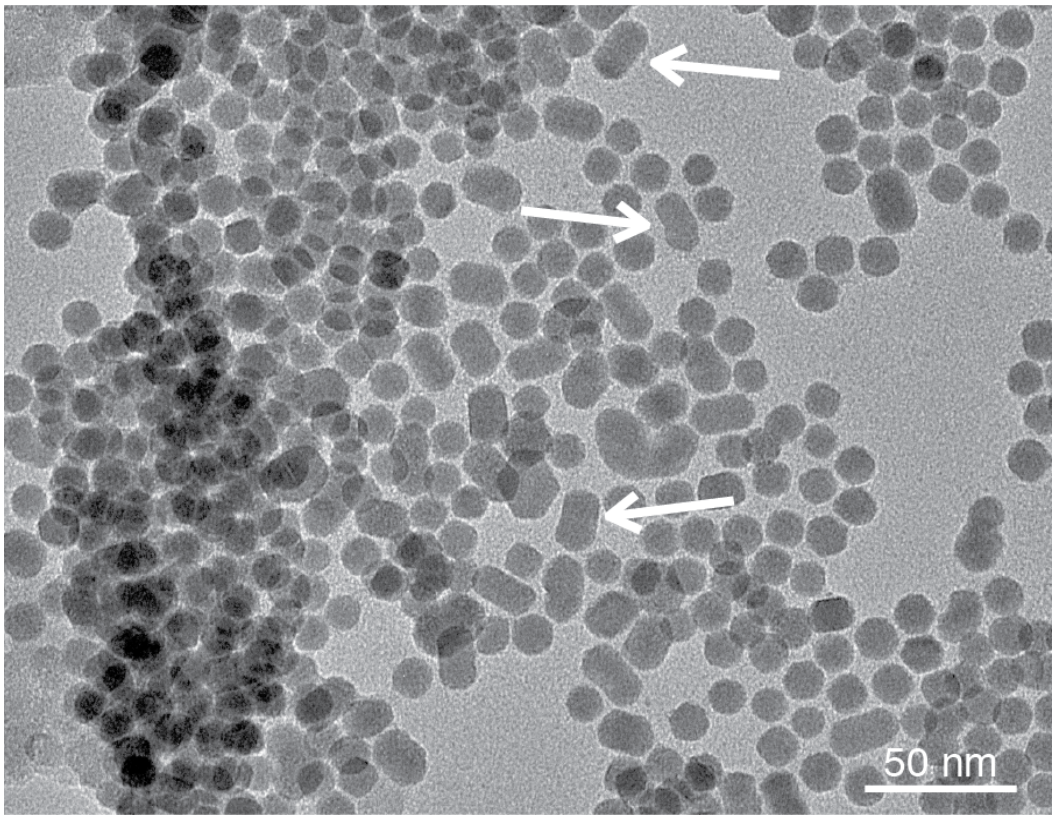

Figure A2.2. TEM image of short, two-particle nanorods (dimers) seen when low concentrations of nanocrystal seeds are used. Solitary nanocrystals comprise the majority of what is seen here, indicating that the nanocrystals are too sparse to interact in the reaction vessel. Increasing the seed concentration increases the probability of attachment. Reprinted with permission from Robinson, E. H., et al. *Chem. Mater.* **2017**, *29* (9), 3854. Copyright 2017 American Chemical Society.

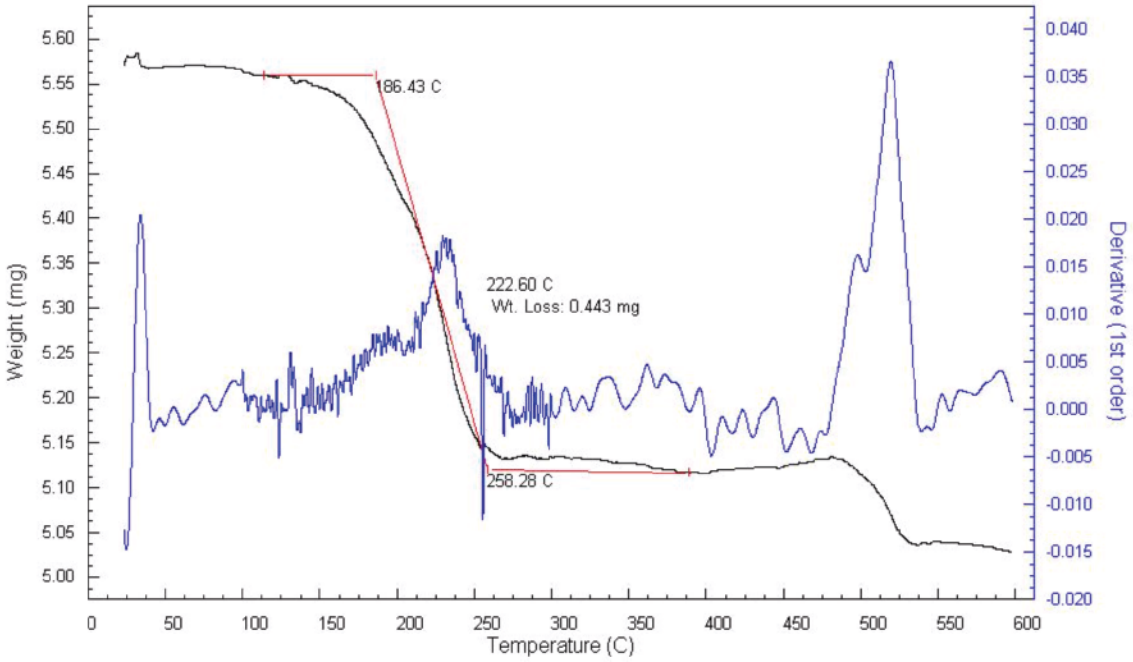

Figure A2.3. TGA of Cu_2S seed nanocrystals with crystal-bound 1-dodecanethiol ligands, showing a loss of organics. The trace of the first derivative is shown in blue. Reprinted with permission from Robinson, E. H., et al. *Chem. Mater.* **2017**, *29* (9), 3854. Copyright 2017 American Chemical Society.

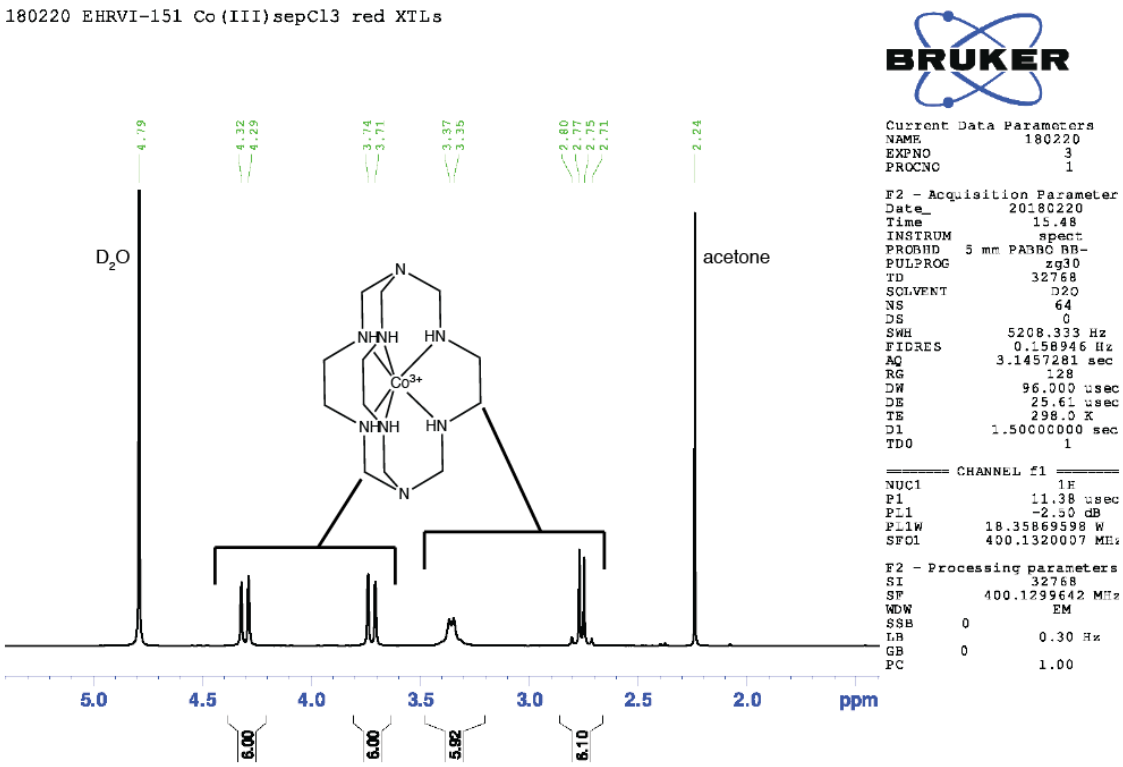

A6.1. ^{1}H NMR (400 MHz) spectrum of cobalt(III) sepulchrate trichloride in D_2O

B. Adapted Publications

Parts of this dissertation have been published previously, copyright approval has been obtained for reproduced figures or text in the following chapters:

Chapter II

Reprinted with permission from Robinson, E. H.; Turo, M. J.; Macdonald, J. E. *Chem. Mater.* **2017**, *29* (9), 3854. Copyright 2017 American Chemical Society.

Chapter III

Reprinted with permission from Hernández-Pagán, E. A.; Robinson, E. H.; La Croix, A. D.; Macdonald, J. E. *Chem. Mater.* **2019**, *31* (12), 4619. Copyright 2019 American Chemical Society.

First authorship is shared with E. A. Hernández-Pagán and his permission was granted to publish this work herein. EHR was responsible for initial synthesis of WZ phase (see Ch. 6), selenol-based syntheses, NC stability experiments, NC syntheses at varying temperatures, precursor aliquot study and making figures. EHP was responsible for directing both the scope of this project and organizing the text of the publication, as well as designing and optimizing the diselenide-based NC synthesis and UV-Vis-NIR spectroscopy. EHR and EHP contributed equally to the variable temperature XRD experiments and executing TEM characterization. ADLC was responsible for the synthesis of organic precursors (selenols and diselenides).

Chapter IV

Robinson, E. H.; Dwyer, K. M.; Nuriye, A. Y.; Macdonald, J. E. *In Preparation.*

Chapter V: Charge Transfer

Fort, M. J.; Robinson, E. H.; Yang, W.; Bernhardt, P.; Lian, T.; Macdonald, J. E. *In Preparation.*

REFERENCES

(1) Ainsworth, E. A.; Rogers, A. *Plant, Cell Environ.* **2007**, *30* (3), 258.

(2) U.S. Energy Information Administration. *Annual Energy Outlook*; 2018.

(3) U.N. Intergovernmental Panel on Climate Change. *IPCC Special Report on the Impacts of Global Warming of 1.5 °C*; 2018.

(4) Obama, B. *Science* **2017**, *355* (6321), 126.

(5) Lazard. *Lazard's Levelized Cost of Energy - Ver. 11.0*; 2017.

(6) Luther, J. M.; Gao, J.; Lloyd, M. T.; Semonin, O. E.; Beard, M. C.; Nozik, A. J. *Adv. Mater.* **2010**, *22* (33), 3704.

(7) Lan, X.; Voznyy, O.; García De Arquer, F. P.; Liu, M.; Xu, J.; Proppe, A. H.; Walters, G.; Fan, F.; Tan, H.; Liu, M.; Yang, Z.; Hoogland, S.; Sargent, E. H. *Nano Lett.* **2016**, *16* (7), 4630.

(8) Sanehira, E. M.; Marshall, A. R.; Christians, J. A.; Harvey, S. P.; Ciesielski, P. N.; Wheeler, L. M.; Schulz, P.; Lin, L. Y.; Beard, M. C.; Luther, J. M. *Sci. Adv.* **2017**, *3* (10).

(9) Wenham, S. R.; Green, M. A. *Prog. Photovoltaics Res. Appl.* **1996**, *4*, 3.

(10) Bowers, M. J.; McBride, J. R.; Garrett, M. D.; Sammons, J. A.; Dukes, A. D.; Schreuder, M. A.; Watt, T. L.; Lupini, A. R.; Pennycook, S. J.; Rosenthal, S. J. *J. Am. Chem. Soc.* **2009**, *131* (16), 5730.

(11) Liao, L.; Zhang, Q.; Su, Z.; Zhao, Z.; Wang, Y.; Li, Y.; Lu, X.; Wei, D.; Feng, G.; Yu, Q.; Cai, X.; Zhao, J.; Ren, Z.; Fang, H.; Robles-Hernandez, F.; Baldelli, S.; Bao, J. *Nat. Nanotechnol.* **2014**, *9* (1), 69.

(12) Tian, B.; Lei, Q.; Zhang, W.; Cui, Y.; Tian, Y.; Tian, B. *Chem. Commun.* **2018**, *54* (15), 1845.

(13) Moriarty, P. *Reports Prog. Phys.* **2001**, *64*, 297.

(14) Moreau, L. M.; Ha, D. H.; Zhang, H.; Hovden, R.; Muller, D. A.; Robinson, R. D. *Chem. Mater.* **2013**, *25* (12), 2394.

(15) Crucho, C. I. C.; Barros, M. T. *Mater. Sci. Eng. C* **2017**, *80*, 771.

(16) Barber, D. J.; Freestone, I. C. *Archaeometry* **1990**, *32* (1), 33.

(17) Ghosh, S.; Zandi, O.; Cho, S. H.; Milliron, D. J.; Johns, R. W.; Agrawal, A. *Chem. Rev.* **2018**, *118* (6), 3121.

(18) Anker, J. N.; Hall, W. P.; Lyandres, O.; Shah, N. C.; Zhao, J.; Van Duyne, R. P. *Nat. Mater.* **2008**, *7* (6), 442.

(19) Faraday, M. *Spie Milestone Ser. Ms* **1996**, *120*, 9.

(20) Brus, L. E. *J. Chem. Phys.* **1983**, *79* (1983), 5566.

(21) Brus, L. E. *J. Chem. Phys.* **1984**, *80* (1984), 4403.

(22) Thanh, N. T. K.; Maclean, N.; Mahiddine, S. *Chem. Rev.* **2014**, *114* (15), 7610.

(23) Kwon, S. G.; Hyeon, T. *Small* **2011**, *7* (19), 2685.

(24) Ostwald, W. *Zeitschrift fuer Phys. Chemie, Stoechiom. und Verwandtschaftslehre* **1897**, *22*, 289.

(25) Sugimoto, T. *Adv. Colloid Interface Sci.* **1987**, *28*, 65.

(26) Peng, X.; Wickham, J.; Alivisatos, A. P. *J. Am. Chem. Soc.* **1998**, *120* (21), 5343.

(27) LaMer, V. K.; Dinegar, R. H. *J. Am. Chem. Soc.* **1950**, *72* (11), 4847.

(28) Mer, V. K. La. *Ind. Eng. Chem.* **1952**, *44* (6), 1270.

(29) Park, J.; Joo, J.; Soon, G. K.; Jang, Y.; Hyeon, T. *Angew. Chemie - Int. Ed.* **2007**,

46 (25), 4630.

(30) Li, J.; Wu, Q.; Wu, J. In *Handbook of Nanoparticles*; Springer International Publishing: Cham, 2015; pp 1–28.

(31) Moser, J.; Grätzel, M. *J. Am. Chem. Soc.* **1983**, *105* (22), 6547.

(32) Fox, M. A.; Lindig, B.; Chen, C. C. *J. Am. Chem. Soc.* **1982**, *104* (21), 5828.

(33) Duonghong, D.; Ramsden, J.; Grätzel, M. *J. Am. Chem. Soc.* **1982**, *104* (11), 2977.

(34) Kalyanasundaram, K.; Borgarello, E.; Duonghong, D.; Grätzel, M. *Angew. Chemie Int. Ed. English* **1981**, *20* (11), 987.

(35) Rossetti, R.; Brus, L. *J. Phys. Chem.* **1982**, *86* (23), 4470.

(36) Henglein, A. *Ber. Bunsenges. Phys. Chem* **1982**, *86*, 301.

(37) Weller, H.; Koch, U.; Gutiérrez, M.; Henglein, A. *Berichte der Bunsengesellschaft für Phys. Chemie* **1984**, *88* (7), 649.

(38) Brus, L. *J. Phys. Chem.* **1986**, *90* (12), 2555.

(39) Fojtik, A.; Weller, H.; Koch, U.; Henglein, A. *Berichte der Bunsengesellschaft/Physical Chem. Chem. Phys.* **1984**, *88* (10), 969.

(40) Rossetti, R.; Ellison, J. L.; Gibson, J. M.; Brus, L. E. *J. Chem. Phys.* **1984**, *80* (9), 4464.

(41) Steigerwald, M. L.; Brus, L. E. *Annu. Rev. Mater. Sci.* **1989**, *19* (1), 471.

(42) Brennan, J. G.; Siegrist, T.; Carroll, P. J.; Stuczynski, S. M.; Brus, L. E.; Steigerwald, M. L. *J. Am. Chem. Soc.* **1989**, *111* (11), 4141.

(43) Stuczynski, S. M.; Brennan, J. G.; Steigerwald, M. L. *Inorg. Chem.* **1989**, *28* (25), 4431.

(44) Steigerwald, M. L.; Alivisatos, A. P.; Gibson, J. M.; Harris, T. D.; Kortan, R.;

Muller, A. J.; Thayer, A. M.; Duncan, T. M.; Douglass, D. C.; Brus, L. E. *J. Am. Chem. Soc.* **1988**, *110* (10), 3046.

(45) Bawendi, M. G.; Kortan, A. R.; Steigerwald, M. L.; Brus, L. E. *J. Chem. Phys.* **1989**, *91* (11), 7282.

(46) Murray, C. B.; Norris, D. J.; Bawendi, M. G. *J. Am. Chem. Soc.* **1993**, *115*, 8706.

(47) Park, J.; An, K.; Hwang, Y.; Park, J. E. G.; Noh, H. J.; Kim, J. Y.; Park, J. H.; Hwang, N. M.; Hyeon, T. *Nat. Mater.* **2004**, *3* (12), 891.

(48) Trindade, T.; O'Brien, P.; Pickett, N. L. *Chem. Mater.* **2001**, *13* (11), 3843.

(49) Yu, W. W.; Peng, X. *Angew. Chemie - Int. Ed.* **2002**, *41* (13), 2368.

(50) van Embden, J.; Chesman, A. S. R.; Jasieniak, J. J. *Chem. Mater.* **2015**, *27* (7), 2246.

(51) Soon, G. K.; Piao, Y.; Park, J.; Angappane, S.; Jo, Y.; Hwang, N. M.; Park, J. G.; Hyeon, T. *J. Am. Chem. Soc.* **2007**, *129* (41), 12571.

(52) Bryks, W.; Wette, M.; Velez, N.; Hsu, S.-W.; Tao, A. R. *J. Am. Chem. Soc.* **2014**, *136* (17), 6175.

(53) Kuzuya, T.; Yamamuro, S.; Hihara, T.; Sumiyama, K. *Chem. Lett.* **2004**, *33* (3), 352.

(54) Choi, S. H.; An, K.; Kim, E. G.; Yu, J. H.; Kim, J. H.; Hyeon, T. *Adv. Funct. Mater.* **2009**, *19* (10), 1645.

(55) Han, W.; Yi, L.; Zhao, N.; Tang, A.; Gao, M.; Tang, Z. **2008**, No. c, 13152.

(56) Xie, R.; Rutherford, M.; Peng, X.; Fayette, V. *J. Am. Chem. Soc.* **2009**, *131* (12), 5691.

(57) Macdonald, J. E.; Bar Sadan, M.; Houben, L.; Popov, I.; Banin, U. *Nat. Mater.*

2010, *9* (10), 810.

(58) Owen, J. S.; Park, J.; Trudeau, P.; Alivisatos, A. P. *J. Am. Chem. Soc.* **2008**, *130* (37), 12279.

(59) Owen, J. *Science (80-.).* **2015**, *347* (6222), 615.

(60) De Roo, J.; Van Driessche, I.; Martins, J. C.; Hens, Z. *Nat. Mater.* **2016**, *15* (5), 517.

(61) Anderson, N. C.; Hendricks, M. P.; Choi, J. J.; Owen, J. S. *J. Am. Chem. Soc.* **2013**, *135* (49), 18536.

(62) Turo, M. J.; Macdonald, J. E. *ACS Nano* **2014**, *8* (10), 10205.

(63) Kippeny, T.; Swafford, L. A.; Rosenthal, S. J. *J. Chem. Educ.* **2009**, *79* (9), 1094.

(64) Ekimov, A. I.; Kudryavtsev, I. A.; Efros, A. L.; Yazeva, T. V.; Hache, F.; Schanne-Klein, M. C.; Rodina, A. V.; Ricard, D.; Flytzanis, C. *J. Opt. Soc. Am. B* **1993**, *10* (1), 100.

(65) Bawendi, M. G.; Steigerwald, M. L.; Brus, L. E. *Annu. Rev. Phys. Chem.* **1990**, *41* (1), 477.

(66) Alivisatos, A. P. *Science (80-.).* **1996**, *271* (5251), 933.

(67) Gin, P.; Bruchez, M.; Alivisatos, A. P.; Moronne, M.; Weiss, S. *Science (80-.).* **1998**, *281* (5385), 2013.

(68) Mattoussi, H.; Matthew Mauro, J.; Goldman, E. R.; Anderson, G. P.; Sundar, V. C.; Mikulec, F. V.; Bawendi, M. G. *J. Am. Chem. Soc.* **2000**, *122* (49), 12142.

(69) Thal, L. B.; Tomlinson, I. D.; Quinlan, M. A.; Kovtun, O.; Blakely, R. D.; Rosenthal, S. J. *ACS Chem. Neurosci.* **2018**.

(70) Howarth, M.; Chinnapen, D. J. F.; Gerrow, K.; Dorrestein, P. C.; Grandy, M. R.;

Kelleher, N. L.; El-Husseini, A.; Ting, A. Y. *Nat. Methods* **2006**, *3* (4), 267.

(71) Howarth, M.; Liu, W.; Puthenveetil, S.; Zheng, Y.; Marshall, L. F.; Schmidt, M. M.; Wittrup, K. D.; Bawendi, M. G.; Ting, A. Y. *Nat. Methods* **2008**, *5* (5), 397.

(72) Clarke, S.; Pinaud, F.; Beutel, O.; You, C.; Piehler, J.; Dahan, M. *Nano Lett.* **2010**, *10* (6), 2147.

(73) You, C.; Wilmes, S.; Beutel, O.; Lochte, S.; Podoplelowa, Y.; Roder, F.; Richter, C.; Seine, T.; Schaible, D.; Uzé, G.; Clarke, S.; Pinaud, F.; Dahan, M.; Piehler, J. *Angew. Chemie - Int. Ed.* **2010**, *49* (24), 4108.

(74) Farlow, J.; Seo, D.; Broaders, K. E.; Taylor, M. J.; Gartner, Z. J.; Jun, Y. W. *Nat. Methods* **2013**, *10* (12), 1203.

(75) You, C.; Wilmes, S.; Richter, C. P.; Beutel, O.; Liße, D.; Piehler, J. *ACS Chem. Biol.* **2013**, *8* (2), 320.

(76) Youn, H. C.; Baral, S.; Fendler, J. H. *J. Phys. Chem.* **1988**, *92* (22), 6320.

(77) Kortan, A. R.; Hull, R.; Opila, R. L.; Bawendi, M. G.; Steigerwald, M. L.; Carroll, P. J.; Brus, L. E. *J. Am. Chem. Soc.* **1990**, *112* (4), 1327.

(78) Dabbousi, B. O.; Rodriguez-Viejo, J.; Mikulec, F. V.; Heine, J. R.; Mattoussi, H.; Ober, R.; Jensen, K. F.; Bawendi, M. G. *J. Phys. Chem. B* **1997**, *101* (46), 9463.

(79) Carbone, L.; Nobile, C.; De Giorgi, M.; Della Sala, F.; Morello, G.; Pompa, P.; Hytch, M.; Snoeck, E.; Fiore, A.; Franchini, I. R.; Nadasan, M.; Silvestre, A. F.; Chiodo, L.; Kudera, S.; Cingolani, R.; Krahne, R.; Manna, L. *Nano Lett.* **2007**, *7* (10), 2942.

(80) Li, N.; Sun, Q.; Yu, Z.; Gao, X.; Pan, W.; Wan, X.; Tang, B. *ACS Nano* **2018**, *12* (6), 5197.

(81) Kamat, P. V. *J. Phys. Chem. C* **2008**, *112* (48), 18737.

(82) Robel, I.; Kuno, M.; Kamat, P. V. *J. Am. Chem. Soc.* **2007**, *129* (14), 4136.

(83) Hagfeldt, A.; Grätzel, M. *Chem. Rev.* **1995**, *95* (1), 49.

(84) Amirav, L.; Alivisatos, A. P. *J. Phys. Chem. Lett.* **2010**, *1* (7), 1051.

(85) Comin, A.; Manna, L. *Chem. Soc. Rev.* **2014**, *43* (11), 3957.

(86) Nan, W.; Niu, Y.; Qin, H.; Cui, F.; Yang, Y.; Lai, R.; Lin, W.; Peng, X. *J. Am. Chem. Soc.* **2012**, *134* (48), 19685.

(87) Alivisatos, A. P. *J. Phys. Chem.* **1996**, *100* (31), 13226.

(88) Evans, H. T. *Science (80-.).* **1979**, *203* (4378), 356.

(89) Evans, H. T. *Am. Mineral.* **1981**, *66* (7–8), 807.

(90) Du, H.; Chen, C.; Krishnan, R.; Krauss, T. D.; Harbold, J. M.; Wise, F. W.; Thomas, M. G.; Silcox, J. *Nano Lett.* **2002**, *2* (11), 1321.

(91) Miller, W. H. *A Treatise on Crystallography*; 1839.

(92) Goldstein, A. N.; Echer, C. M.; Alivisatos, A. P. *Science* **1992**, *256* (5062), 1425.

(93) Mews, A.; Kadavanich, A.; Banin, U.; Alivisatos, A. P. *Phys. Rev. B* **1996**, *53* (20), R13242.

(94) Peng, X.; Manna, L.; Yang, W.; Wickham, J. J.; Scher, E.; Kadavanich, A.; Alivisatos, A. P. *Nature* **2000**, *404* (March), 59.

(95) Manna, L.; Scher, E. C.; Alivisatos, A. P. *J. Am. Chem. Soc.* **2000**, *122* (51), 12700.

(96) Wang, F.; Tang, R.; Buhro, W. E. *Nano Lett.* **2008**, *8* (10), 3521.

(97) Manna, L.; Milliron, D. J.; Meisel, A.; Scher, E. C.; Alivisatos, A. P. *Nat. Mater.* **2003**, *2* (6), 382.

(98) Talapin, D. V.; Nelson, J. H.; Shevchenko, E. V.; Aloni, S.; Sadtler, B.; Alivisatos, A. P. *Nano Lett.* **2007**, *7* (10), 2951.

(99) Wu, K.; Hill, L. J.; Chen, J.; McBride, J. R.; Pavlopolous, N. G.; Richey, N. E.; Pyun, J.; Lian, T. *ACS Nano* **2015**, *9* (4), 4591.

(100) Washington, A. L.; Foley, M. E.; Cheong, S.; Quffa, L.; Breshike, C. J.; Watt, J.; Tilley, R. D.; Strouse, G. F. *J. Am. Chem. Soc.* **2012**, *134* (41), 17046.

(101) Gao, Y.; Peng, X. *J. Am. Chem. Soc.* **2014**, *136* (18), 6724.

(102) Mahler, B.; Lequeux, N.; Dubertret, B. *J. Am. Chem. Soc.* **2010**, *132* (3), 953.

(103) Huang, J.; Kovalenko, M. V.; Talapin, D. V. *J. Am. Chem. Soc.* **2010**, *132* (45), 15866.

(104) Bragg, W. H.; Bragg, W. L. *Proc. R. Soc. A Math. Phys. Eng. Sci.* **1913**, *88* (605), 428.

(105) Patterson, A. L. *Phys. Rev.* **1939**, *56* (10), 978.

(106) Gariano, G.; Lesnyak, V.; Brescia, R.; Bertoni, G.; Dang, Z.; Gaspari, R.; De Trizio, L.; Manna, L. *J. Am. Chem. Soc.* **2017**, *139* (28), 9583.

(107) Kamat, P. V. *J. Phys. Chem. C* **2007**, *111* (7), 2834.

(108) Wu, Y.; Wadia, C.; Ma, W.; Sadtler, B.; Alivisatos, A. P. *Nano Lett.* **2008**, *8* (8), 2551.

(109) Zhao, Y.; Burda, C. *Energy Environ. Sci.* **2012**, *5*, 5564.

(110) Leach, A. D. P.; Mast, L. G.; Hernández-Pagán, E. A.; Macdonald, J. E. *J. Mater. Chem. C* **2015**, *3* (14), 3258.

(111) Stam, W. Van Der; Gradmann, S.; Altantzis, T.; Ke, X.; Baldus, M.; Bals, S.; Donega, C. D. M. *Chem. Mater.* **2016**, *28*, 6705.

(112) Ma, G.; Zhou, Y.; Li, X.; Sun, K.; Liu, S.; Hu, J.; Kotov, N. A. *ACS Nano* **2013**, *7* (10), 9010.

(113) Sadtler, B.; Demchenko, D. O.; Zheng, H.; Hughes, S. M.; Merkle, M. G.; Dahmen, U.; Wang, L.; Alivisatos, A. P. *J. Am. Chem. Soc.* **2009**, *131* (18), 5285.

(114) Kruszynska, M.; Borchert, H.; Bachmatiuk, A.; Rümmeli, M. H.; Büchner, B.; Parisi, J.; Kolny-Olesiak, J. *ACS Nano* **2012**, *6* (7), 5889.

(115) Cho, K. S.; Talapin, D. V.; Gaschler, W.; Murray, C. B. *J. Am. Chem. Soc.* **2005**, *127* (19), 7140.

(116) Koh, W. K.; Bartnik, A. C.; Wise, F. W.; Murray, C. B. *J. Am. Chem. Soc.* **2010**, *132* (11), 3909.

(117) Penn, R. L.; Banfield, J. F. *Geochim. Cosmochim. Acta* **1999**, *63* (10), 1549.

(118) Tang, Z.; Kotov, N. A.; Giersig, M. *Science* **2002**, *297* (5579), 237.

(119) Pacholski, C.; Kornowski, A.; Weller, H. *Angew. Chemie-International Ed.* **2002**, *41* (7), 1188.

(120) O'Sullivan, C.; Gunning, R. D.; Sanyal, A.; Barrett, C. A.; Geaney, H.; Laffir, F. R.; Ahmed, S.; Ryan, K. M. *J. Am. Chem. Soc.* **2009**, *131* (16), 12250.

(121) Evans, H. T. *Zeitschrift für Krist.* **1979**, *150* (1–4), 299.

(122) Vinokurov, K.; Macdonald, J. E.; Banin, U. *Chem. Mater.* **2012**, *24*, 1822.

(123) Lai, Y.-H.; Yeh, C.-T.; Cheng, S.-H.; Liao, P.; Hung, W.-H. *J. Phys. Chem. B* **2002**, *106* (21), 5438.

(124) Wang, X.; Altmann, L.; Zielasek, V.; Al-Shamery, K.; Borchert, H.; Kolny-Olesiak, J. *Chem. Mater.* **2012**, *25*, 1400.

(125) Hens, Z.; Martins, J. C. *Chem. Mater.* **2013**, *25* (8), 1211.

(126) Will, G.; Hinze, E.; Abdelrahman, A. R. M. *Eur. J. Mineral.* **2002**, *14* (3), 591.

(127) Momma, K.; Izumi, F. *J. Appl. Crystallogr.* **2011**, *44* (6), 1272.

(128) Zhang, H.-T.; Wu, G.; Chen, X.-H. *Langmuir* **2005**, *21* (10), 4281.

(129) Saunders, A. E.; Ghezelbash, A.; Smilgies, D.-M.; Sigman, M. B.; Korgel, B. A. *Nano Lett.* **2006**, *6* (12), 2959.

(130) Tolbert, S. H.; Alivisatos, A. P. *Science (80-.).* **1994**, *265* (5170), 373.

(131) Hussain, R. A.; Badshah, A.; Lal, B. *J. Solid State Chem.* **2016**, *243*, 179.

(132) Fenton, J. L.; Schaak, R. E. *Angew. Chemie - Int. Ed.* **2017**, *56* (23), 6464.

(133) Nam, K. M.; Kim, Y.-I.; Jo, Y.; Lee, S. M.; Kim, B. G.; Choi, R.; Choi, S.-I.; Song, H.; Park, J. T. *J. Am. Chem. Soc.* **2012**, *134* (20), 8392.

(134) Norako, M. E.; Greaney, M. J.; Brutchey, R. L. *J. Am. Chem. Soc.* **2012**, *134* (1), 23.

(135) Powell, A. E.; Hodges, J. M.; Schaak, R. E. *J. Am. Chem. Soc.* **2016**, *138* (2), 471.

(136) Seo, W. S.; Shim, J. H.; Oh, S. J.; Lee, E. K.; Hur, N. H.; Park, J. T. *J. Am. Chem. Soc.* **2005**, *127* (17), 6188.

(137) Singh, S.; Ryan, K. M. *J. Phys. Chem. Lett.* **2015**, *6* (16), 3141.

(138) Gao, Y.; Peng, X. *J. Am. Chem. Soc.* **2014**, *136* (18), 6724.

(139) Rhodes, J. M.; Jones, C. A.; Thal, L. B.; MacDonald, J. E. *Chem. Mater.* **2017**, *29* (19), 8521.

(140) Scotognella, F.; Della Valle, G.; Srimath Kandada, A. R.; Dorfs, D.; Zavelani-Rossi, M.; Conforti, M.; Miszta, K.; Comin, A.; Korobchevskaya, K.; Lanzani, G.; Manna, L.; Tassone, F. *Nano Lett.* **2011**, *11* (11), 4711.

(141) Riha, S. C.; Johnson, D. C.; Prieto, A. L. *J. Am. Chem. Soc.* **2011**, *133* (5), 1383.

(142) Liu, X.; Wang, X.; Zhou, B.; Law, W. C.; Cartwright, A. N.; Swihart, M. T. *Adv. Funct. Mater.* **2013**, *23* (10), 1256.

(143) Kriegel, I.; Jiang, C.; Rodríguez-Fernández, J.; Schaller, R. D.; Talapin, D. V.; Da Como, E.; Feldmann, J. *J. Am. Chem. Soc.* **2012**, *134* (3), 1583.

(144) Hessel, C. M.; P. Pattani, V.; Rasch, M.; Panthani, M. G.; Koo, B.; Tunnell, J. W.; Korgel, B. A. *Nano Lett.* **2011**, *11* (6), 2560.

(145) Wang, W.; Zhang, L.; Chen, G.; Jiang, J.; Ding, T.; Zuo, J.; Yang, Q. *CrystEngComm* **2015**, *17* (9), 1975.

(146) Eikeland, E.; Blichfeld, A. B.; Borup, K. A.; Zhao, K.; Overgaard, J.; Shi, X.; Chen, L.; Iversen, B. B. *IUCrJ* **2017**, *4*, 476.

(147) Liu, S.; Zhang, Z.; Bao, J.; Lan, Y.; Tu, W.; Han, M.; Dai, Z. *J. Phys. Chem. C* **2013**, *117* (29), 15164.

(148) Coughlan, C.; Ibáñez, M.; Dobrozhan, O.; Singh, A.; Cabot, A.; Ryan, K. M. *Chem. Rev.* **2017**, *117* (9), 5865.

(149) Beberwyck, B. J.; Surendranath, Y.; Alivisatos, A. P. *J. Phys. Chem. C* **2013**, *117* (39), 19759.

(150) De Trizio, L.; Manna, L. *Chem. Rev.* **2016**, *116* (18), 10852.

(151) Low, K. H.; Li, C. H.; Roy, V. A. L.; Chui, S. S. Y.; Chan, S. L. F.; Che, C. M. *Chem. Sci.* **2010**, *1* (4), 515.

(152) Brutchey, R. L. *Acc. Chem. Res.* **2015**, *48* (11), 2918.

(153) Tappan, B. A.; Barim, G.; Kwok, J. C.; Brutchey, R. L. *Chem. Mater.* **2018**, *30* (16), 5704.

(154) Berends, A. C.; van der Stam, W.; Akkerman, Q. A.; Meeldijk, J. D.; van der Lit,

J.; de Mello Donega, C. *Chem. Mater.* **2018**, *30* (11), 3836.

(155) Bryks, W.; Smith, S. C.; Tao, A. R. *Chem. Mater.* **2017**, *29* (8), 3653.

(156) Guo, Y.; Alvarado, S. R.; Barclay, J. D.; Vela, J. *ACS Nano* **2013**, *7* (4), 3616.

(157) Glazov, V. M.; Pashinkin, A. S.; Fedorov, V. A. *Inorg. Mater.* **2000**, *36* (7), 641.

(158) Marbella, L. E.; Gan, X. Y.; Kaseman, D. C.; Millstone, J. E. *Nano Lett.* **2017**, *17* (4), 2414.

(159) Dorfs, D.; Härtling, T.; Miszta, K.; Bigall, N. C.; Kim, M. R.; Genovese, A.; Falqui, A.; Povia, M.; Manna, L. *J. Am. Chem. Soc.* **2011**, *133* (29), 11175.

(160) Rivest, J. B.; Fong, L.-K.; Jain, P. K.; Toney, M. F.; Alivisatos, A. P. *J. Phys. Chem. Lett.* **2011**, *2*, 2402.

(161) Koparde, V. N.; Cummings, P. T. *ACS Nano* **2008**, *2* (8), 1620.

(162) Bryks, W.; Lupi, E.; Ngo, C.; Tao, A. R. *J. Am. Chem. Soc.* **2016**, *138* (41), 13717.

(163) Chen, Y. B.; Chen, L.; Wu, L. M. *Inorg. Chem.* **2005**, *44* (26), 9817.

(164) Dance, I. G.; Fisher, K. J.; Banda, R. M. H.; Scudder, M. L. *Inorg. Chem.* **1991**, *30* (2), 183.

(165) Hollingsworth, N.; Roffey, A.; Islam, H. U.; Mercy, M.; Roldan, A.; Bras, W.; Wolthers, M.; Catlow, C. R. A.; Sankar, G.; Hogarth, G.; De Leeuw, N. H. *Chem. Mater.* **2014**, *26* (21), 6281.

(166) Turo, M. J.; Shen, X.; Brandon, N. K.; Castillo, S.; Fall, A. M.; Pantelides, S. T.; Macdonald, J. E. *Chem. Commun.* **2016**, *52* (82), 12214.

(167) Dilimon, V. S.; Fonder, G.; Delhalle, J.; Mekhalif, Z. *J. Phys. Chem. C* **2011**, *115* (37), 18202.

(168) Li, H.; Brescia, R.; Povia, M.; Prato, M.; Bertoni, G.; Manna, L.; Moreels, I. *J.*

Am. Chem. Soc. **2013**, *135* (33), 12270.

(169) Tu, R.; Xie, Y.; Bertoni, G.; Lak, A.; Gaspari, R.; Rapallo, A.; Cavalli, A.; Trizio, L. De; Manna, L. *J. Am. Chem. Soc.* **2016**, *138* (22), 7082.

(170) Li, W.; Zamani, R.; Rivera Gil, P.; Pelaz, B.; Ibáñez, M.; Cadavid, D.; Shavel, A.; Alvarez-Puebla, R. A.; Parak, W. J.; Arbiol, J.; Cabot, A. *J. Am. Chem. Soc.* **2013**, *135* (19), 7098.

(171) Yang, H. J.; Chen, C. Y.; Yuan, F. W.; Tuan, H. Y. *J. Phys. Chem. C* **2013**, *117* (42), 21955.

(172) Willhammar, T.; Sentosun, K.; Mourdikoudis, S.; Goris, B.; Kurttepeli, M.; Bercx, M.; Lamoen, D.; Partoens, B.; Pastoriza-Santos, I.; Pe´rez-Juste, J.; Liz-Marzán, L. M.; Bals, S.; Van Tendeloo, G. *Nat. Commun.* **2017**, *8*, 1.

(173) Poulose, A. C.; Veeranarayanan, S.; Mohamed, M. S.; Aburto, R. R.; Mitcham, T.; Bouchard, R. R.; Ajayan, P. M.; Sakamoto, Y.; Maekawa, T.; Kumar, D. S. *Sci. Rep.* **2016**, *6*, 1.

(174) Wang, X.; Ma, Y.; Chen, H.; Wu, X.; Qian, H.; Yang, X.; Zha, Z. *Colloids Surfaces B Biointerfaces* **2017**, *152*, 449.

(175) Nethravathi, C.; Rajamathi, C. R.; Rajamathi, M.; Maki, R.; Mori, T.; Golberg, D.; Bando, Y. *J. Mater. Chem. A* **2014**, *2* (4), 985.

(176) Zhou, C.; Dun, C.; Wang, Q.; Wang, K.; Shi, Z.; Carroll, D. L.; Liu, G.; Qiao, G. *ACS Appl. Mater. Interfaces* **2015**, *7* (38), 21015.

(177) Ghosh, A.; Mitra, M.; Banerjee, D.; Mondal, A. *RSC Adv.* **2016**, *6* (27), 22803.

(178) Wang, H.; Zuo, P.; Wang, A.; Zhang, S.; Mao, C.; Song, J.; Niu, H.; Jin, B.; Tian, Y. *J. Alloys Compd.* **2013**, *581*, 816.

(179) PashinkinV., A. S.; Fedorov, A. *Inorg. Mater.* **2003**, *39* (6), 539.

(180) Da Silva, J. L. F.; Wei, S. H.; Zhou, J.; Wu, X. *Appl. Phys. Lett.* **2007**, *91* (9), 2.

(181) Palchik, O.; Kerner, R.; Zhu, Z.; Gedanken, A. *J. Solid State Chem.* **2000**, *154* (2), 530.

(182) Zhang, Y.; Qiao, Z. P.; Chen, X. M. *J. Mater. Chem.* **2002**, *12* (9), 2747.

(183) Zhang, L.; Ai, Z.; Jia, F.; Liu, L.; Hu, X.; Yu, J. C. *Chem. - A Eur. J.* **2006**, *12* (15), 4185.

(184) Kumar, P.; Singh, K. *Cryst. Growth Des.* **2009**, *9* (7), 3089.

(185) Mugnaioli, E.; Gemmi, M.; Tu, R.; David, J.; Bertoni, G.; Gaspari, R.; De Trizio, L.; Manna, L. *Inorg. Chem.* **2018**, *57* (16), 10241.

(186) Hernández-Pagán, E. A.; Robinson, E. H.; La Croix, A. D.; Macdonald, J. E. *Chem. Mater.* **2019**, *31* (12), 4619.

(187) Li, Y.; Silverton, L. C.; Haasch, R.; Tong, Y. Y. *Langmuir* **2008**, *24* (14), 7048.

(188) Uemura, S.; Fukuzawa, S. I.; Patil, S. R. *J. Organomet. Chem.* **1983**, *243* (1), 9.

(189) Stuhr-Hansen, N.; Nørgaard, K.; Christensen, J. B.; Nielsen, L. K.; Bjørnholm, T.; Brust, M. *Nano Lett.* **2001**, *1* (4), 189.

(190) Peng, J.; Pan, Y.; Yu, Z.; Wu, J.; Wu, J.; Zhou, Y.; Guo, Y.; Wu, X.; Wu, C.; Xie, Y. *Angew. Chemie - Int. Ed.* **2018**, *57* (41), 13533.

(191) Lin, Y.; Wu, Y.; Wang, R.; Tao, G.; Luo, P. F.; Lin, X.; Huang, G.; Li, J.; Yang, H. H. *Chem. Commun.* **2018**, *54* (62), 8579.

(192) Chen, Y. S.; Ding, J.; He, X. M.; Xu, J.; Feng, Y. Q. *Microchim. Acta* **2018**, *185* (8).

(193) Xu, C.; Kong, A.; Ding, H.; Shan, Y. *Mater. Lett.* **2012**, *82*, 45.

(194) Wu, M.; Wang, Y.; Wang, H.; Wang, H.; Sui, Y.; Du, F.; Yang, X.; Zou, B. *Nanoscale* **2018**, *10* (46), 21928.

(195) She, G.; Zhang, X.; Shi, W.; Cai, Y.; Wang, N.; Liu, P.; Chen, D. *Cryst. Growth Des.* **2008**, *8* (6), 1789.

(196) Park, J. S.; Yang, J. H.; Kanevce, A.; Choi, S.; Repins, I. L.; Wei, S. H. *Phys. Rev. B - Condens. Matter Mater. Phys.* **2015**, *91* (7), 1.

(197) Cozzoli, P. D.; Manna, L.; Curri, M. L.; Kudera, S.; Giannini, C.; Striccoli, M.; Agostiano, A. *Chem. Mater.* **2005**, *17* (6), 1296.

(198) Dawood, F.; Schaak, R. E. *J. Am. Chem. Soc.* **2009**, *131* (34), 12494.

(199) Li, L. S.; Pradhan, N.; Wang, Y.; Peng, X. *Nano Lett.* **2004**, *4* (11), 2261.

(200) Hines, M. A.; Scholes, G. D. *Adv. Mater.* **2003**, *15* (21), 1844.

(201) Zheng, X.; Han, X.; Liu, H.; Chen, J.; Fu, D.; Wang, J.; Zhong, C.; Deng, Y.; Hu, W. *ACS Appl. Mater. Interfaces* **2018**, *10* (16), 13675.

(202) McBride, J. R.; Pennycook, T. J.; Pennycook, S. J.; Rosenthal, S. J. *ACS Nano* **2013**, *7* (10), 8358.

(203) Subbarao, U.; Marakatti, V. S.; Amshumali, M. K.; Loukya, B.; Singh, D. K.; Datta, R.; Peter, S. C. *J. Solid State Chem.* **2016**, *244* (August), 84.

(204) Sobhani, A.; Salavati-Niasari, M. *Superlattices Microstruct.* **2014**, *65*, 79.

(205) Bestgen, S.; Fuhr, O.; Roesky, P. W.; Fenske, D. *Dalt. Trans.* **2016**, *45*, 14907.

(206) Schoen, D. T.; Xie, C.; Cui, Y. *J. Am. Chem. Soc.* **2007**, *129* (14), 4116.

(207) Sahu, A.; Qi, L.; Kang, M. S.; Deng, D.; Norris, D. J. *J. Am. Chem. Soc.* **2011**, *133* (17), 6509.

(208) Bailey, D. M.; Catron, M. A.; Kovtun, O.; Macdonald, R. L.; Zhang, Q.;

Rosenthal, S. J. *ACS Chem. Neurosci.* **2018**, *9*, 2534.

(209) Gary, D. C.; Flowers, S. E.; Kaminsky, W.; Petrone, A.; Li, X.; Cossairt, B. M. *J. Am. Chem. Soc.* **2016**, *138* (5), 1510.

(210) Gary, D. C.; Petrone, A.; Li, X.; Cossairt, B. M. *Chem. Commun.* **2017**, *20*, 2.

(211) Xia, C.; Meeldijk, J. D.; Gerritsen, H. C.; De Mello Donega, C. *Chem. Mater.* **2017**, *29* (11), 4940.

(212) Nguyen, L. M.; Dellinger, M. E.; Lee, J. T.; Quinlan, R. A.; Rheingold, A. L.; Pike, R. D. *Inorganica Chim. Acta* **2005**, *358* (4), 1331.

(213) Olshansky, J. H.; Ding, T. X.; Lee, Y. V.; Leone, S. R.; Alivisatos, A. P. *J. Am. Chem. Soc.* **2015**, *137* (49), 15567.

(214) Ding, T. X.; Olshansky, J. H.; Leone, S. R.; Alivisatos, A. P. *J. Am. Chem. Soc.* **2015**, *137*, 2021.

(215) Creaser, I. I.; Sargeson, A. M.; Zanella, A. W. *Inorg. Chem.* **1983**, *22* (26), 4022.

(216) He, F. M. C.; Bernhardt, P. V. *J Biol Inorg Chem* **2017**, *22*, 775.

(217) Chou, M.; Creutz, C.; Sutin, N. *J. Am. Chem. Soc.* **1977**, *99* (17), 5615.

(218) Gahan, L. R.; Harrowfield, J. M. *Polyhedron* **2015**, *94*, 1.

(219) Gahan, L. R.; Healy, P. C.; Patch, G. J. *J. Chem. Educ.* **1989**, *66* (5), 445.

(220) Creaser, I. I.; Geue, R. J.; Harrowfield, J. M.; Herlt, A. J.; Sargeson, A. M.; Snow, M. R.; Springborg, J. *J. Am. Chem. Soc.* **1982**, *104* (22), 6016.

(221) Eberson, L.; Ekström, M.; Mattinen, J.; Bernáth, G.; Eberson, L. *Acta Chem. Scand.* **1987**, *41b*, 41.

(222) Chen, O.; Zhao, J.; Chauhan, V. P.; Cui, J.; Wong, C.; Harris, D. K.; Wei, H.; Han, H. S.; Fukumura, D.; Jain, R. K.; Bawendi, M. G. *Nat. Mater.* **2013**, *12* (5), 445.

(223) Sugimoto, H.; Hataoka, H.; Mori, M. *J. Chem. Soc. Chem. Commun.* **1982**, No. 22, 1301.

(224) Barry, L. G. *Am. Mineral.* **1954**, *39*, 504.

(225) Howard T. Evans, J.; Konnert, J. A. *Am. Mineral.* **1976**, *61*, 996.

(226) Akkerman, Q. A.; Genovese, A.; George, C.; Prato, M.; Moreels, I.; Casu, A.; Marras, S.; Curcio, A.; Scarpellini, A.; Pellegrino, T.; Manna, L.; Lesnyak, V. *ACS Nano* **2015**, *9* (1), 521.

(227) Van Der Stam, W.; Berends, A. C.; Rabouw, F. T.; Willhammar, T.; Ke, X.; Meeldijk, J. D.; Bals, S.; De Mello Donega, C. *Chem. Mater.* **2015**, *27* (2), 621.

Evan Hojer Robinson

6900 Lenox Village Dr. Apt. #471 • Nashville, TN 37211
850-982-0936 • evanhrob@gmail.com

Summary

- Recently defended PhD dissertation in materials chemistry at Vanderbilt University
- Previous experience as a process development engineering co-op in the semiconductor industry
- More than 1.5 years of work experience as a research chemist developing and characterizing ceramic membranes in an industrial environment
- Has real work experience reaching large, long-term goals and managing multiple projects simultaneously
- Very conscious of laboratory safety and the well-being of coworkers

Education

Doctor of Philosophy, Chemistry — **Feb. 2020 (defended)**
Vanderbilt University, Nashville, TN

Master of Science, Semiconductor/Photovoltaic Device Processing — **Sept. 2013**
University of Oregon, Eugene, OR

Bachelor of Science, Chemistry, minor in Anthropology — **Dec. 2009**
University of Florida, Gainesville, FL

Professional Experience

Vanderbilt University, Chemistry Dept., Nashville, TN — **July 2014 – present**
Research Assistant — **Aug. 2014 – present**

- Learned and applied the fundamentals of colloidal nanocrystal synthesis and characterization resulting in new synthetic method for Cu_2S nanorods
- Developed a new direct synthesis for wurtzite $Cu_{2-x}Se$ nanocrystals with collaborators
- Maintained Rigaku SmartLab powder x-ray diffractometer as designated student tech
- Mentored REU student and multiple rotation students
- Worked with lab mates to improve lab safety as the safety officer

Teaching Assistant

General Chemistry Laboratory — **Aug. 2014 – May 2015**
Advanced Integrated Laboratory — **Jan. 2020 – present**

Fairchild Semiconductor International, Inc., Portland, ME — **Jan. 2013 – Sept. 2013**
Process Development Engineer Co-op

- Processed wafers through oxide deposition and planarization operations, targeted thicknesses, created and tuned ellipsometer recipes for characterization
- Planned and monitored fabrication operations on multiple development DoE (experimental design) wafer lots
- Taught myself how to program, learned the JMP Scripting Language and wrote code for Process Engineering, Quality Assurance, Wafer-Level Reliability, Process Technology Development, and Device Engineering
- Trained engineers and developed training documentation on JMP use and script execution

Media and Process Technology, Inc., Pittsburgh, PA — **March 2010 – Nov. 2011**
Application Chemist

- Designed and fabricated Swagelok-based pressurized fluid systems for ceramic membrane R&D
- Performed over 2000 gas chromatography runs with a multiple-GC system to characterize own membranes after processing them
- Gained some field experience through traveling out of state to disassemble a biogas unit
- Formulated a solution to regenerate contaminated membranes for used motor oil recycling project

Publications and Presentations

1. **Robinson, E. H.**; Turo, M. J.; Macdonald, J. E. Controlled Surface Chemistry for the Directed Attachment of Copper(I) Sulfide Nanocrystals. *Chem. Mater.* **2017**, *29*, 3854–3857.
   - Research poster presented at the 2015 Southeast Regional Meeting of the American Chemical Society (SERMACS), Memphis, TN
   - Research poster presented at the 2017 National Meeting of the American Chemical Society, Washington, DC
2. Hernández-Pagán, E. A.;* **Robinson, E. H.**;* La Croix, A. D.; Macdonald, J. E. Direct Synthesis of Novel $Cu_{2-x}Se$ Wurtzite Phase. *Chem. Mater.* **2019**, 31, 4619-4624. *authors share first-author credit
3. **Robinson, E. H.**; Dwyer, K. M.; Nuriye, A. Y.; Macdonald, J. E. Investigation into $Cu_{2-x}Te$ Nanocrystal Syntheses Using a Ditelluride Precursor. *In Preparation.*

Skills and Instrumentation

- Academic hands-on **semiconductor** device processing experience
  - Photolithography, LPCVD, diffusion, wet/plasma etch, spin coating
- Industrial **semiconductor** device processing exposure
  - CVD, CMP
- Ceramic **membrane** R&D
  - Layer deposition (dip and spray), liquid and gas separation
- Powder **XRD** Student Tech – Rigaku SmartLab **April 2017 – Dec. 2019**
  - Responsible for instrument maintenance, user training and billing

- TEM – analyzed approximately 500 samples, HR-TEM, SAED, received EDS map training
- Nanocrystal synthesis - Cu_2S, $Cu_{2-x}Se$, $Cu_{2-x}Te$, ZnSe, CdSe, CdSe/CdS core/shell, PbSe, Ag_2Se, NiSe
- UV-Vis, fluorimetry, TGA, GC, IR, XPS (basic), NMR (basic), ICP (basic), glovebox
- TopSpin (NMR), CasaXPS (XPS), Adobe Illustrator and Photoshop (basic), Microsoft Office
- **JMP** and use of the JMP Scripting Language

Community Outreach and Leadership

Vanderbilt Student Volunteers for Science **Aug. 2015 – Dec. 2018**

- Team Leader **Jan. 2016 – Dec. 2017**
- Vanderbilt Children's Hospital Group **Jan. 2018 – Dec. 2018**

Vanderbilt Institute for Nanoscale Science and Engineering (VINSE)
Student Selected Seminar Committee **July 2017 – May 2018**

Mitchum E. Warren Committee **Aug. 2018 – Aug. 2019**

Awards and Honors

Mitchum E. Warren Fellowship **Aug. 2018 – Dec. 2018**
1st Place Award – VINSE NanoDay Poster Competition **Oct. 2015**
Florida Bright Futures Scholarship (Full undergraduate tuition coverage)